PONTIFICIA UNIVERSIDAD CATOLICA DE CHILE

ESCUELA DE INGENIERIA

FAULT-CONTROLLED DEVELOPMENT OF SHALLOW HYDROTHERMAL SYSTEMS, SOUTHERN ANDES

TOMÁS E. ROQUER

Thesis submitted to the Office of Research and Graduate Studies in partial fulfillment of the requirements for the Degree of Master of Science in Engineering

Advisor:

GLORIA ARANCIBIA H.

Santiago de Chile, January, 2016

PONTIFICIA UNIVERSIDAD CATOLICA DE CHILE
ESCUELA DE INGENIERIA

FAULT-CONTROLLED DEVELOPMENT OF SHALLOW HYDROTHERMAL SYSTEMS, SOUTHERN ANDES

TOMÁS ESTEBAN ROQUER RODRÍGUEZ

Members of the Committee:

GLORIA ARANCIBIA H.

GONZALO YÁÑEZ C.

DIEGO MORATA C.

CARLOS BONILLA M.

Thesis submitted to the Office of Research and Graduate Studies in partial fulfillment of the requirements for the Degree of Master of Science in Engineering

Santiago de Chile, January, 2016

A mi abuelo, padres, hermanos y amigos, que me han apoyado incasablemente

ACKNOWLEDGEMENTS

I thank the members of my Committee Carlos Bonilla, Diego Morata and Gonzalo Yáñez. I specially thank my advisor Gloria Arancibia, who showed me what would become my vocation. She restlessly guided this thesis with genuine scientific and humane interest. I thank Martin Reich (UChile), who supported this work; and José Cembrano (PUC), whose active guidance helped me develop some of the ideas presented here. I specially thank the help and support of Julie Rowland (University of Auckland), who kindly received and guided me during my research visit to New Zealand.

This thesis is a contribution to the FONDECYT Project #1130030 "The feedback between active tectonics, fluid flow and mineralization in an Andean geothermal reservoir: a case of study from the Tolhuaca System, Southern Chile", directed by Martin Reich, and to the FONDAP-CONICYT Project #15090013 "Centro de Excelencia en Geotermia de los Andes". An international research visit was funded by the CONICYT-REDES Project #140036. Field measurements were made with devices provided by the FONDEF Project #D10I1027. Partial funding for college fees came from the "San Andrés" scholarship, provided by College UC. I acknowledge financial support given by the Dirección de Postgrado de la Escuela de Ingeniería UC (DIPEI) funds to assist to international conferences.

This work would have been impossible without the help of my unforgettable field companions: Juancho and Pablo Sánchez (UChile) and Pamela Pérez (PUC), thank you very much! XRD methods were learnt under the tutelage of Mercedes Vázquez (UChile), and samples were prepared with the help of Fabián Tapia (UChile) and Estefanía Terrón (Universidad Politécnica de Madrid). I particularly thank the help of Patrick Brown (University of Auckland), who generously contributed with the petrographic analysis. Pablo Iturrieta (PUC) collaborated with failure envelope models. Nicolás and Ronny (PUC) contributed with the inversion and interpretation of electrical data.

Thanks to Mariel, who has always been a helpful hand. There are not enough words to thank my geo-friends, who always supported and accompanied me. Tiaren, Rodrigo, Gerd, Gert and Ashley: THANKS A LOT!

And last but no least: I thank my mother, who taught me to never give up; my father, who always motivated my scientific curiosity; my siblings, who gave me the love and support so necessary in times of crisis; my grandfather, who taught me how to cultivate a desire of personal improvement; and Gabriel, who has accompanied me in this long process.

TABLE OF CONTENTS

Page

LIST OF TABLES

Page

LIST OF FIGURES

Page

RESUMEN

Las zonas de falla controlan la formación de sistemas hidrotermales someros, candidatos para el desarrollo de sistemas geotérmicos. El modo de falla es controlado por la presión de fluido ($P_F = \lambda_V * \sigma_V$, λ_V = factor de presión de poro, σ_V = estrés vertical) y el estrés diferencial ($\sigma_1 - \sigma_3$), generando distintos estilos de deformación (extensional y/o cizalle). La Zona Volcánica Sur de los Andes (ZVS) es una de las regiones geotermales más vastas e inexploradas del mundo, ideal para estudiar la interacción entre el modo de deformación y el transporte de fluidos. El Sistema de Falla Liquiñe-Ofqui (SFLO) y el Sistema de Falla de Larga Vida Oblicuo al Arco (SFOA) corresponden a fallas corticales que controlan la tectónica de la ZVS. En este trabajo, dos transectas de meso-escala, que representan a cada sistema, fueron estudiadas mediante mapeo estructural, sondajes eléctricos 2D *in situ*, petrografía, difracción de rayos X y microscopía electrónica de barrido. El análisis meso- y microestructural sugiere que la exposición del SFLO está dominada por una falla EW cíclica en extensión (±cizalle) en un régimen de rumbo Andersoniano. En cambio, el afloramiento del SFOA registra dos modos de falla de rumbo NW sobreimpuestos: (1) cizalle (±extensión) en un régimen de rumbo Andersoniano; y (2) extensión (±cizalle) en un régimen transtensional no-Andersoniano. Zeolitas ricas en Ca y Ca(-Na), que ocurren principalmente en venas del bloque colgante, indican temperaturas de cristalización entre 110-210°C y paleo-profundidades entre 2.1-3.5 km (asumiendo 60-100°C/km). Los resultados de sondajes eléctricos sugieren una correlación significativa entre la cantidad de zeolitas (por unidad de área) y la conductividad de la roca, mayor en el núcleo y el bloque colgante, comparada a una roca de caja andesítica inalterada. Para campos de estrés dados en la ZVS se construyeron, mediante modelación numérica, diagramas de modo de falla en el espacio λ-σ. En la exposición del SFLO, la falla en extensión (±cizalle) probablemente ocurre entre rangos típicos de factor de presión de poro ($0.4 \leq \lambda_V \leq 0.48$). Por el contrario, en el afloramiento del SFOA, el cambio entre falla en cizalle (±extensión) y extensión (±cizalle) necesariamente involucra una sobrepresión de fluidos (λ_V >50-88% sobre la presión hidrostática). Estos resultados sugieren que las condiciones de estrés de largo plazo favorecen: (1) el almacenamiento de fluidos sobrepresurizados en sistemas hidrotermales espacialmente asociados a las fallas NW del SFOA; y (2) flujo localizado y continuo en conductos verticales asociados a las fallas EW del SFLO. La ocurrencia de sistemas geotermales en la ZVS requiere de zonas de falla regionales que acumulen y transporten fluidos hidrotermales, lo que podría estar dado por las interacciones entre las fallas NW del SFOA y EW del SFLO.

Palabras clave: Sistema de Falla Liquiñe-Ofqui, Sistema de Falla de Larga Vida Oblicuo al Arco, modo de falla, resistividad eléctrica, exploración geotermal, zeolitas, sobrepresión de fluido

ABSTRACT

Fault zones exert a first order control on formation of shallow hydrothermal systems, candidates for development of geothermal systems. The failure mode within fault zones is controlled by the pore fluid pressure ($P_F = \lambda_V * \sigma_V$, λ_V = pore fluid factor, σ_V = vertical stress) and differential stress ($\sigma_1 - \sigma_3$), generating different styles of deformation (extensional and/or shear failure). The Southern Volcanic Zone of the Andes (SVZ) is one of the largest, unprospected geothermal regions in the world, ideal to study the interaction between mode of deformation and fluid transport. The Liquiñe-Ofqui Fault System (LOFS) and the Arc-oblique Long-lived Fault System (ALFS) are crustal scale fault systems that control the SVZ. In this work, two very well exposed, meso-scale transects representing each system were studied with structural mapping, *in situ* 2D electrical survey, petrography, X-ray powder diffraction and scanning electron microscopy. Meso- and microstructural analyses suggest the LOFS exposure is dominated by repeated EW extensional (±shear) failure under a near-Andersonian strike-slip regime. The ALFS outcrop records two superimposed styles of failure: (1) NW shear (±extensional) in a near-Andersonian strike-slip regime and (2) NW extensional (±shear) likely developed under a non-Andersonian transtensional regime. Ca and Ca(-Na) zeolites occurring as vein networks mainly in the hanging wall of NW-striking normal faults indicate crystallization temperatures between 110-210°C and paleodepths between 2.1-3.5 km (assuming a 60-100°C/km temperature gradient). Electrical results suggest a significant positive correlation between zeolite amount (per area unit) and rock conductivity, which is greater in the core and hanging wall with respect to the unaltered andesitic host rock. Given stress fields for the SVZ, numerically modelled failure diagrams in the λ-σ space were constructed. In the LOFS exposure, extensional (±shear) failure likely occurs between typical ranges of pore fluid factors ($0.4 \leq \lambda_V \leq 0.48$). On the other hand, in the ALFS exposure, a switch from shear (±extensional) to extensional (±shear) failure is only possible at overpressures given by $\lambda_V \geq 0.6$-0.75 (λ_V >50-88% above cold hydrostatic pressure). Results suggest that long-term stress conditions favor: (1) the storage of increasingly overpressured fluids in hydrothermal reservoirs spatially associated with NW-striking ALFS faults, and (2) continuous localized fluid transport through vertical high-flux conduits in EW-striking faults of the LOFS. Development of geothermal systems in the SVZ requires major fault zones that both cumulate and transport hydrothermal fluids, which could be given by the interaction of the NW-striking and EW-striking faults of the ALFS and LOFS, respectively.

Key words: Southern Volcanic Zone, Liquiñe-Ofqui Fault system, Arc-oblique Long-lived Fault system, mode of failure, electrical resistivity, geothermal exploration, zeolites, fluid overpressure

1. INTRODUCTION

The generation and reactivation of geological faults and fracture networks creates and destroys permeability within the Earth's crust (e.g. Faulkner *et al.*, 2010 and references therein). Fault zone permeability influences the genesis of ore deposits, seismic/volcanic activity, and the spatial distribution and behavior of hydrothermal and geothermal systems at all scales (e.g Krupp and Seward, 1987; Sibson, 1989; Cole, 1990; Sillitoe, 2010).

The active Andean Margin is an exceptional natural laboratory that offers a unique set of on-going tectono-magmatic-hydrothermal systems, in which the interactions between fault systems, fluid flow and tectonic state of stress can be investigated. Amongst many other approximations, fluid redistribution accompanying faulting may be studied from classical structural methods or indirect observations such as electrical methods of the subsurface. In this work, I take both approaches, combining geological and geophysical information to propose a conceptual model for the formation of shallow hydrothermal systems in the Southern Volcanic Zone of the Andes (SVZ). In this manner, this work aims to contribute to the development of efficient strategies for geothermal exploration in one of the vastest, unexploited geothermal regions in the world.

1.1 Conceptual framework

In a general sense, a geological fault can be defined as a volume in the crust in which a relative movement between two competent masses of rock along a discontinuity called *fault plane* has occurred, due to natural stresses in the Earth's crust. When the fault plane is not perfectly vertical, two blocks can be distinguished: the hanging wall, above the fault plane, and the footwall, beneath the fault plane. The kinematics, or type of movement, can be classified as (Figure 1-1): (1) reverse movement, if the hanging wall moves up with respect to the footwall; (2) normal movement, if the hanging wall moves down with respect to the footwall; and (3) transcurrent or strike-slip movement, if the slip occurs in the horizontal direction and the fault plane is vertical. However, most of geological faults show combined kinematics (strike and dip components) and a complex reactivation story related to a changing stress field of the Earth (e.g. Rowland *et al.*, 2013). Due to the natural border condition in the Earth's surface, usually one of the principal stresses $\sigma_1 > \sigma_2 > \sigma_3$ is vertical (σ_V). Based on this, Anderson (1951) recognized three basic stress regimes in which different fault kinematics may develop. Normal faults occur when $\sigma_V = \sigma_1$, reverse faults occur when $\sigma_V = \sigma_3$ and strike-slip faults occur when $\sigma_V = \sigma_2$.

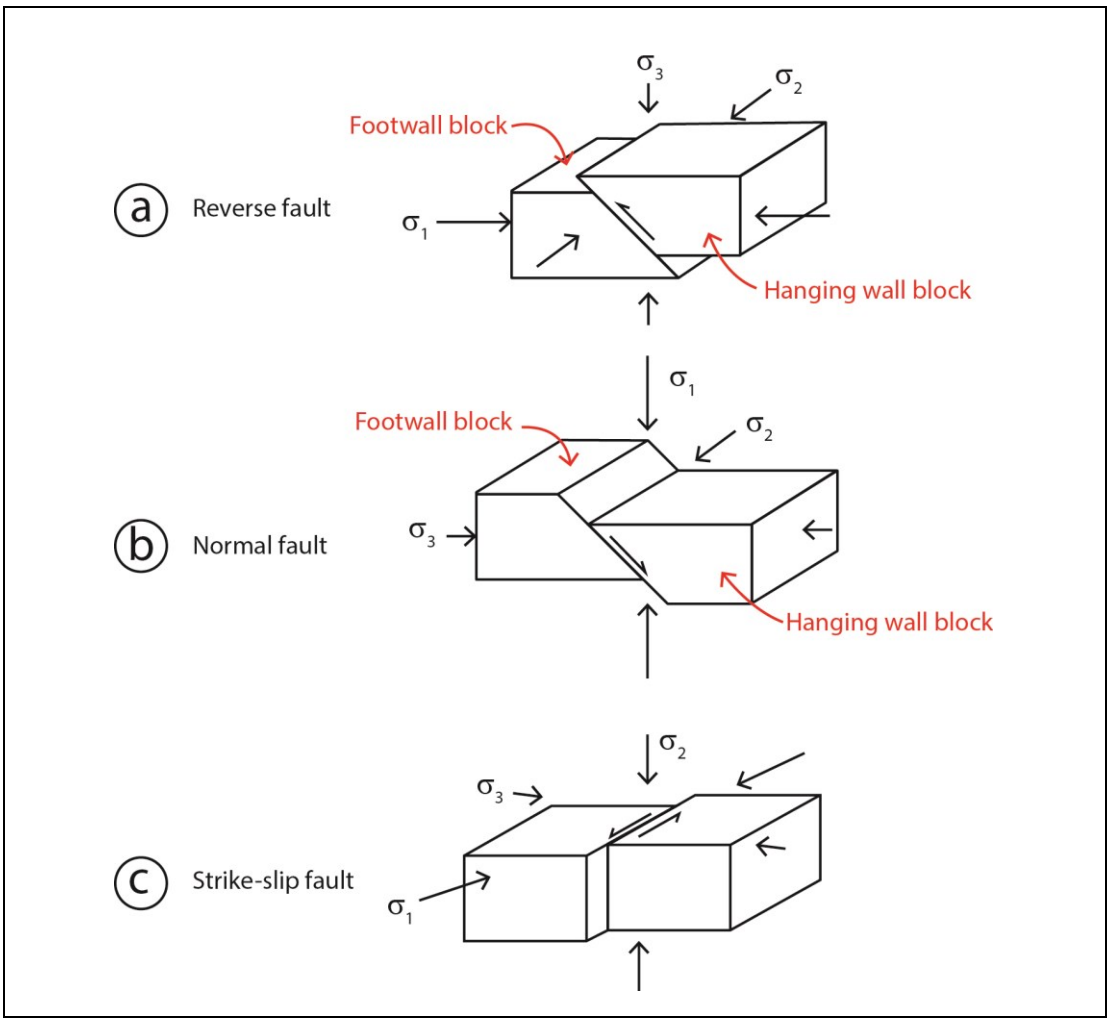

Figure 1-1. Fault types in the Earth's crust. a) Reverse fault: the hanging wall block moves up with respect to the footwall block. In an idealized stress regime the greatest principal stress σ_1 = vertical stress σ_V. b) Normal fault: the hanging wall block moves down with respect to the footwall block. The least principal stress $\sigma_3 = \sigma_V$. c) Strike-slip fault: blocks separated by the fault plane move parallel to the boundaries of the fault. The medium principal stress $\sigma_2 = \sigma_V$. Modified from Rowland *et al.* (2013) and Anderson (1951).

In practice, a fault cannot only express as a discrete surface, but as a volume called *fault zone*. From the point of view of its architecture, a fault zone is composed of a narrow core surrounded by a damage zone (Figure 1-2). The core is the volume of rock in which most of the strain is accommodated. The rocks that can be found in a

fault core, when it has formed at shallow depths (<10-15 km), are rocks such as cataclasites, breccias, or fault gouge (Sibson, 1977). In turn, the damage zone is the volume of rock surrounding the core that has been fractured due to the core's activity. Therefore, the rocks that can be found here correspond to the fractured host rock. The core can be simple, if there is only one zone where the strain was mostly accommodated, or multiple, if there is more than one (Faulkner *et al.*, 2003) (Figure 1-2a, b). Likewise, the damage zone can be symmetrical, if the distribution and number of fractures are similar along both sides of the fault core, or asymmetrical, if not (Sibson, 2003) (Figure 1-2c, d).

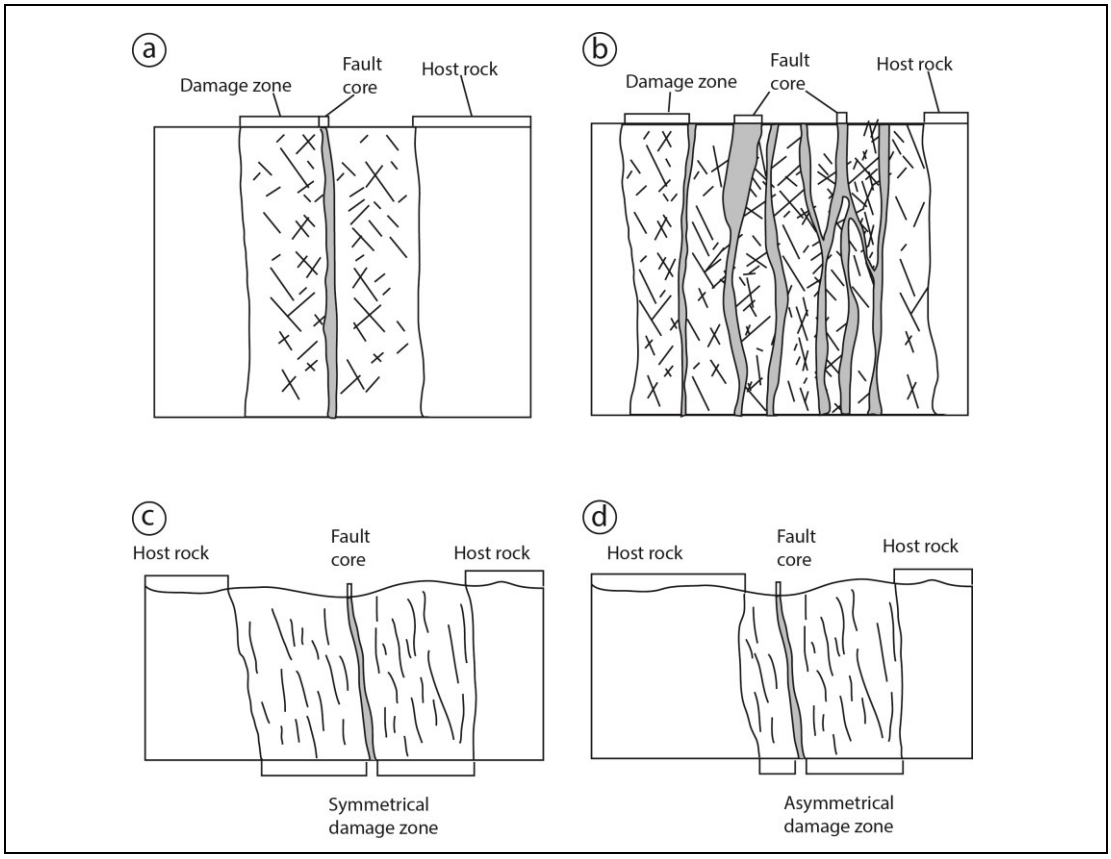

Figure 1-2. Fault zone architecture. a) Simple-core and b) Multiple-core fault zone (modified from Faulkner *et al.,* 2003). c) Symmetrical damage zone. d) Asymmetrical damage zone (modified from Sibson, 2003).

Permeability can be defined as the ability of a material to allow fluids to circulate through it without altering its internal structure. Fault zone permeability can be understood in terms of its primary permeability, which depends on the nature of the rock before failure; and in terms of the secondary permeability, that results from failure. Primary permeability is defined by the nature of the rocks in which pores may be interconnected or not. Secondary permeability, on the other hand, is defined by the formation of fractures due to interconnection of pores, and depends on whether the core or the damage zone is observed.

While the core can act as a conduit for fluid flow during seismic rupture, frictional decrease in grain size and mineral precipitation can turn this part of the fault zone in an impermeable barrier, so the core can act as (1) an along-dip conduit during rupture (Sibson, 1990) or (2) as an across-fault barrier in dormant, mature systems (Caine *et al.*, 1996). In this manner, depending on the stage of development of the fault zone, the core may lodge distributed or channelized fluid flow, which can lead to sealing on times scales commensurate to those of rupture recurrence (Morrow *et al.*, 2001).

Permeability of the damage zone is controlled by the orientation and frequency of micro and mesofractures, which depend on the lithology (cf. Main *et al.*, 2000, Balsamo *et al.*, 2010) and the orientation of the local stress field (Lunn and Wilson, 2008). Activation of fault zones can form fractures within the damage zone, where hydrothermal fluids may flow, leading to precipitation of hydrothermal minerals therein. This process, usually denominated *crack-seal episode* (Ramsay, 1980), may

increase permeability by orders of magnitude with respect to the sealed fault zone, during brief periods compared to the time scales of rupture recurrence (Brown *et al.*, 1998; Beeler and Hickman, 2004). For these reasons, fracture distribution within the damage zone of an outcropped fault zone can be used as an indicator of paleo-permeability of the system. Interestingly, GPS data and mechanical modeling demonstrate that, during a seismic event, when normal and reverse faulting occur, the hanging wall displaces more than the footwall block does (distances measured with respect to a horizontal plane) (Stein *et al.*, 1988; Biggs *et al.*, 2010) . For this reasons, fault-related damage may be greater within the damage zone in the hanging wall block.

Fluid redistribution accompanying fault zone activity depends on the macroscopic mode of brittle failure (Sibson, 1998; Cox, 2010). Three modes of brittle failure are possible: extensional, shear and extensional + shear failure (Sibson, 1998). Extensional failure, the most favorable style of deformation for fluid flow, occurs when open fractures form orthogonal to the least principal stress σ_3. Shear failure (faulting), the least favorable for fluid flow, happens when a movement parallel to the fracture boundary takes place. Extensional + shear failure, moderately favorable for fluid flow, involves the two previous kinds of failure. The type of brittle failure depends on three parameters (Sibson, 1998; Cox, 2010) : the pore fluid pressure (P_F), the difference between the greatest and the least principal stress (σ_1-σ_3) and the tensile strength of the rock mass (T). The prevailing effective stress field (σ_1'=σ_1-P_F >σ_2'=σ_2-P_F > σ_3'=σ_3-P_F) is related to the vertical stress (σ_V) by means of the pore fluid factor (λ_V), which can be defined as:

$$\lambda_V = P_F/\sigma_V \quad (1.1)$$

A value λ_V~0.4 is known as hydrostatic, and relates to a fault zone connected to the surface by a water column. This value is obtained dividing the weight of the water column to the rock column, assuming typical density values. A value λ_V~1 is known as lithostatic, and represents a fault zone in which the values of fluid pressure are high enough to equal the confining pressure. The combined effect of the pore fluid pressure, the difference between the greatest and the least principal stress, the tensile strength of the rock mass and the pore fluid factor on the failure mode can be conveniently represented in the pore fluid factor and differential stress space (Cox, 2010), equivalent to the Mohr's Circle. Failure envelopes in the $\lambda - \sigma$ space are excellent graphs that can be used to illuminate the role of fluid-pressure conditions and differential stresses in failure and permeability enhancement. In this graphs, red lines indicate failure in extension; green lines, failure in extension + shear; and blue lines, failure in shear. The rock will fail in the corresponding failure mode only when pore fluid factors and differential stresses reach the envelope. Below the envelope, the rock is elastically strained, but will not fail. Pore fluid factors and differential stresses above the envelope are not possible (Figure 1-3).

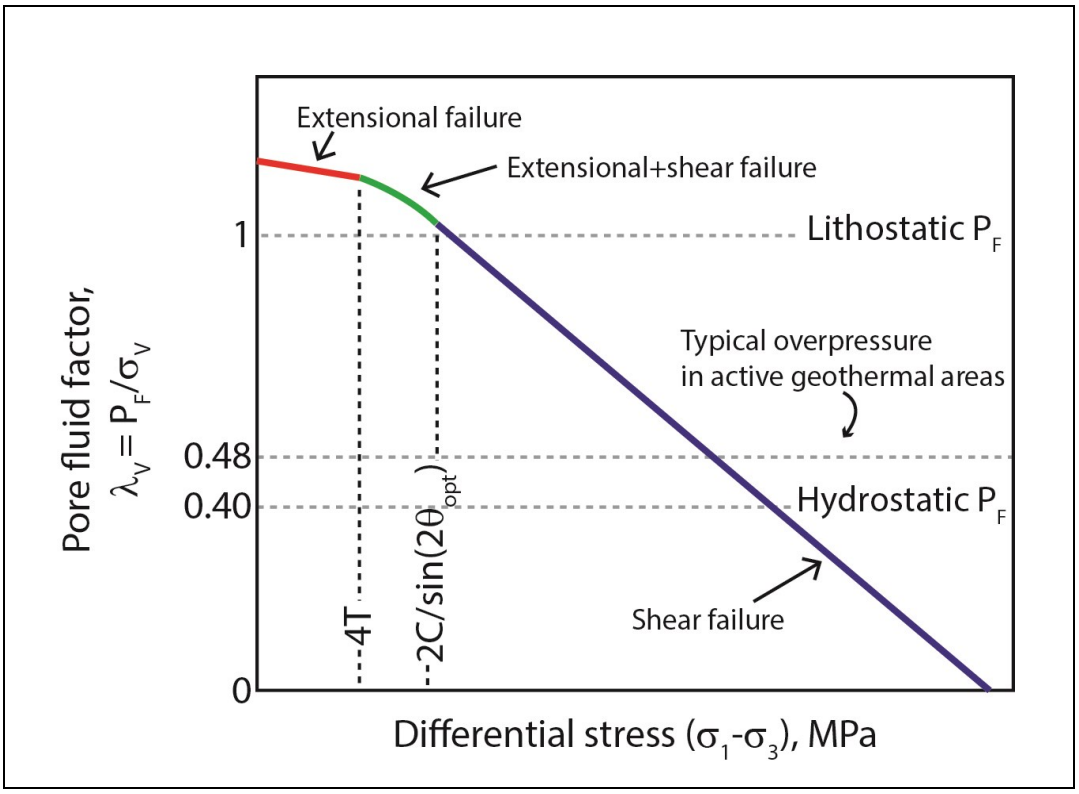

Figure 1-3. Generic failure mode diagram in the λ-σ space, for a given depth and tensile strength (T) (modified from Cox, 2010). The red line indicates failure in extension; the green line, failure in extension + shear; the blue line, failure in shear. The rock mass will only fail when the pore fluid pressures and the differential stress reach the envelope. Lithostatic and hydrostatic pore fluid factors are depicted along with typical over pressures in active geothermal areas (Rowland and Simmons, 2012). C = cohesion = 2T (Sibson, 2000), θ_{OPT} = maximum shear angle.

When hydrothermal fluids have circulated within fractures, hydrothermal minerals can precipitate therein. Minerals such as zeolites are common in many orogenic terrains, and are frequent products of the fluid-rock interaction between andesitic rocks and hydrothermal fluids at geothermal P-T conditions of temperature and pressures (Figure 1-4) (often <200°C, <50 MPa) (Cho *et al.*, 1987, Bish and Ming, 2001, Deer *et al.*, 2004, Weisenberger and Bucher, 2010, Dempsey *et al.*, 2014). From a geological point of view, zeolites can be used as very faithful monitors of the geological conditions, especially temperature conditions (Browne, 1978).

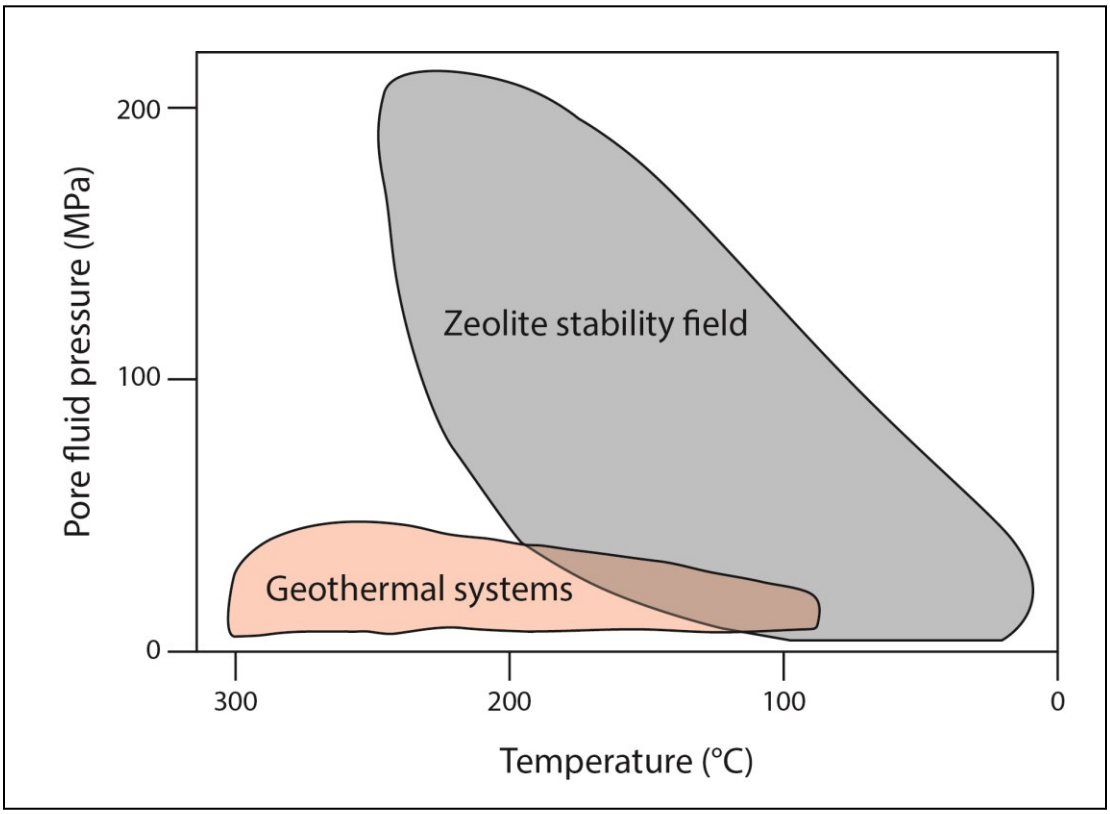

Figure 1-4. Geological conditions of crystallization (pore fluid pressure *vs*. temperature) within the zeolite stability field compared to those of the geothermal systems (Modified from Cho *et al.*, 1987).

On the other hand, water-filled fracture zones can be indirectly identified by electrical geophysical methods. The critical factor in the measured resistivity in shallow rocks is water content (Grant and West, 1965; Zohdy *et al.*, 1974; Revil *et al.*, 1998). Volcanic rocks such as andesites display ranges of resistivities between $10^{1.5}$-10^{5} ohm-m, whereas fractured, water-saturated andesites display resistivities within the range 1-10^{2} ohm-m (Figure 1-5) (Telford *et al.*, 1990, Ward, 1990). In this manner, hydrated, absorbent or adsorbent minerals occurring in filled fractures should behave as electrical conductors, similar to the documented behavior of clay sediments and fractured, water-saturated andesites (1-10^{2} ohm-m -Telford *et al.*, 1990).

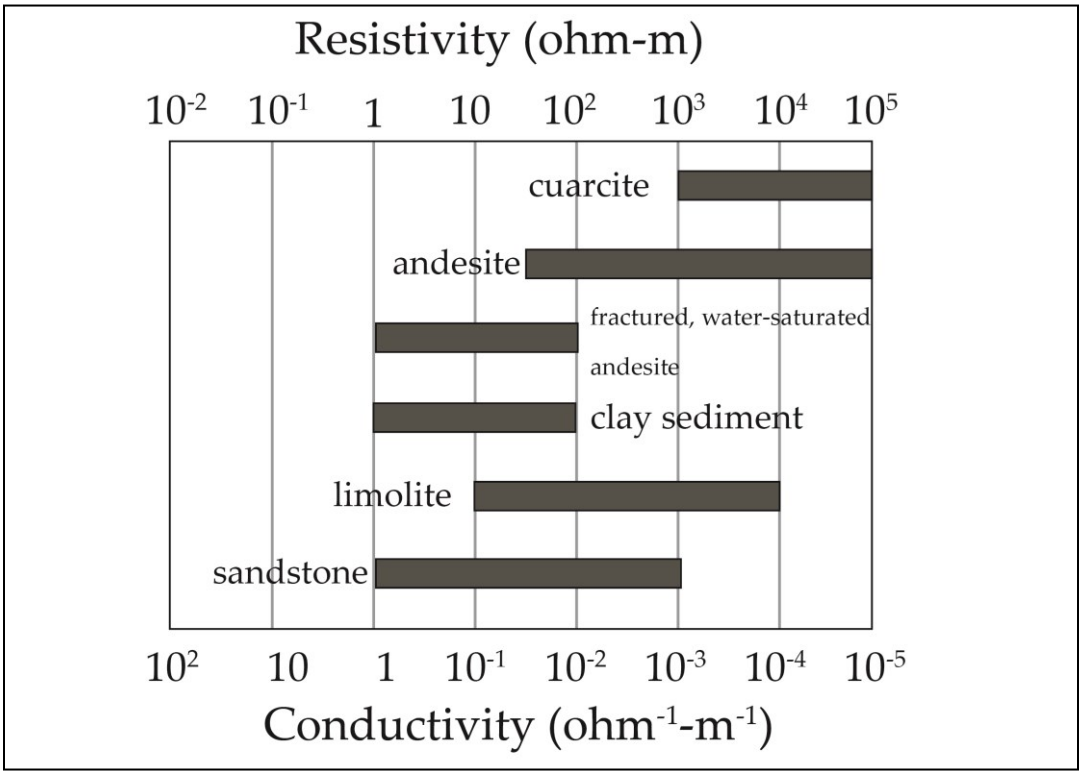

Figure 1-5. Ranges of electrical resistivity in common rocks and sediments (after Telford *et al.*, 1990, Ward, 1990).

In this thesis I used field structural mapping, X-ray powder diffraction (XRD), petrography, Scanning Electron Microscopy with Energy Dispersive Spectrometer (SEM-EDX), and a 2D geoelectrical survey in two outcrops that represent the major fault systems controlling the tectonics of the SVZ. These systems are the Liquiñe-Ofqui Fault System (LOFS) and the Arc-oblique Long-lived Fault System (ALFS). The previous techniques allowed determining architectural arrays that favor the development of shallow hydrothermal systems in the Southern Andes, candidates for geothermal exploitation. The nature of the deformation in such outcropped, fossil exposures of the LOFS and the ALFS was studied based on its textural, mineralogical

and electrical characteristics. The mode of failure of cm-width zeolite-bearing structures within the damage zone was determined, and then used to estimate plausible $\lambda - \sigma$ conditions for failure. Electrical measurements allowed the identification of the structural domains that concentrated fluid flow during fault zone activity. The union between structural, mineralogical and geophysical information allowed a better understanding of the relative roles of the LOFS and ALFS fault in the formation of shallow hydrothermal systems in the Southern Andes.

1.2 Geological setting

The Southern Andes show a trench-parallel segmentation, from west to east: (1) Paleozoic metamorphic rocks in the Coastal Range, (2) Oligocene-Recent sedimentary and volcanic deposits in the Central Depression, and (3) Paleozoic-Cenozoic plutonic and metamorphic rocks and Cenozoic volcano-sedimentary rocks as basement for the present volcanic arc in the Principal Range (Melnick and Echtler, 2006). The arc-parallel Liquiñe-Ofqui Fault System (LOFS) and the Arc-oblique NW to WNW-striking Long-lived Fault System (ALFS) constitute the main structural features in the Southern Volcanic Zone of the Andes (SVZ) (33-46°S) (Lavenu and Cembrano, 1999; Rosenau *et al.*, 2006; Sánchez *et al.*, 2013). At least from *ca.* 25 Ma, these structural features have been controlled by the subduction of the Nazca and Antarctic plates beneath the South American continental plate (Somoza and Ghidella, 2005) (

Figure 1-6a).

The arc-parallel LOFS is an active *ca*. 1200 km long Cenozoic intra-arc, strike-slip fault system, that strikes NS to NNE in its master traces and NE in its subsidiary traces, forming a strike-slip duplex with dextral and dextral-normal movement mostly developed in the last 6 Ma (e.g. Cembrano *et al.*, 1996; Arancibia *et al.*, 1999; Lavenu and Cembrano, 1999; Folguera *et al.*, 2002). The LOFS displays a kinematics compatible with strain partitioning due to the decomposition of the convergence vector: (i) NS to NNE-striking master traces accommodate the margin-parallel component, and are consequently favorably oriented for dextral shear; and (ii) the NE subsidiary traces accommodate the margin-orthogonal component, and are therefore favorably oriented for transtensional failure (Arancibia *et al.*, 1999; Lavenu and Cembrano, 1999; Cembrano and Lara, 2009).

The margin-oblique ALFS is a fault system related to a family of crustal lineaments transverse to the main volcanic arc (Salfity, 1985; Cembrano and Lara, 2009; Rivera and Yáñez, 2009; amongst others). The ALFS is apparently older than the LOFS, and is at least present between 25°30'-41°S (e.g. Taylor *et al.*, 1998, Rivera and Cembrano, 2000, Moreno *et al.*, 2011, Aron *et al.*, 2013). The ALFS is probably related to the tectonic segmentation of the Andes, emplacement of NW-striking intrusive bodies, control of Paleozoic-Mesozoic volcanic and volcano-tectonic episodes, and genesis of one or more NW to WNW basins oblique to the actual Andes, at least from the Mesozoic to the recent (Rivera and Cembrano, 2000). Its precise geometry and kinematics are still open to debate. Nevertheless, seismic and field evidence indicate that these faults record alternate phases of: (1) sinistral,

sinistral-normal and sinistral-reverse kinematics (e.g. Moreno *et al.*, 2011), and (2) normal kinematics (e.g. Lange *et al.*, 2008; Melnick *et al.*, 2009).

The area of study, located in the northernmost termination of the LOFS, has been described as an active, east-branching "horse-tail" fan, with faults that strike NE, progressively becoming EW towards the east, accommodating transtensional to purely extensional deformation (Reuther *et al.*, 2003, Rosenau *et al.*, 2006) (Figure 1-6a). The northern tip of the LOFS spatially and temporarily interacts with the ALFS (e.g. Sánchez, 2015). The studied outcrops, one of each fault system, correspond to two *ca.* 100-m-long sections located at about 15 km SE of the locality of Lonquimay (*ca*. 38°20'S) (Figure 1-6b). Here, the LOFS and the ALFS cut andesitic Miocene rocks, with K-Ar ages that vary between 20-11 Ma (Suárez and Emparán, 1988, 1995) (

Figure 1-6b). The oldest rocks in the study area are Jurassic monzogranites, diorites and tonalities (K-Ar ages between 148±8 and 23±2 Ma), and pyroclastic-andesitic Cretaceous rocks (K-Ar ages between 73.5±5 and 13±3.2 Ma). These rocks are intruded by Miocene monzogranites and granodiorites (K-Ar ages between 15.2±3 and 7.2±1.9). Above the described units there are quaternary deposits of unconsolidated, undifferentiated sediments interlayered with pyroclastic horizons (all descriptions and ages from Suárez and Emparán, 1997).

Some authors have suggested that activation of crustal fault zones in Chile is controlled by the Andean Earthquake Cycle, that has two distinctive stages: (1) the interseismic period (*Andean interseismic*), in which the prevailing stress field is

produced. This period occurs between each megathrust interplate earthquake (*ca.* M_W>8), and the continental plate is compressed; and (2) co- and postseismic period (*Andean co- and postseismic*), in which a transient change of stress field within the continental plate is induced. This period occurs during and after a megathrust earthquake, and a relaxation of the continental plate takes place. Seismic evidence suggests that normal rupture of crustal NW-striking faults could be produced by high Coulomb stress change after large interplate earthquakes, enhanced by fluid presence, as observed in the Pichilemu fault in after the Maule earthquake in 2010 (Farías *et al.*, 2011, Aron *et al.*, 2013). The active Andean Margin is an exceptional natural laboratory for investigating the interactions between fault systems, fluid flow and tectonic state of stress because the Andean Earthquake Cycle and the kinematics of the major fault systems are reasonably well understood, and because fault zones are locally very well exposed.

The LOFS and ALFS faults constitute contrasting magmatic-tectonic-hydrothermal domains (e.g. Cembrano and Lara, 2009; Sánchez *et al.*, 2013; Sánchez, 2015), which have been interpreted to play different roles in magma transport under the prevalent stress conditions: (1) the NE faults of the LOFS are favorably oriented for transtensional reactivation, promoting rapid ascent of undifferentiated, basaltic magma in channelized fluid paths; and (2) the NW to WNW-striking faults of the ALFS are severely misorientated with respect to the prevailing stress field, promoting long-term residence of differentiated, riolitic magma reservoirs.

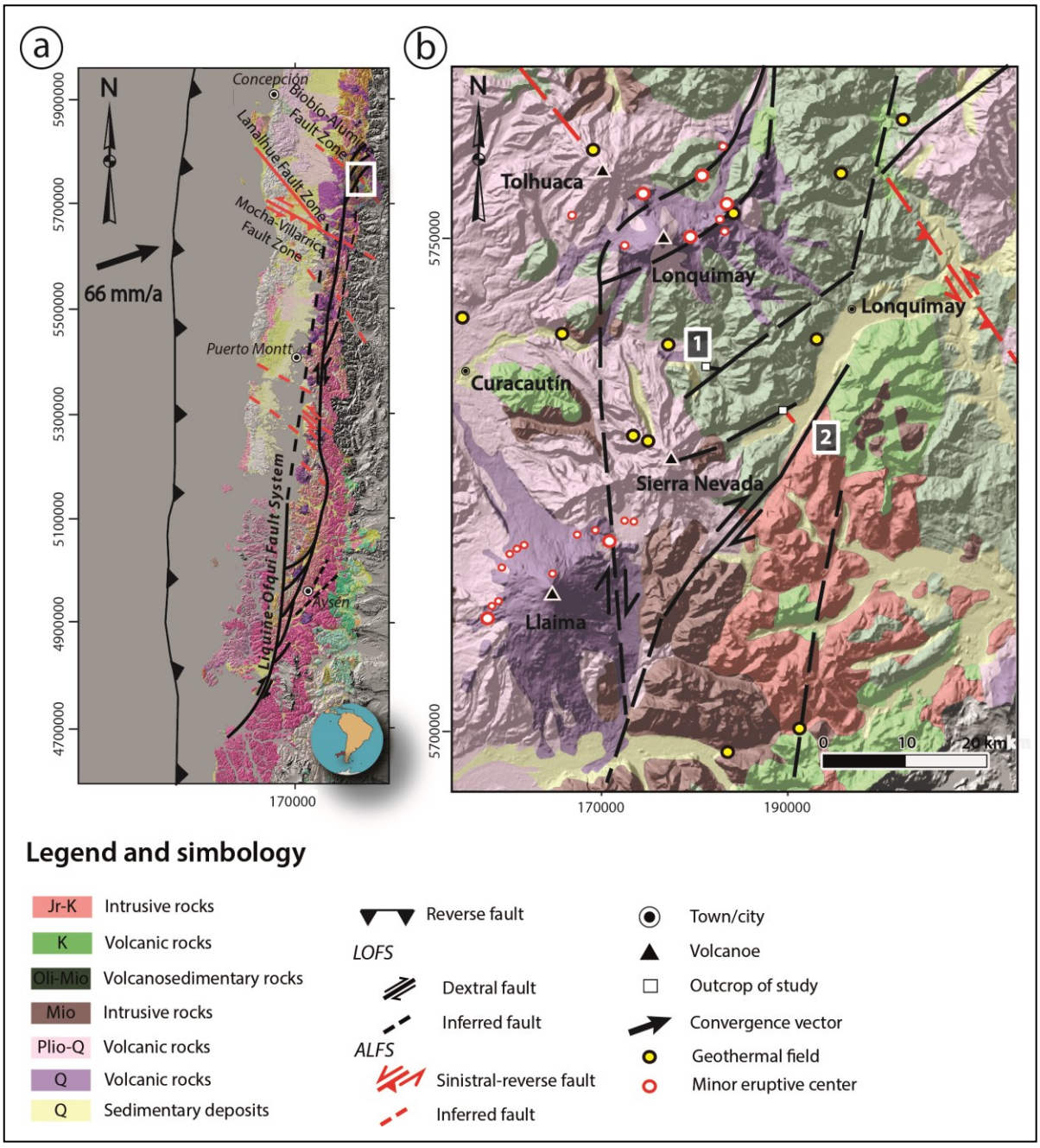

Figure 1-6.a) Liquiñe-Ofqui Fault System (LOFS, black line) and Arc-oblique Long-lived Fault System (ALFS, red line). The arrow represents the convergence vector (66 mm/a). Modified from Sánchez *et a*l. (2013). b) Geological context of the outcrops of study, indicated in white squares as outcrops 1 (LOFS splay fault) and 2 (ALFS segment). Modified from Pérez-Flores *et al.* (2015).

1.3 Hypothesis

The hypotheses of this work are:

a) The LOFS and the ALFS play different roles in the circulation and storage of shallow fluids. Long-term stress conditions promote circulation of fluids in the EW-striking faults of the LOFS, and storage in the NW-striking faults of the ALFS.

b) The geological conditions of crystallization (temperature and depth) of the hydrothermal minerals within fractures in the damage zones of the LOFS and ALFS are consistent with shallow hydrothermal alteration (<250°C, <10-15 km).

c) Electrical resistivity of the different structural domains and their associated host rocks are distinguishable. Conductivity is controlled by the spatial distribution of fault-related mineralogy, and since secondary (hydrothermal) minerals preferentially occurs in filled fractures within the damage zone and the core, these zones will have a different conductivity with respect to a non-fractured host rock.

1.4 Objectives

The general objective of this work is to constrain architectural arrays (geometry and damage) that favor the development of shallow hydrothermal systems.

The specific objectives of this work are: (1) to determine the style of deformation involved in the different faulting episodes of the studied exposures; (2) to establish the geological conditions of the paleofluids (crystallization temperature and conjectural depth of formation) registered in the mineral assemblages along the

studied fault zones; (3) to correlate the electrical resistivity and the architecture of a fault zone, for the case of study.

2. METHODOLOGY

In order to achieve the proposed objectives, two very well exposed, representative outcrops in the northernmost tip of the LOFS were selected, where this system spatially and temporarily interacts with the ALFS. In both outcrops –one of each fault system- a 22-m-long transects was studied in three field trips (summers of 2014 and 2015: 41 days in total). The location of the outcrops is *ca.* 10 km S of the Lonquimay Volcano, IX Region of the Araucania, Southern Andes, Chile.

2.1 Structural Mapping

In each locality, the structural mapping was made in two transects orthogonal to strike of the fault zone of interest: one of them was orthogonal to a local splay fault of the LOFS and the other was orthogonal to a specific segment of the ALFS (Figure 1-6b). Structural mapping consisted of:

(1) Determining the geometrical attitude (i.e. spatial orientation) of the core and the discontinuities of the damage zone, using a geological compass. The geometrical attitude (strike, dip) of geological objects constitutes the basis for spatial and geometrical analyses (section A.1 in Appendix A);

(2) Determining the orientation, the pitch angle (or rake) and the sense of shear on slip surfaces in the damage zone (normal, reverse, dextral, sinistral or any combination), using a geological compass and brittle kinematic indicators (following Petit, 1987) (section A.2 in Appendix A);

(3) Meso-scale description of the textures and cross-cutting relationships in discontinuities within the damage zones (section A.3 in Appendix A). Such discontinuities are here referred to as structural elements, whose classification

was based on their mesoscopic internal texture (e.g. (Jébrak, 1997, Bons *et al.*, 2012)). To avoid ambiguity, the term *hydrothermal breccia* will be used here to refer to any structural element composed of clasts cemented in a hydrothermal matrix.

The percentage of hydrothermal mineralogy in each structural domain (core and damage zone), was estimated using an areal index. For the damage zone within the hanging and footwall blocks, such index was calculated as following:

$$\delta_x = \Sigma A_i / A_T \quad (2.1)$$

where:

δ_x = areal proportion of hydrothermal mineralogy of the hanging or footwall block (δ_H and δ_F, correspondingly)

A_i = area of each individual structural element

A_T = total area of the hanging wall or footwall block

Both A_i and A_T were obtained considering rectangular surfaces. Both areas were calculated multiplying a length given by the structural mapping and an arbitrary height of 1 m. In particular, the length of all structural elements occurring in the damage zone was approximated by a characteristic width of 0.02 m. In this manner A_i = 0.02 m^2 for each structural element and the previous equation can be re-casted as follows:

$$\delta_x = n*0.02 / A_T \quad (2.2)$$

Where: n = number of structural elements within the hanging or footwall blocks

On the other hand, for the core, the index was calculated as following:

$\delta_c = A_c * p$

Where:

δ_c = areal proportion of hydrothermal mineralogy of the core

A_c = area of the core

p = proportion of hydrothermal mineralogy within the core (obtained from diffractogram analysis. For more information, see section 2.3).

Just like in the case of the damage zone, A_c was calculated multiplying a square surface, whose length is given by the structural mapping and its height is arbitrary and equal to 1 m.

The linear fracture density of macroscopic fractures (λ_x) was determined by calculating the ratio:

$$\lambda_x = n/L_x \quad (2.3)$$

Where n = number of discontinuities intersecting along a vertical plane perpendicular to the corresponding fault core, and

L_x = length of the core, hanging wall or footwall block (L_C, L_H and L_F, correspondingly).

2.2 Microstructural analysis

Thins sections are thin slices of rock (usually 30 μm thick) mounted on a microscope slide. Oriented thin sections are slices where the geometrical attitude of the sample is known. The microstructural analysis was made using the petrographic microscope (cf. with Appendix B) and it was complemented with a Scanning Electron

Microscope with Energy Dispersive X-ray Spectrometer (SEM-EDX) (cf. with Appendix C).

In this study, two types of samples were analyzed: (1) non-oriented thin sections (2 samples of the LOFS exposure, 1 sample of the ALFS exposure); and (2) thin sections oriented perpendicular to the foliation and parallel to the lineation (XZ section of the strain ellipsoid of Simpson and Schmid, 1983), where it is possible to observe representative textures of the deformational events (Figure 2-1a, b) (3 samples of the LOFS exposure and 3 samples of the ALFS exposure).

The analyzed thin sections correspond to 3 of the 5 structural elements defined in the damage zones: (1) hydrothermal breccia (1 sample of the LOFS exposure and 2 samples of the ALFS exposure); (2) vein (2 samples of the LOFS exposure); and (3) vein-fault (1 sample of the ALFS exposure). Despite a total of 6 oriented thin sections were studied, 3 representative samples were selected to make a detailed microstructural map of each one (1 hydrothermal breccia of the ALFS exposure, 1 fault-vein + 1 vein of the LOFS exposure). The confection of the microstructural maps involved the creation of a photomosaic of approximately 150 pictures per map, taken under the petrographic microscope (XPL – 2.5x). The microstructural classification of the veins within such samples was based on the morphology and growth direction of the crystals, being only distinguished syntaxial veins, characterized by having crystals growing out from the country rock towards a median zone, or from one boundary towards the other (Bons et al., 2012). The occurrence of a syntaxial vein is related to at least one crack-seal episode (Ramsay, 1980, Wilson, 1994).

The preparation of non-oriented and oriented thin sections basically follows the same procedure, with the one difference that the slices oriented thin sections were oriented perpendicular to the foliation and parallel to the lineation (XZ section of the strain ellipsoid of Simpson and Schmid, 1983), The fragile samples were covered with polyester resin, and were cut using a circular cut-off saw from which a chip of rock is obtained. The chips were sent to the Thin Sections Laboratory, in the Universidad de Chile, where the polished and unpolished thin sections were made, using epoxy glue (index of refraction = 1.54) (Figure 2-1c).

Additionally, I analyzed 6 of the polished oriented thin sections using SEM-EDX. Sample preparation involved covering the selected thin sections with a conductive coating of carbon, which promotes better elemental analysis. The analyses were performed in the SEM-EDX Laboratory of the Universidad de Chile, using a FEI Quanta 250 SEM.

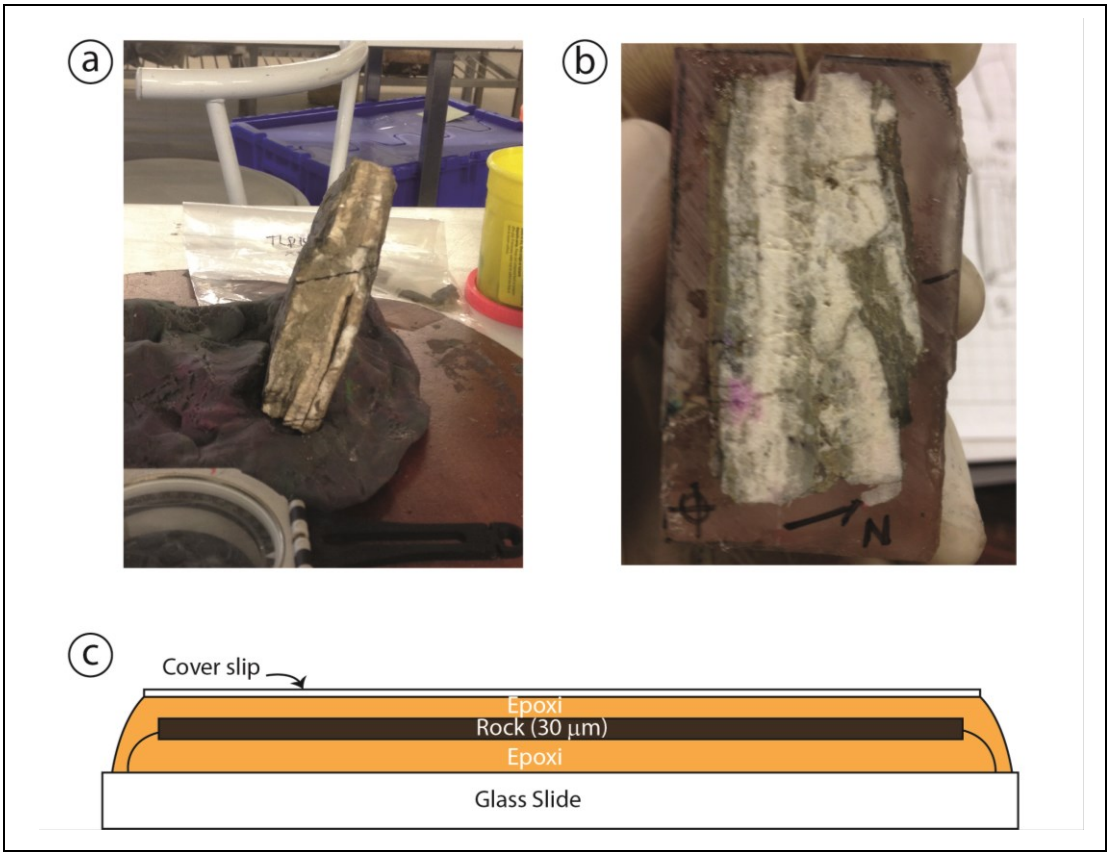

Figure 2-1. Sample preparation for optical microscopy. a) Sampled were marked in the plane of interest. b) Example of oriented sample already cut. c) Schematic cartoon showing a thin section.

2.3 X-Ray powder Diffraction (XRD)

X-ray powder diffraction analysis (XRD) is a classical technique utilized to determine the unknown mineral composition of sample (for more details see Appendix D). In this study, a total of 60 samples of structural elements within the damage zones were collected for XRD analysis.

Sample preparation was carried out following the methodology proposed by Bish and Post (1989). The unknown mineral was ground to a fine particle size (<10 μm) using an agate mortar (Figure 2-1a, b). The resulting mono- or polycrystalline material was dissolved in water and placed in a 2x2 cm^2 square

sample holder (Figure 2-1c). Once the sample was dry, where they were analyzed using a diffractometer. Samples were analyzed in the Crystallography Laboratory of the Department of Physics, Universidad de Chile. A Bruker D8 Advance X-Ray Diffractometer was used (Figure 2-1d) (radiation Cu Kα=1.5406Å), equipped with a Cu X-Ray tube (operating at 40kV/30mA), Ni filter, sample spinner and a solid state detector (Lineal LynxEye). The Bragg-Brentano geometry was used.

The interpretation of the resulting diffractograms (e.g. Figure 2-1e) was performed using the software Match!. The logic beneath the interpretation is that the interatomic spacing of each mineral is unique, generating a set of unique peaks in the diffractogram. Once all the peaks have been identified and background noise effects were diminished, a systematic procedure was used to assess mineral identification (Bish and Post, 1989): (1) the interatomic spacings were ordered in terms of their intensity beginning with the most intense peak; (2) software-driven automated search/match routines helped in the comparison of the interatomic spacings of the unknown mineral to those of known minerals, using the Panalytical-ICSD (Inorganic Crystal Structure Database) database; (3) matching mineral phases were determined by visual comparison and geological context; (4) the diffractogram was totally interpreted when no unidentified peaks remained in the diffractogram.

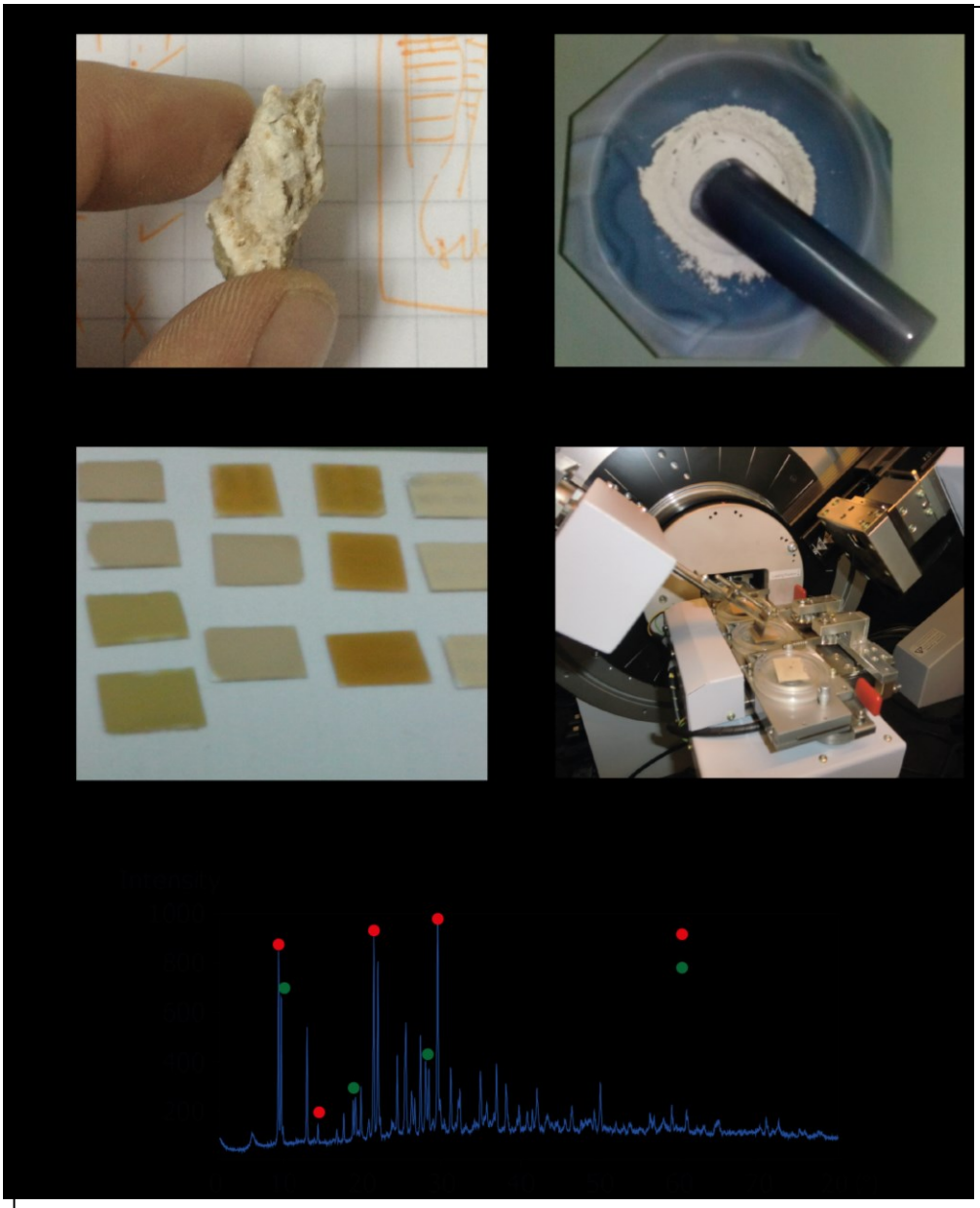

Figure 2-2. Sample preparation for X-ray diffraction analysis (XRD). a) Intact sample. b) Sample ground to a particle size <10mm. c) Samples mounted on the sample holder. d) Diffractometer. e) Example of diffractogram (sample LR8.4 - LOFS exposure).

Semi-quantitative data of the composition of the core were obtained using the normalized Reference Intensity Ratio method (Chung, 1974). The reported XRD abundances may have an error ranging from ±1% to ±5% depending on

the quantity and type of minerals in the powder (e.g. phyllosilicates and clay minerals may be overestimated due to their preferred orientation).

2.4 2D electrical survey

2D electrical survey is a geophysical method that seeks to obtain an apparent resistivity section of the subsurface using the Ohm's law and the Maxwell's equations (Telford *et al.*, 1990), under the assumption that electrical properties of the Earth can be described as a two-dimensional resistivity function $\rho=\rho(z,x)$ depending on the depth z and the horizontal position x (e.g. Zhdanov, 2009).

In this work, a 2D electrical survey was conducted in two 20-m-long transects orthogonal to the corresponding fault core of the selected exposures of the LOFS and the ALFS. Appendix E illustrates about the basics of the 2D electrical surveys.

The electrical measurements were undertaken using the multi-electrode device TIGRE, that belongs to the department of Structural and Geotechnical Engineering at the Pontificia Universidad Católica de Chile. This equipment has 32 electrodes, and potential-current measurements are controlled by the software ImagerPro2006. The field installation considered deployments for each outcrop, using the Schlumberger and dipole-dipole configurations: (1) one with the electrodes directly installed in a vertical wall of rock, which gives a resistivity profile in plan view (Figure 2-3a); and (2) with the electrodes installed in the ground, which provides a cross-section resistivity profile (Figure 2-3b). In the case of the electrodes directly inserted in the rock, the

installation of the electrodes was made after drilling the rock and injecting a conductor gel to increase the contact area and the resistivity of the electrodes (Figure 2-3c-e), modifying an idea developed by Araya (2005). This conductor consisted of a prepared solution of 10% volume fraction of NaCl + 10% volume fraction of collagen. The viscosity of the gel prevented it to get out the drilled holes. In the case of the electrodes installed in the ground, the contact resistivity was increased using a solution of 10% volume fraction of NaCl.

In each installation of electrodes, two electrical lines were overlapped with the objective of getting a better spatial resolution of the zones of interest. The dipolar distance was 0.5m and for each line, that consisted of 32 electrodes, and 23 electrodes were overlapped. This gives a total studied length of 20m for each type of installation (rock and ground).

With the apparent resistivity section, the data were inverted to obtain a geoelectrical mesh using the software ImagerPro 2006. Final resistivity models were obtained employing that mesh and interpolating by Minimum Square using the software Oasis Montaj. The statistical analysis was made using the software R. With the finality of testing the geoelectrical behavior of the fault zones, electrical domains were defined in the inversion resulting from the installations of the electrodes in the wall of rock. Such domains were determined using the architecture of the main structural domains (core and damage zone – the last subdivided in the hanging and footwall blocks), obtained from the structural mapping, and considering that the first centimeters of the vertical walls of rock are exposed to weathering effects. The analysis of the resistivities involved two approaches: (1) a quantitative statistical

comparison of the structural domains, and (2) a qualitative comparison of the spatial distribution of the resistivities within such domains.

Figure 2-3. Field installation for the 2D electrical survey. a) Example of installation of the electrodes in a vertical wall of rock (LOFS exposure). b) Example of installation of the electrodes on the ground (LOFS exposure). c) Installation in the vertical wall of rock involved drilling, d) injecting a conductor gel and e) insert the electrodes in the wall.

3. RESULTS

3.1 Fault zone architecture

From an architectural point of view, the LOFS outcrop has a simple core and an asymmetric damage zone, with a higher fracture density in the hanging wall (4.80 fractures/m), than in the footwall (1.51 fractures/m) (Figure 3-1a, b). The N83°W/65°SW core has a width of 0.4 m, and is composed of a microdioritic dyke with fault gouge in its borders. The damage zone within the hanging wall block extends 5 m away from the core to the SSE, whereas in the footwall extends for 15 m to the NNW. The structural elements in both blocks display N10-80°E/75-85°S. NNE to ENE-dextral and dextral-normal slip surfaces (inferred from brittle kinematic indicators such as steps and quartz and calcite mineral fibers, e.g. Petit, 1987) show rakes that vary between 10-50° from the NE.

On the other hand, the ALFS outcrop (Figure 3-1c, d) exhibits a simple core and an asymmetric damage zone, defined by the distribution and intensity of fractures. Fracture density within the hanging wall block (3.53 fractures/m) is greater than in the footwall (2.18 fractures/m) and the damage extends further from the core. The N45°W/60°SW core has a width of 0.5 m, and is composed of foliated gouge with S-C internal structure consistent with normal movement. The boundaries of the core also exhibit slip surfaces with reverse and sinistral-reverse sense of movement recorded in brittle kinematic indicators as steps (e.g. Petit, 1987).

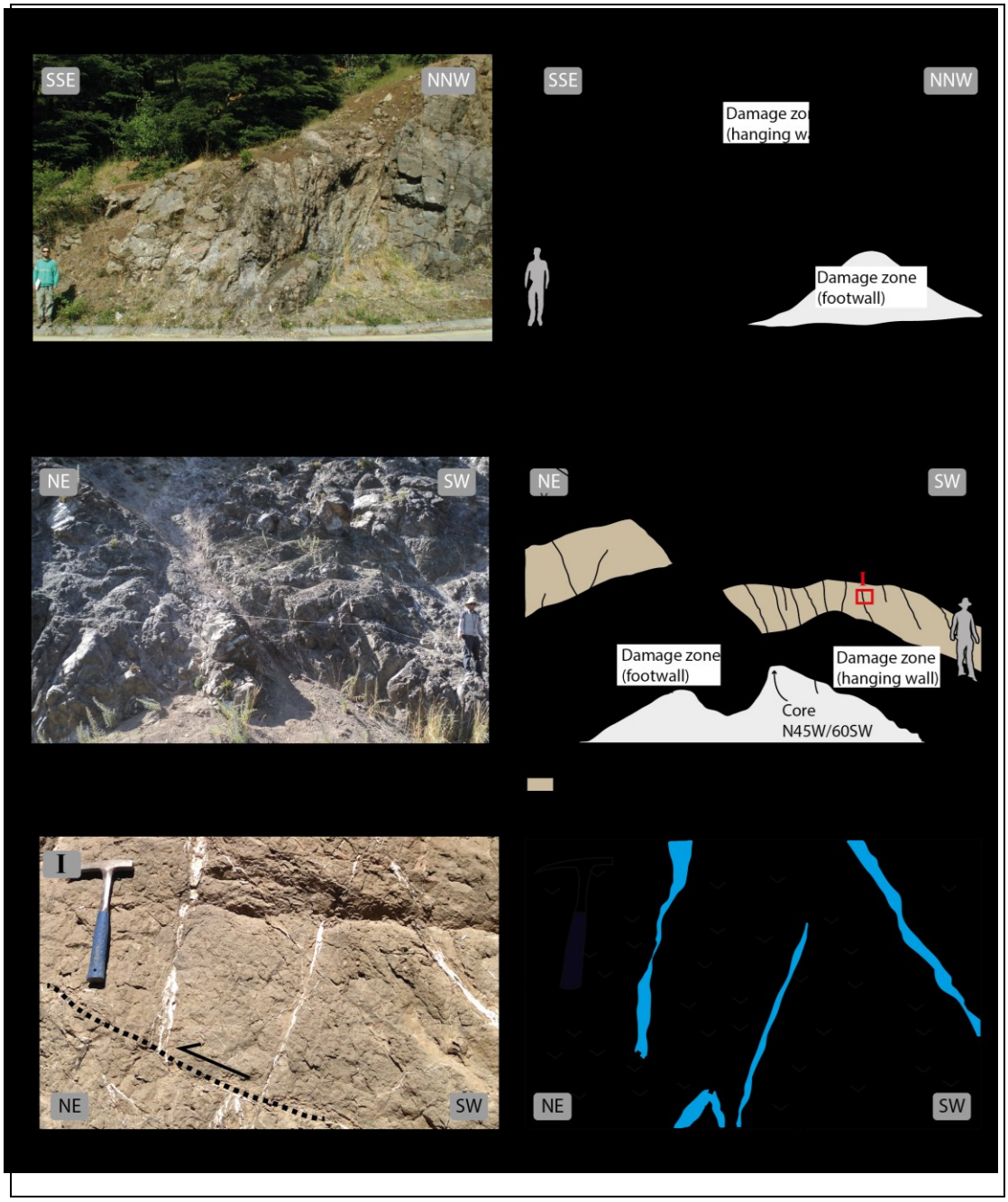

Figure 3-1. a) Photography of the studied splay fault of the LOFS (cross section, picture looking to the WSW). b) Cartoon of the LOFS exposure, showing the fault core (microdioritic dyke with fault gouge in its borders), the damage zone (dominated by NNE-ENE/subvertical discontinuities) and the protolith. c) Photography of the studied segment of the ALFS (cross section, picture looking to the SE). d) Cartoon of the ALFS exposure, showing the fault core (foliated gouge consistent with normal movement) and the damage zone (dominated by NW/subvertical discontinuities). The red square indicates the schematic positions of figures 2e, f. e) Example of NW/gently dipping faults cutting and separating NW/subvertical discontinuities. f) Cartoon of situation in letter (e).

In addition, NW/gently dipping-shear surfaces occur in the borders of the fault core, cutting and displacing NW-striking mm-width veins, with a reverse centimetric separation (Zone I in Figure 3-1d-f). The damage zone within the hanging wall block extends 15 m away from the core to the SW, whereas in the footwall extends for 5 m to the NE. Within both blocks mostly NW/subvertical structural elements occur. Additionally, N5-15°W/subvertical sinistral shear surfaces can be found within the hanging wall, having rakes <10° from the S.

The areal proportion of hydrothermal mineralogy in the different structural domains (calculated as shown in Section 2.1) is summarized in Table 3-1. In both outcrops, the biggest percentages are in the core (δ_C=12-37.5%), one order of magnitude more than the hanging and footwall blocks (δ_H=7.10 -9.60% and δ_F=2.90-5.60%).

Table 3-1. Areal proportion of hydrothermal mineralogy within the different structural domains of the LOFS and ALFS exposure. δ_C = core, δ_H = hanging wall block, δ_F = footwall block.

Outcrop/proportion of hydrothermal mineralogy	δ_C	δ_H	δ_F
LOFS exposure	12.00%	9.60%	2.90%
ALFS exposure	37.50%	7.10%	5.60%

3.2 Structural elements within the fault zones

The different tabular structural elements that occur in the analyzed damage zones have a wide variety of internal textures, summarized in Figure 3-2 (complete dataset in Appendix F). Regardless of the type of structural element, almost all

discontinuities in the damage zones of the LOFS and the ALFS outcrops are associated with zeolite precipitation and, as it will be discussed in the next sections.

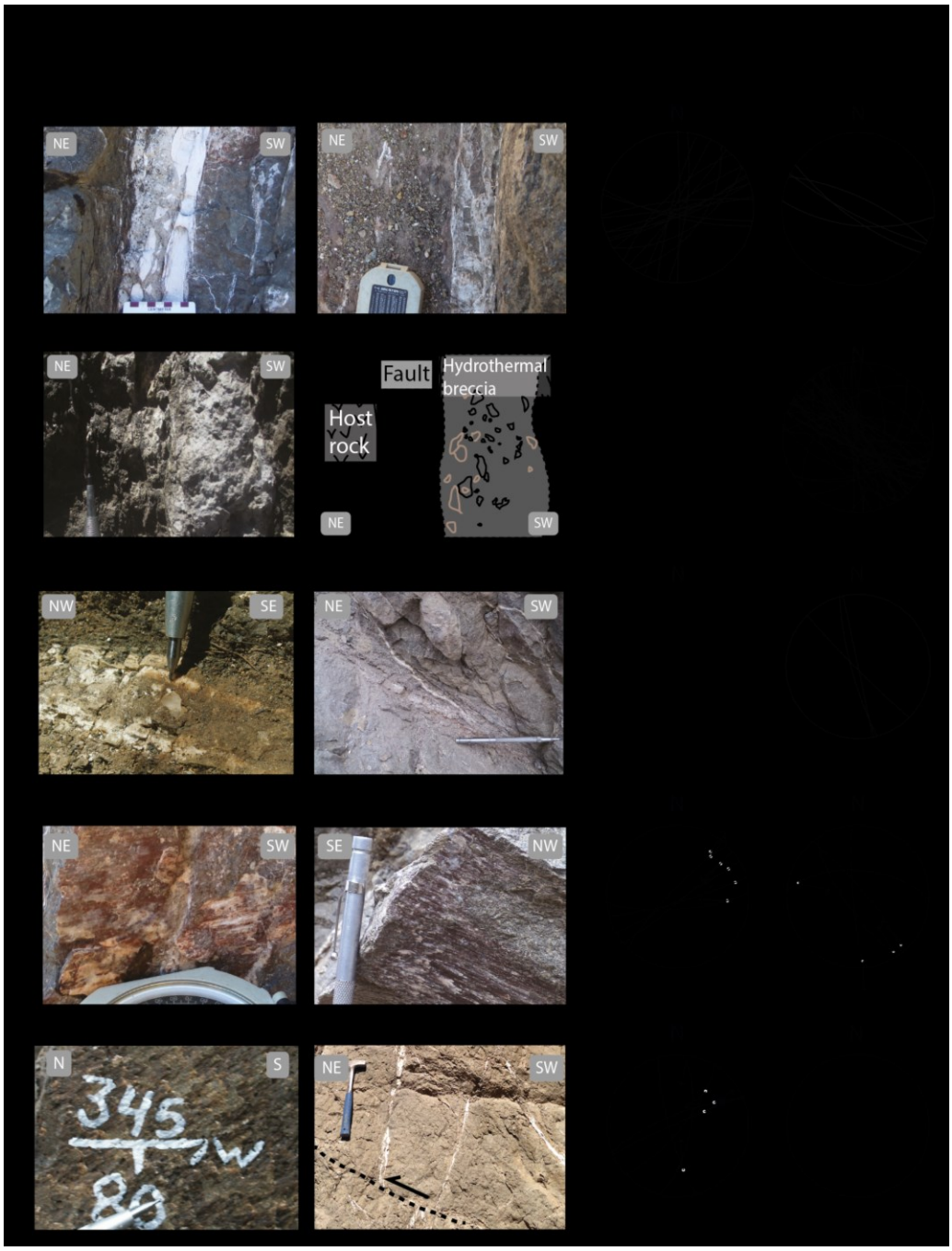

Figure 3-2. Left, examples of the structural elements occurring in the LOFS and the ALFS exposures. Right, geometry of the structural elements. a) Hydrothermal breccias are here defined as any structural element that has clasts cemented by a hydrothermal matrix (pictures are cross sections, looking to the SE).

Five families of structural elements were identified in the studied fault zones: (1) hydrothermal breccia; (2) fault-localized hydrothermal breccia; (3) vein; (4) fault-vein; and (5) fault. All of these structural elements have tabular shape, and a width/length ratio <0.001. The detailed description of each structural element is the following:

a) Hydrothermal breccia (LOFS n=16, ALFS n=4)

These tabular discontinuities are composed of subangular clasts of the host rock and/or hydrothermal clasts, in a fine matrix of hydrothermal minerals (Figure 3-2a).

In the LOFS exposure, hydrothermal breccias are present in both the footwall and the hanging wall, and have widths on the cm-scale, with along dip continuity >5m. The boundaries of the hydrothermal breccias strike between NNE and ENE, with high angle dips preferentially to the S. Some of these elements exhibit kinematic indicators of dextral and dextral-normal shear, with rakes <30° from the NE.

---

b) Fault-localized hydrothermal breccia is distinguished from hydrothermal breccia since the latter is contained in a cm-to-mm width discontinuity with cataclastic fabric, as shown in the cartoon to the right of the picture (picture is a cross sections, looking to the SE). c) Veins are filled of equant milimetric crystals without any preferred orientation (picture to the left is a plan view, picture to the right is a cross section, looking to the SE). d) Fault-veins are here defined as structural elements with evidence internal shear and mineral precipitation (mainly quartz and calcite) (pictures are cross sections, picture to the left, looking to the SW; picture to the right looking to the SE). e) Faults are slip surfaces with no mineral precipitation (picture is a cross section, looking to the E). Arrows on the stereoplots indicate the sense of movement of the hanging wall block. All stereograms are lower-hemisphere equal-area projections.

Hydrothermal breccias in the ALFS outcrop, concentrated in the hanging wall, display width on the centimetric scale and along dip continuity >5m. These elements show a preferred WNW-striking, high angle dipping to the S attitude.

b) Fault-localized hydrothermal breccia (LOFS n=0, ALFS n=56)

These composed tabular discontinuities are made of two different bands (Figure 3-2b): (1) one or more hydrothermal breccias that are contained in (2) a fault breccia. The hydrothermal breccia band is composed of a two populations of subangular clast, interpreted to be from the host rock and previously precipitated hydrothermal material, and a fine-grained zeolitic matrix. The fault breccia band (cut by the hydrothermal breccia band), has foliated cataclastic fabric with S-C internal structure, consistent with reverse movement.

Fault-localized hydrothermal breccias only occur in the ALFS exposure, and are concentrated in the hanging wall block. These structural elements exhibit widths on the cm-scale, with along dip continuity >5m. The boundaries of the breccias strike NW, with high angle dips preferentially to the SW. Some of these structures exhibit evidence of sinistral-reverse shear, as inferred from the obliquity of the foliation and from measured striae with rakes <20° from the SW. Fault-localized hydrothermal breccias in this outcrop are locally cut and are cut by NW-striking, gently dipping faults with reverse centimetric separation (Zone I in Figure 3-1).

c) Vein (LOFS n=11, ALFS n=3)

These tabular discontinuities have hydrothermal infill, with no evidence of internal shear (Figure 3-2c). Veins are filled with equant milimetric crystals, without any preferred orientation on observation under naked eye.

In the LOFS exposure, veins occur in the hanging wall and the footwall blocks, and locally occur as banded aggregates. Vein widths vary from mm-to-cm scale, with along dip continuity >5m. Most of the veins are N50-60°E/subvertical structures. In the ALFS outcrop, veins only occur in the footwall, and presented cm-to-mm widths with continuity along dip between 0.5-5 m. NW to NNW strikes with high angle dips are dominant.

d) Fault-vein (LOFS n=5, ALFS n=2)

These tabular discontinuities show evidence of shear and growth of hydrothermal minerals (Figure 3-2d).

In the LOFS exposure, such elements are exclusively found in the hanging wall. The fault-veins in this outcrop have widths on the mm-scale, and persist >0.5 m along dip. The kinematics of opening is recorded by the presence of quartz or calcite mineral fibers. Two families of vein-faults were distinguished: dextral-reverse N65-90°E/80°S., and dextral-normal N40-45°/80°N, both families with rakes 15-20° from the E. Cross-cutting relationships between them could not be appreciated. In the ALFS exposure, fault-veins are present in foot and hanging wall. The vein-faults in this outcrop have widths on the mm-scale, and persist about 0.5 m along dip. They are preferentially sinistral N5-45°W/subvertical surfaces with rakes <10° from the S and the E.

e) Fault (LOFS n=5, ALFS n=2)

These tabular discontinuities shows evidence for shear (i.e. striae), but no precipitation of hydrothermal material (Figure 3-2e).

In the LOFS exposure, faults occur in both the footwall and the hanging wall blocks. These slip surfaces are exposed in patches of several tens of square centimeters, and have a preferred NE-striking/subvertical attitude. The rakes are <35° from the NE, indicating dextral-reverse movement principally recorded in steps.

In the ALFS exposure, faults occur in the hanging wall block, and have widths *ca.* 1-2 cm and along-dip continuity >1.5 m. The faults in this outcrop have preferred N40-50°W/25-30°S attitude, and cut and are cut by fault-localized hydrothermal breccias, which exhibiting reverse separation on the cm-scale (Zone I in Figure 3-1). Rakes could not be determined with the meso-structural analysis.

3.3 Mineral identification using X-ray powder diffraction (XRD)

The previously described structural elements are dominated by zeolitic assemblages in both exposures (Figure 3-3). The prevalent zeolite is laumontite, whereas other zeolites such as yugawaralite, heulandite, natrolite, scolecite, stilbite, chabacite and wairakite also are present. Common hydrothermal minerals, such as quartz and calcite also occur (complete dataset in Appendix G).

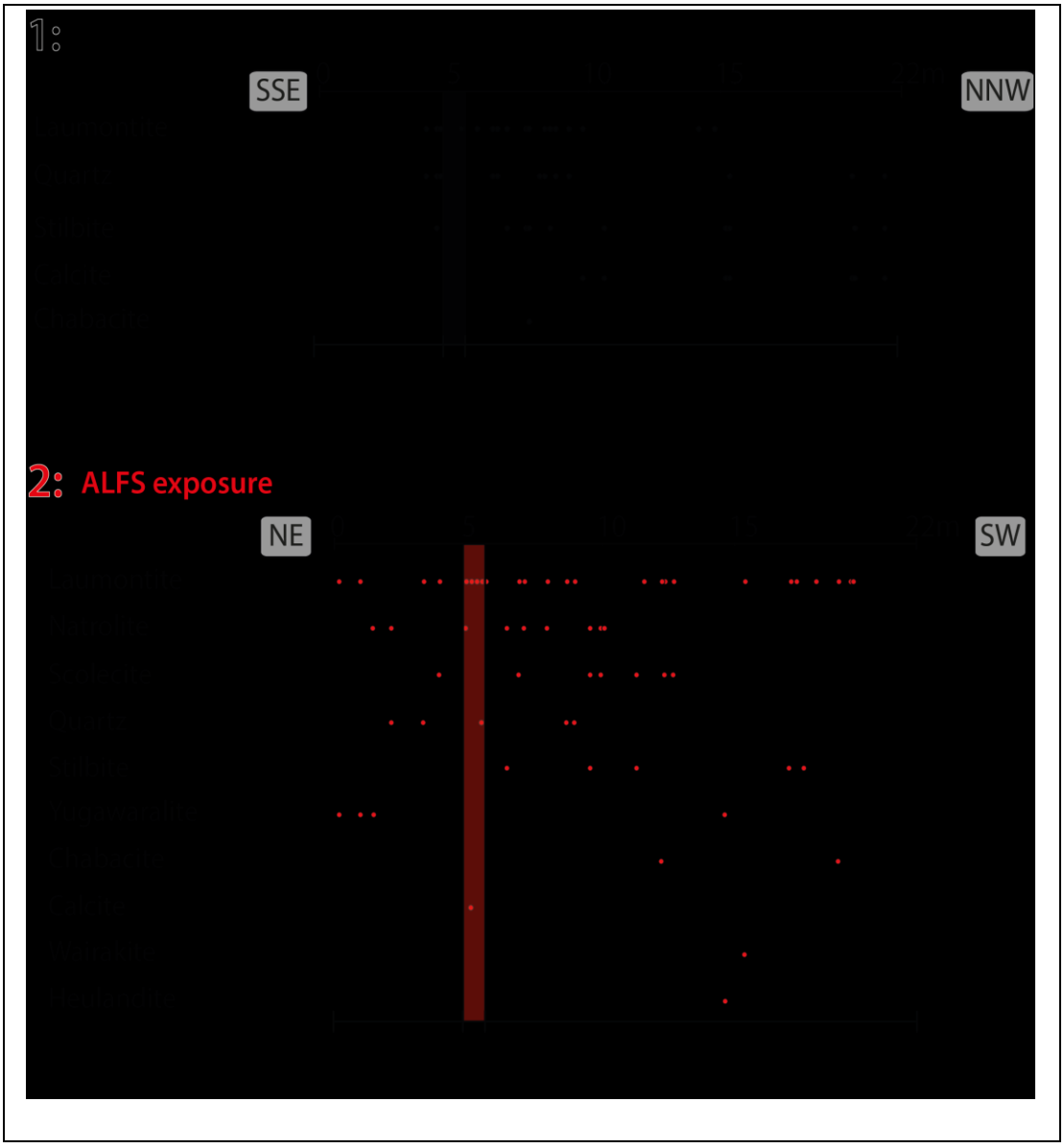

Figure 3-3. Spatial distribution of the syntectonic hydrothermal mineralogy present in the LOFS (black dots) and the ALFS (red dots) exposures.The cores are shaded, and the position of the damage zones is also indicated. See text for description.

The LOFS exposure has laumontite, quartz, stilbite and calcite as the prominent minerals, distributed in the core and the damage zone (Figure 3-3). In this exposure, the assemblage laumontite + stilbite is dominant along the fault zone. Minor quartz, calcite and chabacite were also locally found.

In the ALFS segment laumontite is the dominant hydrothermal product, and is uniformly distributed within the core and the damage zone (Figure 3-3). Natrolite and quartz were detected in the core as well as in both sides of the damage zone, close to the core. Scolecite, stilbite, chabacite and heulandite were only found in the hanging wall. Calcite was only detected in one sample. Pyroxene, feldspar and mica, coming from the andesitic host rock, are restricted to the hanging wall. In the ALFS outcrop no dominant mineral assemblages were detected, but in the damage zone two associations are locally present: laumontite + scolecite and laumontite + wairakite.

3.4 Petrographic and microstructural analysis

The LOFS exposure has an andesitic host rock. The andesite (Figure 3-4a) has porphyritic texture: phenocrysts are subhedral to euhedral crystals of: tabular K-feldspar (30%, 1-2 mm), tabular plagioclase (10%, 1 mm x 0.5 mm) and equant crystals of quartz (5%, 1 mm). The matrix is composed of: tabular albitised plagioclase (20%, 0.5 mm x 0.25 mm); a 20% a equant prismatic crystals of quartz (15%, <1 mm); equant prismatic orthopyroxene (5%, 0.1 mm; and a 20% of volcanic glass. Additionally, hydrothermal alteration occurs in amygdalae filled with (1) radiating subhedral to anhedral colorless zeolites (<0.5 mm), and (2) spherulitic chlorite (<0.5 mm) (Figure 3-4b). Locally, veins bearing colorless platy crystals of zeolite cut the previously described amygdalae. The core is composed of a microdioritic dyke (Figure 3-4c), and has traquitic texture, and it is composed of a

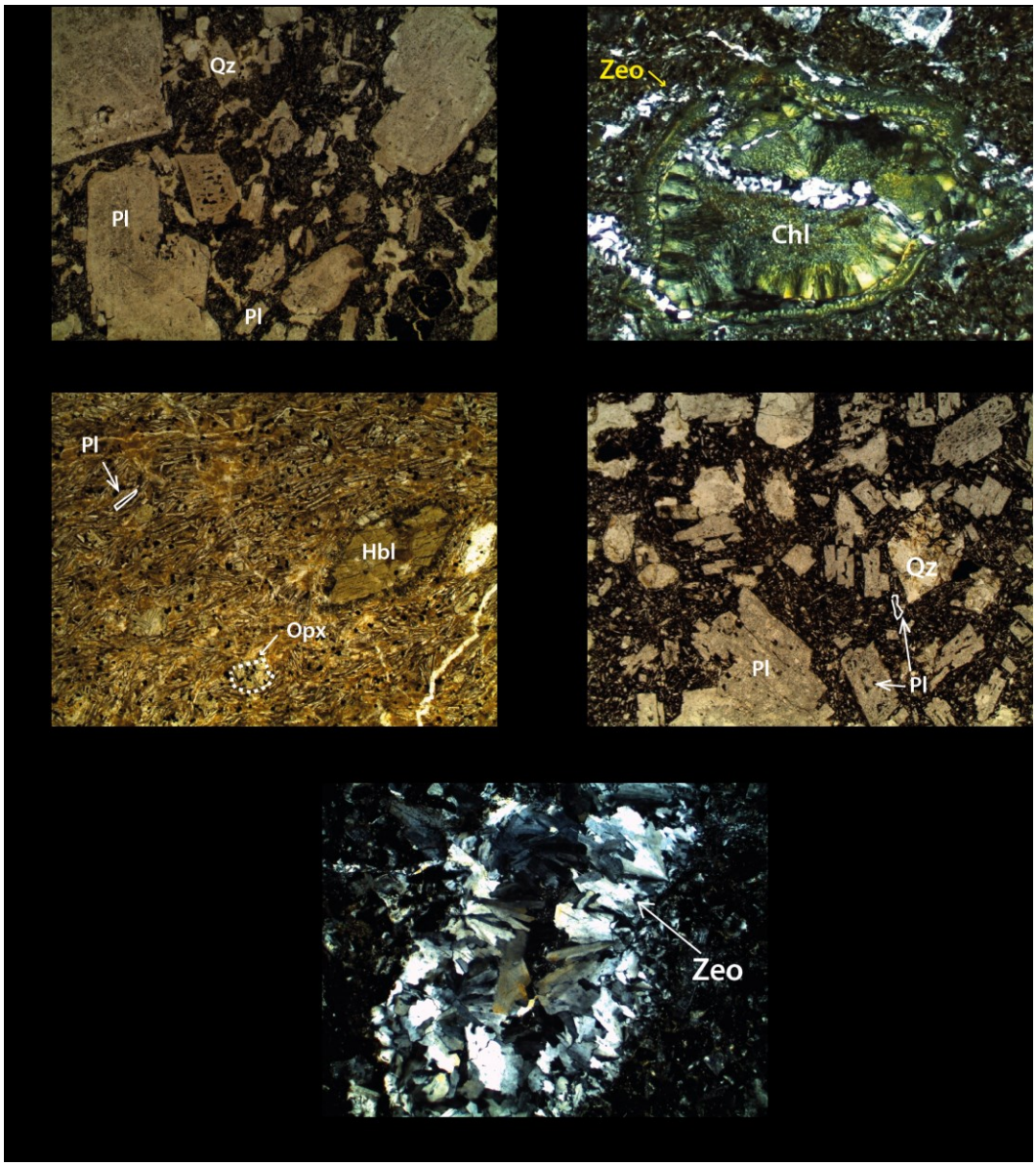

Figure 3-4. Photomicrographies of the host rocks and hydrothermal alteration in the studied faults of the LOFS (a-c) and the ALFS (d-e).Qz = quartz, Pl = plagioclase, Zeo= zeolite, Chl = chlorite, Opx = orthopyroxene. See text for description.

mosaic of subhedral to euhedral crystals of: a 60% of tabular plagioclase (0.5 mm x 0.1 mm) preferentially oriented; a 15% of equant prismatic crystals of hornblende (<2 mm); a 10% of equant prismatic crystals of orthopyroxene (0.1-1 mm); a 10% of a prismatic opaque mineral.

The ALFS exposure has an andesitic host rock (Figure 3-4d). This andesite has porphyritic-amygdaloidal texture. The phenocrysts are subhedral to euhedral crystals of: tabular albitised plagioclase (45%, 1.5 mm x 1 mm), equant crystals of quartz (5%, 0.8 mm), equant prismatic clyno and orthopyroxene (10%, 0.5 mm). The matrix is composed of: tabular plagioclase (20%, 0.2 mm x 0.05 mm) and a volcanic glass (20%). Hydrothermal alteration occurs in amygdalae filled with radiating subhedral to anhedral colorless zeolites (<0.5mm).

Microstructural analysis of the structural elements within the studied damage zones involved the description of 3 representative oriented samples, from which a detailed microstructural map of each one was made (1 fault-vein + 1 vein s of the LOFS exposure, and 1 hydrothermal breccia of the ALFS exposure).

a) Fault-vein of the LOFS exposure

The chosen representative NNE-striking sample of a fault-vein in the LOFS outcrop, found in the hanging wall block, has a width varying from 0.5 cm to 1 cm, with a diffuse and curved contact with the andesitic host rock (Figure 3-5a, b). The hydrothermal filling in this sample is composed of three microstructural families, distinguished by orientation (identified in green in Figure 3-5b): (1) a NE-striking en-échelon array of lenticular veins filled with platy-elongate and relatively large crystals of subhedral-euhedral laumontite (0.15mm-0.5mm)

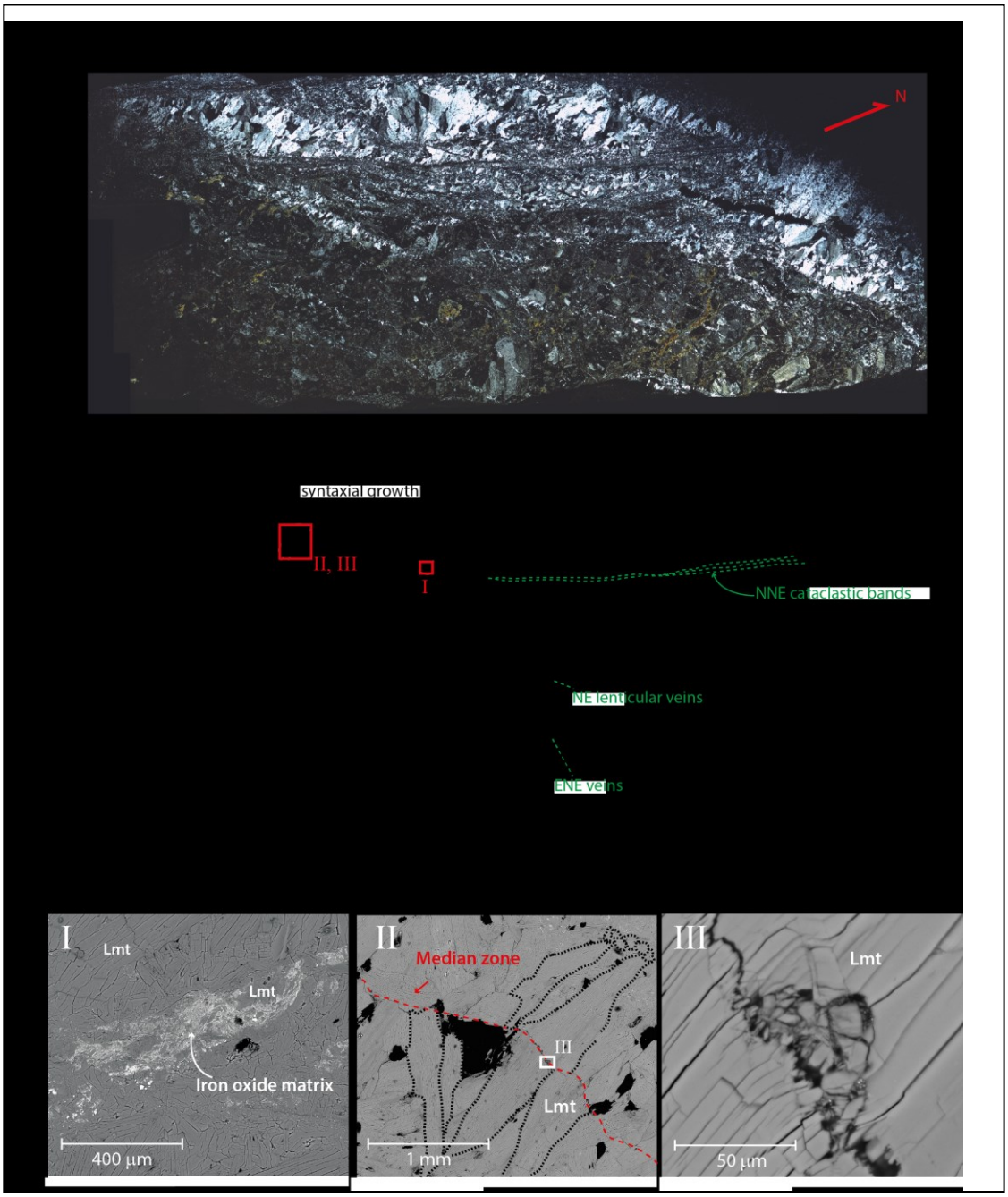

Figure 3-5. a) Photomosaic of the horizontal thin section LR7.75 (XPL). This sample presents a microcrystalline aggregate, uniform under observation with naked eye. b) Microstructural map of the sample. In red, selected areas to watch with the SEM, in green, the different structural families defined. Schematic crystals are drawn, along with black arrows, indicating growth direction of the crystals. c) Photomicrographies of selected areas in *b* (SEM-BSE). Zone I shows the texture of the cataclastic unit. Zone II shows syntaxial growth of laumontite crystals. Zone III shows the median zone between syntaxial laumontite crystals, exhibiting cataclastic fabric. Lmt = Laumontite.

(zone II in Figure 3-5b, c); (2) a cataclastic fine-grained mixture of subangular clasts of laumontite (0.05 mm-0.25 mm) embedded in a matrix of iron oxide (zone I in Figure 3-5b, c), that occurs between the NE-striking lenticular discontinuities or as NNE-striking bands, and (3) a ENE-striking family of discontinuities, filled with a mosaic of subhedral-platy laumontite (0.05-0.1mm).

The NE-striking lenticular veins occur in two NNE-striking bands (bands A and B in Figure 3-5b), distinguished by dominant size of single veins in the corresponding band (characteristic sizes: 10mm x 5mm in band A and 2.5mm x 1.5mm in band B). Individual lenticular veins have small equant crystals of laumontite: (1) concentrated in the two boundaries, with increasing length/width ratio towards a median zone (zone II Figure 3-5b, c); or (2) concentrated in one boundary increasing the length/width ratio towards the opposite boundary. In both cases, the long axis of the crystals is oriented perpendicular to the boundaries, which is consistent with syntaxial growth and at least one crack-seal episode (Ramsay, 1980; Wilson, 1994; Bons *et al.*, 2012).

On the other hand, the fine-grained cataclastic unit is composed of angular clasts (40%) with iron oxides as the matrix (60%) (Zone I in Figure 3-5b, c). According to the classification of Woodcock and Mort (2008), such population can be classified as a cataclasite.

Two key observations can be made: (i) the median zone in the NE-striking lenticular veins locally exhibits cataclastic texture (zone III in Figure 3-5c), and (ii) the cataclastic bands has laumontite clasts (zone I in Figure 3-5c). Both textures suggest that the NNE-striking en-échelon array of NE-lenticular veins served as a zone of weakness that localized dextral shear, as inferred from the obliquity of the lenticular veins with respect to the contact with the host rock. This story is in perfect agreement with proposed models on the formation of en-échelon veins (e.g. Olson and Pollard, 1991).

b) Vein of the LOFS exposure

The sample of the vein, within the footwall, and in contact with the fault core in the LOFS outcrop, is composed by three parallel EW-striking bands (bands A, B and C in Figure 3-6a, b), all filled with an aggregate of laumontite + stilbite and calcite. These bands are distinguished by the size of the crystals of the laumontite + stilbite aggregate: bands A and C are relatively coarse-grained (0.05-1.2 mm) (Zone I in Figure 3-6c), whereas band B is relatively fine-grained (≤0.05 mm) (Zone II in Figure 3-6c). Additionally, they are characterized by habit and size of the calcite crystals: band A has anhedral elongate crystals of calcite ranging from 0.5-6 mm in the direction of the long axis and 0.2-0.5 mm in the direction of the short axis; band B has hexagonal subhedral crystals of calcite ranging from 0.3-1.5 mm; and band C has platy-subhedral crystals of calcite with sizes between 1-10 mm.

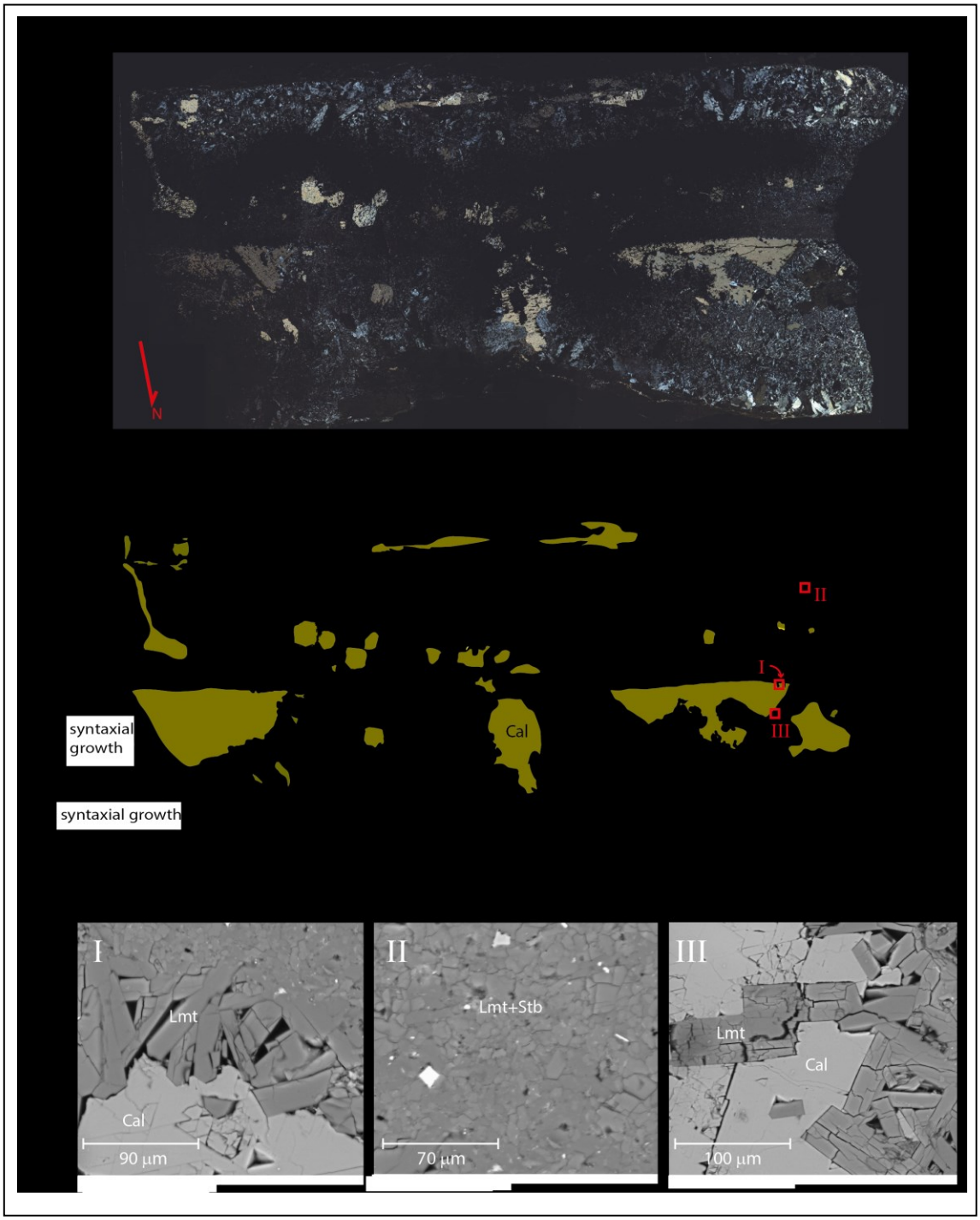

Figure 3-6. a) Photomosaic of the horizontal thin section TLR1507 (XPL). This sample corresponds to a banded vein, in contact with the fault core of the LOFS exposure. b) Microstructural map of the sample. In red, selected areas to watch with the SEM, Schematic crystal are drawn, along with black arrows, indicating growth direction of the crystals (black, laumontite crystals; yellow, calcite crystals). c) Photomicrographies of selected areas in *b* (SEM-BSE). Zone I shows syntaxial growth in the contact between bands B and C. Zone II shows characteristic texture of the fine-grained band B. Zone III intergrowth of calcite and laumontite, indicating co-precipitation. Lmt = Laumontite, Stb = Stilbite, Cal = Calcite.

Independently of the textures, the three bands record similar composition: bands A and B are composed of a 70% of the aggregate laumontite + stilbite and a 30% of calcite. B and C, in contact with the host rock, is filled with a 30% of prismatic subhedral-platy calcite, a 65% of an aggregate of subhedral laumontite + stilbite and a 5% of orthopyroxene, likely to come from the host rock.

Contact zones between bands A-B and B-C are sharp and nearly straight. Bands B and C have syntaxial growth of crystals: Band B has subhedral platy crystals of laumontite (0.1 mm-2 mm) growing perpendicular to the boundary in contact with band A; band C, on the other hand, has crystals of calcite and laumontite growing perpendicular to its boundaries towards the center (e.g. Zone I in Figure 3-6c). Additionally, bands A and C have intergrowth of calcite and laumontite (e.g. Zone III in Figure 3-6c), which indicates co-precipitation. Syntaxial growth and intergrowth textures indicate that each one of the three individual bands have formed in single, but not necessarily time-independent, crack-seal event (Ramsay, 1980).

c) Hydrothermal breccia of the ALFS exposure

The representative sample of a hydrothermal breccia in the ALFS exposure is composed of two NW-subvertical bands distinguished by mesoscopic color and internal textures (bands A and B in Figure 3-7a-c). Band A is white, has a width of 4 mm, and consists of a fine-grained mosaic of subhedral-platy laumontite

(≤0.15 mm). Band B is composed of a 40% of white sub-rounded equant clasts (1-3 mm) and a 60% of fine-grained grey matrix of subhedral-platy laumontite (≤0.15 mm). Clasts in band B are composed of smaller clasts of laumontite and quartz (zones II and III in Figure 3-7c, d), imbedded in a matrix of fine-grained grey laumontite (≤0.15 mm).

Clasts in band B very likely correspond to fragments of band A, as it becomes evident due to their similarity in mesoscopic color and mineralogy (Figure 3-7a).

Additionally, bands A and B are cut by mm-width, NW/subvertical veins with curved and diffuse boundaries, composed of relatively large crystals of subhedral-platy syntaxial laumontite (0.5 x 0.2 mm) (Figure 3-7c). Such NW-veins are locally cut by a subhorizontal attrition breccia (zone I Figure 3-7c, d) (Sibson, 1986), composed of an 80% of a mixture of angular clasts of laumontite and quartz (characteristic sizes 0.1 mm), imbedded in a 20% of a fine-grained matrix made of angular clasts of laumontite (≤0.01 mm).

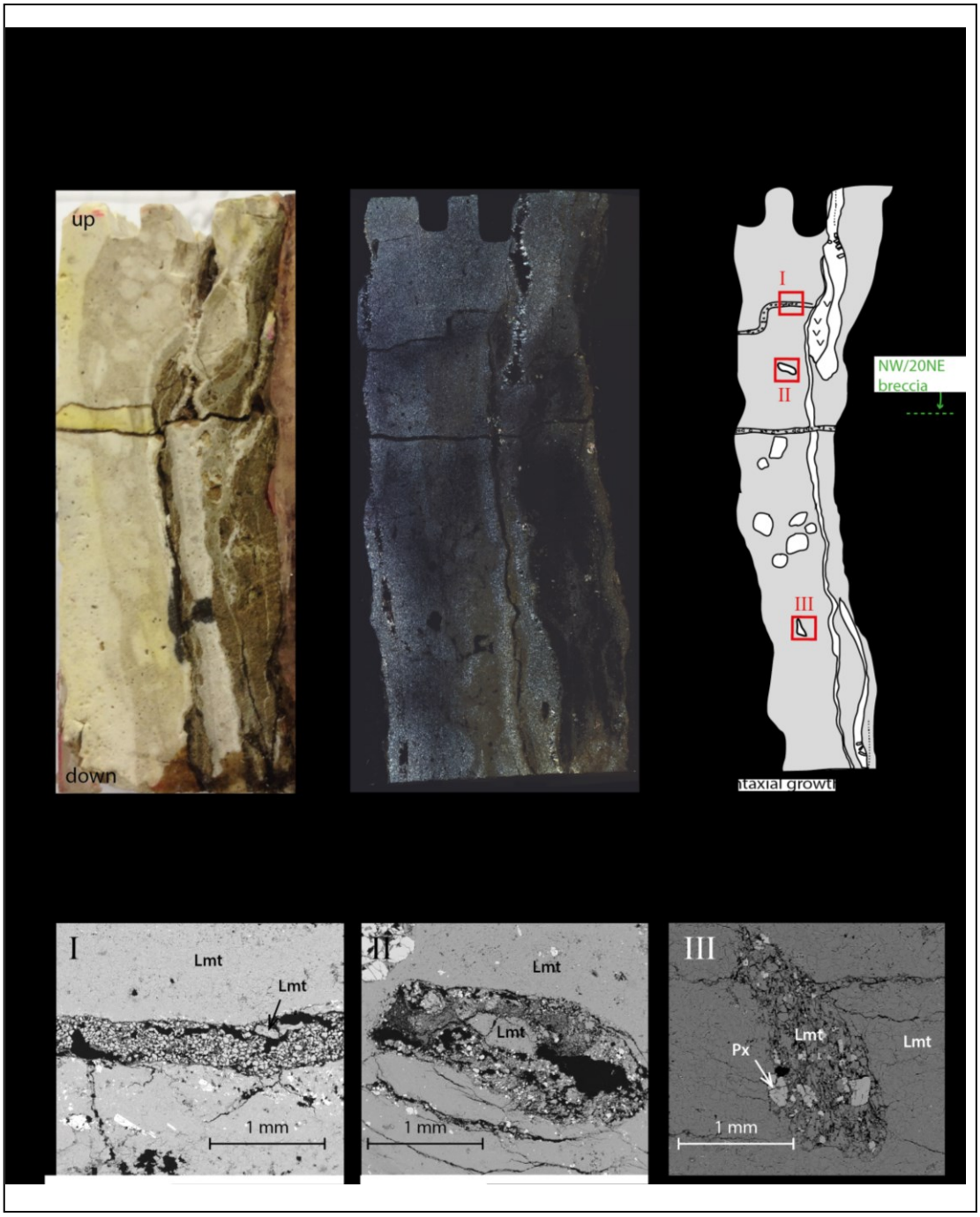

Figure 3-7. a) Photography of the vertical sample LAZI7.5E (hydrothermal breccia within the ALFS exposure). b) Photomosaic of the vertical thin LAZI7.5E (XPL). c) Microstructural map of the sample. In red, selected areas to watch with the SEM. Schematic laumontite crystals are drawn, along with black arrows, indicating growth direction of the crystals c) Photomicrographies of selected areas in *b* (SEM-BSE). Zone I shows a subhorizontal breccia. Zones II and III show characteristic texture of the clasts within band B. Lmt = Laumontite, Px = Pyroxene.

Additional to the microstructural observations, chemical composition analyses of zeolite-bearing structural elements were obtained from SEM-EDX, and are shown in Table 3-2.

Table 3-2. Zeolite SEM-EDX analyses in the LOFS and ALFS exposures. Analyses 1-9 correspond to heulandite, and 10-13 correspond to laumontite. *X_{Ca}=Ca/[Ca+Na]. ** values obtained assuming anhydrous basis.

	1	2	3	4	5	6	7	8	9	10	11	12	13
SiO_2	61.54	62.31	60.56	62.72	56.07	67.17	69.29	61.74	60.39	62.49	55.00	55.23	63.88
Al_2O_3	16.53	16.42	16.31	16.65	14.98	17.18	19.78	15.25	15.68	22.83	21.26	21.03	23.30
Fe_2O_3	0.00	0.00	0.00	0.00	0.00	1.16	0.76	0.00	0.00	0.00	0.00	0.00	0.77
MgO	0.00	0.00	0.00	0.00	0.00	0.56	0.00	0.00	0.00	0.00	0.00	0.00	0.00
CaO	7.64	8.02	7.86	7.92	6.28	9.28	10.98	8.06	7.74	12.16	11.63	10.79	12.26
Na_2O	0.63	0.88	0.86	0.44	0.62	0.00	0.66	0.42	0.44	0.57	0.00	0.00	0.70
K_2O	0.00	0.23	0.35	0.25	0.00	0.00	0.00	0.00	0.00	0.64	0.00	0.00	0.24
Total	86.35	87.86	85.94	87.99	77.95	95.34	101.47	85.46	84.25	98.67	87.88	87.05	101.14
Number of cations on basis of framework of**:													
	72O	72O	72O	72O	72O	72O	72O	72O	72O	48O	48O	48O	48O
Si	27.50	27.48	27.35	27.54	27.66	27.36	26.70	27.87	27.65	16.73	16.50	16.65	16.68
Al	8.71	8.54	8.68	8.62	8.71	8.24	8.99	8.11	8.46	7.20	7.51	7.47	7.17
Fe^{3+}	0.00	0.00	0.00	0.00	0.00	0.35	0.22	0.00	0.00	0.00	0.00	0.00	0.15
Mg	0.00	0.00	0.00	0.00	0.00	0.34	0.00	0.00	0.00	0.00	0.00	0.00	0.00
Ca	3.66	3.79	3.80	3.73	3.32	4.05	4.54	3.90	3.80	3.49	3.74	3.48	3.43
Na	0.55	0.75	0.76	0.38	0.59	0.00	0.49	0.37	0.39	0.29	0.00	0.00	0.35
K	0.00	0.13	0.20	0.14	0.00	0.00	0.00	0.00	0.00	0.22	0.00	0.00	0.08
Total	40.42	40.69	40.79	40.41	40.28	40.34	40.94	40.25	40.31	27.93	27.75	27.61	27.87
Si/Al	3.16	3.22	3.15	3.20	3.17	3.32	2.97	3.44	3.27	2.32	2.20	2.23	2.33
%E	10.72	0.94	1.32	8.06	20.42	-2.08	-3.76	-0.60	5.97	-3.81	0.55	7.22	0.38
X_{Ca}*	0.87	0.83	0.83	0.91	0.85	1.00	0.90	0.91	0.91	0.92	1.00	1.00	0.91

As a way to discriminate chemically distinctive zeolites, a Ca/[Ca+Na] *vs*. Si/Al diagram can be constructed (Figure 3-8). Obtained values are plotted in blue dots, and referential values for identified zeolites are in yellow dots. At least two zeolite families are present: i) a low Si/Al, Ca-rich family consistent with the occurrence of

laumontite (left in Figure 3-8); and ii) a high Si/Al, Ca and Ca(-Na) rich family, consistent with the presence of Ca-heulandite and Ca(-Na)-heulandite (Nesse, 2000).

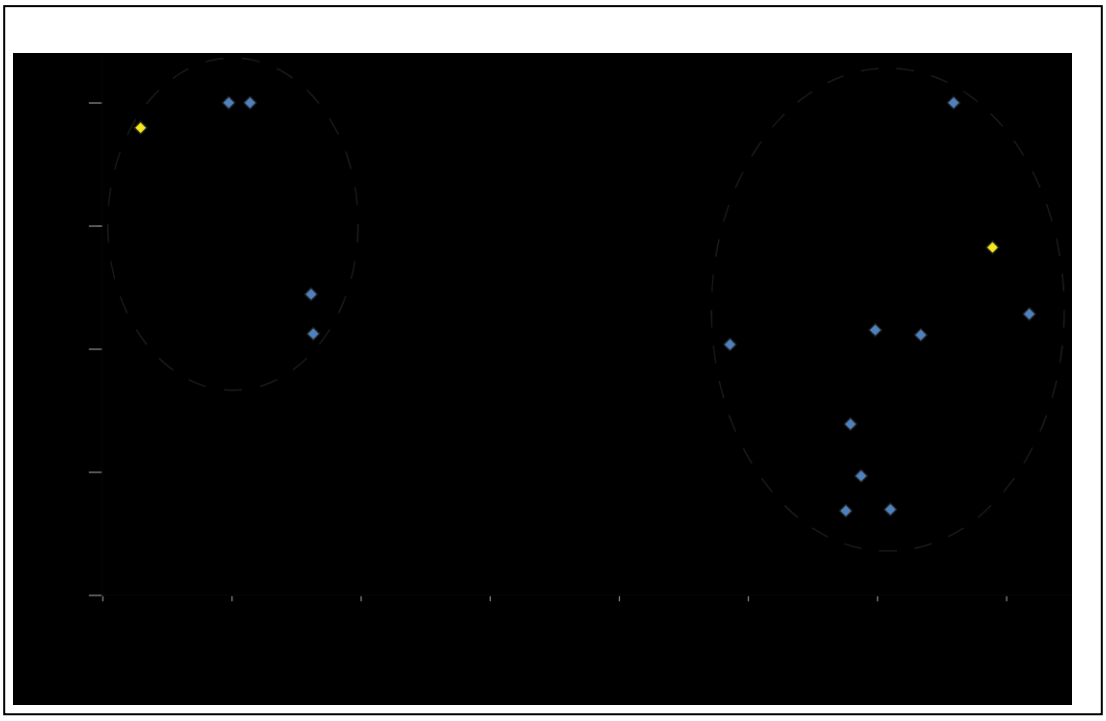

Figure 3-8. Proportion of Ca/[Ca+Na] *vs*. Si/Al. Values of blue dots correspond to those shown in Table 3-2. Blue dots represent obtained values. Yellow dots were obtained from analyses reported in Nesse (2000) in laumontite and heulandite-Ca and Ca(-Na).

3.5 2D electrical survey

The inversion of the 2D electrical survey along the profiles in the LOFS and ALFS exposures resulted in a model with resistivities that range between 1-3950 ohm-m and 1-6450 ohm-m respectively, and percentages of error summarized in Table 3-3.

Table 3-3. Percentages of error in inverted resistivity models.

Percentages of error in inverted models (%)		Resistivity profile in plan view		Resistivity profile in cross-sectional view	
LOFS exposure	Schlumberger	Line 1	6.2	Line 1	3.6
		Line 2	6.1	Line 2	5.2
	Dipole-dipole	Line 1	18.9	Line 1	16
		Line 2	16.2	Line 2	14.9
ALFS exposure	Schlumberger	Line 1	20.7	Line 1	1.75
		Line 2	30.3	Line 2	37
	Dipole-dipole	Line 1	29.4	Line 1	5
		Line 2	30.6	Line 2	30

As shown in Figure 3-9 and Figure 3-11, relative resistive values (red), relative conductive values (blue) and intermediate combinations can be found. In both resistivity profiles in plan and cross-sectional view, the shapes of the electrical anomalies of the Schlumberger and the Dipole-dipole geometries do not show considerable differences between each other. Instead, the greatest differences in the shape of the resistivity anomalies were found between the plan and cross-section profiles, regardless of the configuration used.

The profiles in plan view show 4 distinctive areas, in each outcrop and electrode configuration (domains 1-4 in Figure 3-9a-d), whose statistical distribution is summarized in Figure 3-10. Domain 1 corresponds to the volume of rock more exposed to weathering; domain 2 is the fault core; domain 3 is the damage zone within the hanging wall block; and finally, domain 4 represents the damage zone within the footwall block.

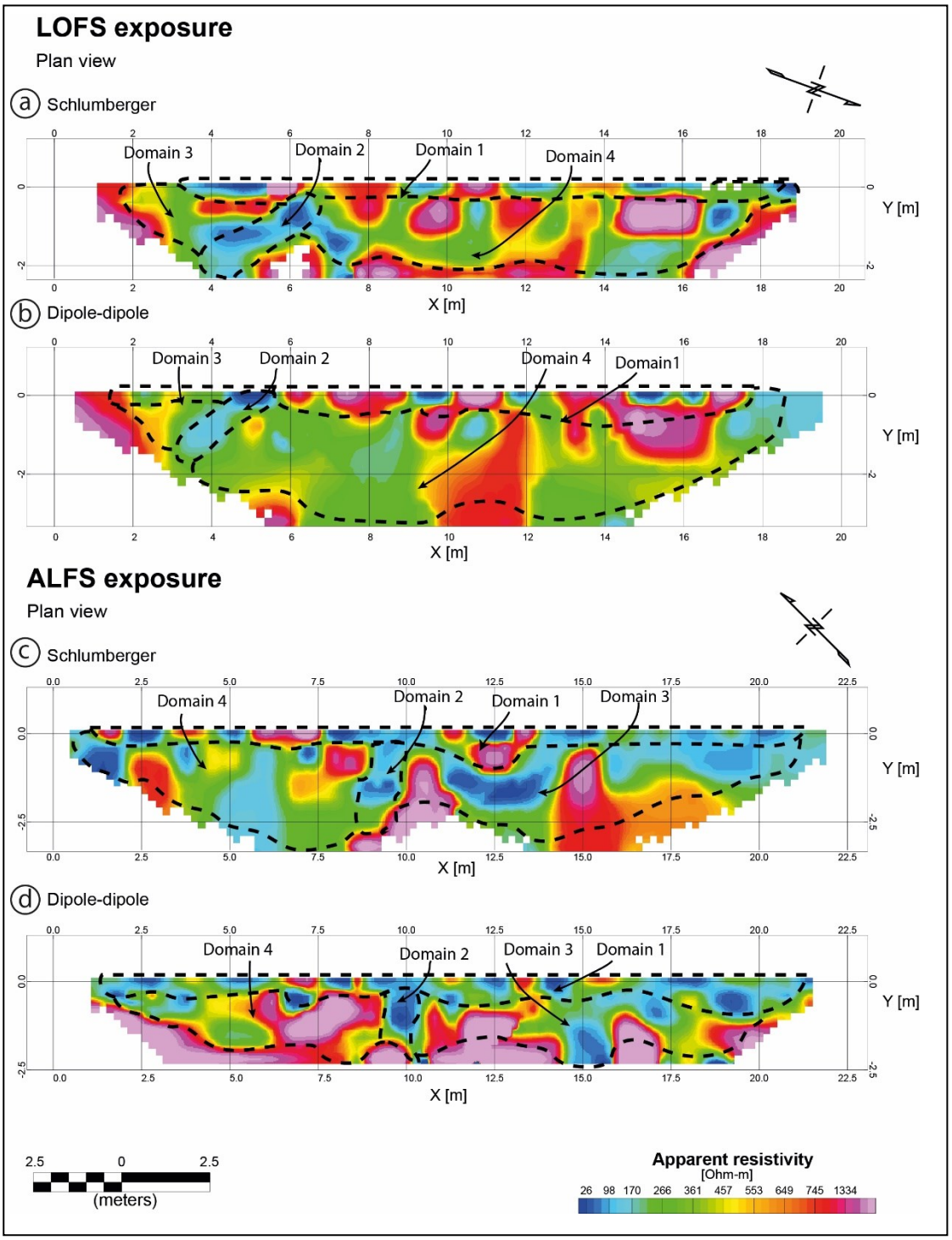

Figure 3-9. Inversion result along the profiles resulting from electrodes installed directly in the wall of rock. a) LOFS exposure, Schlumberger configuration. b) LOFS exposure, Dipole-dipole configuration. c) ALFS exposure, Schlumberger configuration. d) ALFS exposure, Dipole-dipole configuration. Domain *i* denotes the i-th electrical domain. See text for detailed description.

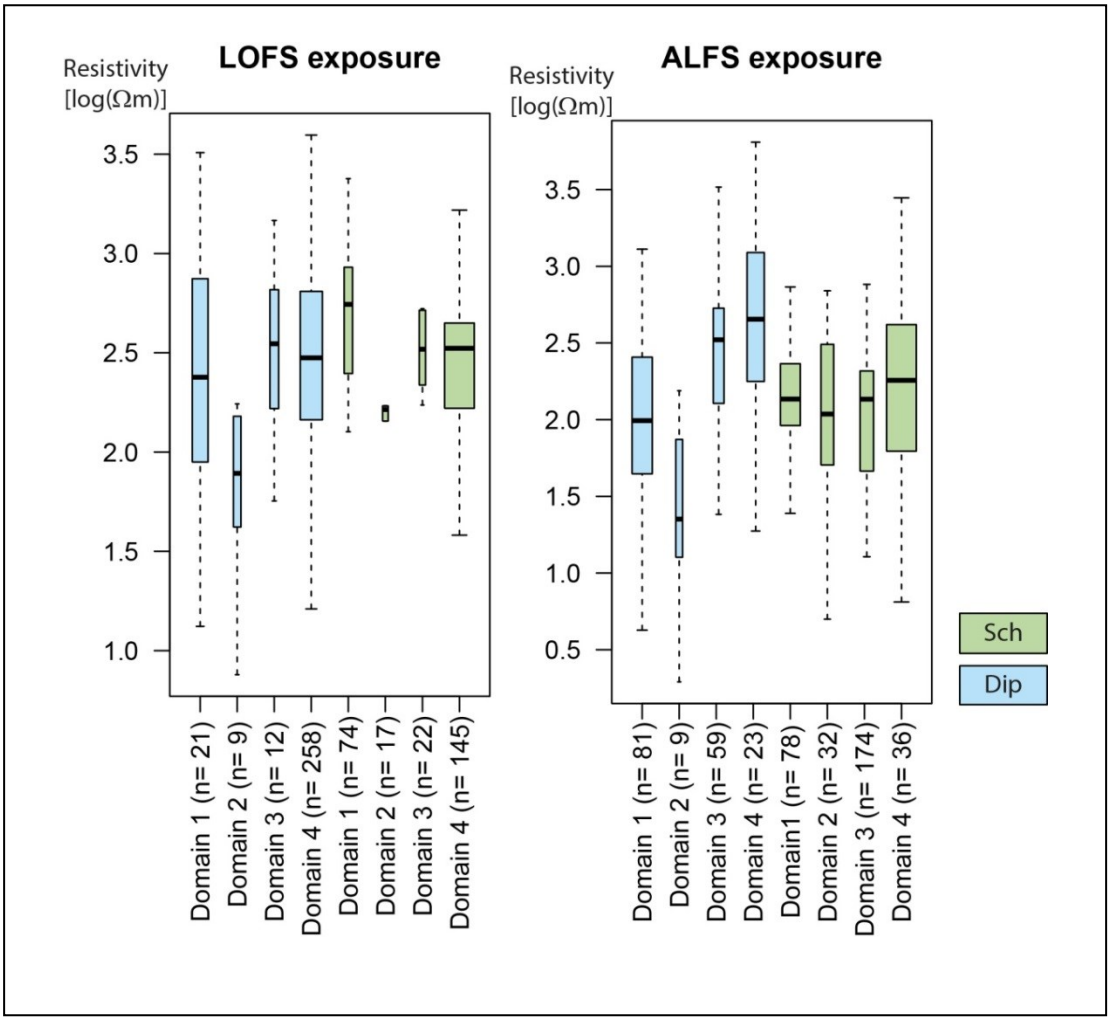

Figure 3-10. Boxplots resulting from the inversion of the plan view profiles in the LOFS and the ALFS exposures. Resistivity values are presented by domain and configuration of electrodes, in logarithmic scale. Green boxes = Schlumberger configuration, blue boxes = dipole-dipole configuration. Width of the boxes represents relative statistical weight determined by the number of observations (n).

In the LOFS exposure (Figure 3-9a, b), domain 1 corresponds to the shallowest 0.5m, and exhibits a wide range of resistivity values (9-2380 ohm-m). Domain 2, located in the southern part of the section, is an evident WNW-striking localized relative conductor (10-175 m) of *ca.* 0.7m width. Domains 3 and 4 display ample resistivity values (20-1500 ohm and 1-3950 ohm-m respectively) and extend about 6m and 10m across the profile correspondingly.

In the ALFS segment (Figure 3-9c, d), domain 1 corresponds to the shallowest 0.4m, and exhibits a wide range of resistivity values (4-4000 ohm-m). Domain 2, located in the central part of the section, is an evident NW-striking localized relative conductor (1-200 ohm-m) of *ca.* 0.5m width. Domains 3 and 4 display a wide range of resistivity values (1-6450 ohm-m and 1-2790 ohm-m respectively) and extend about 14 m and 7 m across the profile.

On the other hand, the cross-sectional profiles show horizontal electrical anomalies (Figure 3-11a-d), with values of resistivity ranging between 4-9675 ohm-m. In both outcrops and in each electrode configuration, two domains were distinguished: domain 1, which corresponds to a relative resistive and shallow volume; and domain 2, which is a horizontal relative conductor and deeper volume.

In the LOFS exposure (Figure 3-11a, b), domain 1 corresponds to the shallowest, resistive 0.5-0.8 m, exhibiting a wide range of resistivity values (7-8070 ohm-m, >50% of values above 660 ohm-m). Domain 2 is a relative conductor with ample resistivity values (50-4450 ohm-m, >75% of values below 610 ohm-m).

In the ALFS exposure (Figure 3-11c, d), domain 1 corresponds to the shallowest 0.7-0.8m, and exhibits a wide range of resistivity values (4-7730 ohm-m, >75% of values below 750 ohm-m). Domain 2 is a relative conductor with ample resistivity values (7-9673 ohm-m, >75% of values below 460 ohm-m).

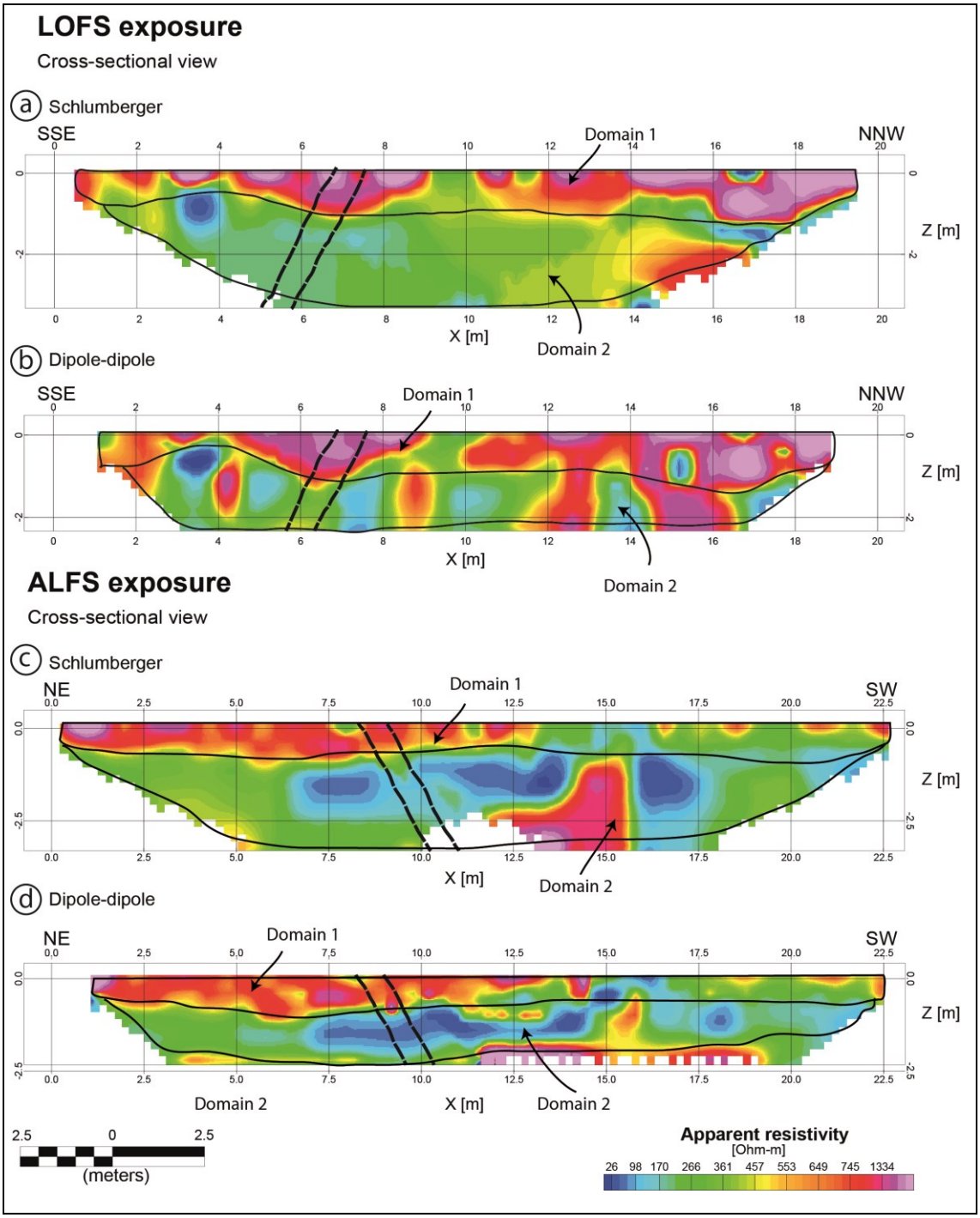

Figure 3-11. Inversion result along the profiles resulting from electrodes in the ground. a) LOFS exposure, Schlumberger configuration. b) LOFS exposure, Dipole-dipole configuration. c) ALFS exposure, Schlumberger configuration. d) ALFS exposure, Dipole-dipole configuration. Black dashed lines within the profiles enclose the fault core, and indicate the beginning of the damage zone. Domain *i* denotes the i-th electrical domain. See text for detailed description.

4. DISCUSSION

4.1 Brecciated textures and rupture cycle

The dominant structural elements within the damage zone of the LOFS exposure are hydrothermal breccias (Figure 3-2a), whereas in the ALFS outcrop are fault-localized hydrothermal breccias Figure 3-2b). There are different genetic classifications of fault breccias, of which probably the most influential are Sibson's (1986) and Jébrak's (1997) schemes. Here I used the classification of Jébrak (1997), based on the morphology of the fragments and the particle size distribution as a function of the energy input. Two main types of breccias were distinguished: fluid-assisted breccias and tectonic comminution breccias. Jébrak (1997) states that fluid-assisted breccias are formed by fluctuations in pore fluid pressures, and have high dilation ratio α (defined as the proportion of abundance of matrix with respect to the clasts). This author indicates that when they are formed with a relatively low amount of energy (directly related to fluid flow, volume and pressures), fluid-assisted breccias have angular clasts with a good selection in a jigsaw-like texture. However, I propose that when greater energy is supplied to the system (e.g. constant fluid flow, overpressured fluids and/or large volumes of fluids), fragments are likely to develop more rounded shape, bad selection and jigsaw texture may be obliterated. As it will be discussed in Section 4.4 this last scenario seems to be the case in the analyzed exposures. On the other hand, tectonic comminution breccias are formed by the progressive shear along slip surfaces, and therefore have low α, angular clasts and bad selection. For the previous reasons, the classification of the breccias was mainly based on the nature of

the matrix, and dilation of the structure (exotic hydrothermal matrix and high α indicating fluid-assisted brecciation, and autogenous matrix with low α indicating tectonic comminution brecciation).

Under this scheme, hydrothermal breccias in the LOFS outcrop can be classified as fluid-assisted breccias, formed with an important component of extensional failure (α=50-60%). On the other hand, fault-localized hydrothermal breccias in the ALFS exposure are composed of: (1) what is here interpreted as a tectonic comminution breccia (cataclastic fabric in Figure 3-2b), and (2) a fluid-assisted breccia (hydrothermal breccia in Figure 3-2b), cutting the tectonic comminution breccia (α=5%). In summary, the LOFS splay fault registers a dominance of failure in extension (±shear) and the ALFS segment records two modes of brittle failure: (1) extension (±shear), and (2) reverse shear (±extension).

Additionally, three important observations can be made: (1) in the LOFS exposure, at least three extensional (± shear) crack-seal episodes are recorded in the banded vein at the boundary of the core (Figure 3-6); (2) In the ALFS exposure, field and microstructural evidence demonstrate that the two proposed modes of failure are superimposed (e.g. Figure 3-1e, f and Figure 3-7); and (3) clasts in the fault-localized hydrothermal breccias have, in turn, a brecciated texture (Zones II and III in Figure 3-7). These observations suggest that the observed textures are the result of cyclical rupturing (Figure 4-1)

Figure 4-1. Proposed rupture cycle for the LOFS and the ALFS exposures, based on the inferred modes of failure of the dominant structural elements within the damage zones. See text for discussion.

In the LOFS exposure, extensional (±shear) failure occurs in discrete episodes, reactivating previously formed extensional discontinuities (Figure 4-1a). In the ALFS segment, shear (±extension) and extension (±shear) failure episodes alternate: shear episodes localize strain in weakness zones, where a cataclastic fabric is generated (Figure 4-1b-i); extensional episodes produce a transient dilation at such inherited structural sites, producing a brecciation of the wallrock, circulation of fluids and hydrothermal cementation (Figure 4-1b-ii). Subsequent shear episodes may activate the previous discontinuities and/or produce second-order shear structures (Figure 4-1b-iii).

4.2 Fault zone kinematics, style of fracture-controlled permeability and outcrop-scale tectonic regimes

Structural meshes in the damage zones of the LOFS and the ALFS exposures are dominated by subvertical structural elements concentrated in the hanging wall (Figure 3-1a-d), which seem to be primary associated with transtensional faulting (Sibson, 2000). However, only the ALFS exposure preserves clear architectural features consistent with a transtensional faulting regime (foliated gouge in Figure 3-1c, d). Both the inferred kinematics of the fault zones, and the style of fracture-controlled permeability within the damage zone, can be compared with stress fields obtained in the same localities in the work done by Pérez-Flores *et al.* (2015). They obtained the directions of the stress tensor from the multi-inverse method (Yamaji, 2000), which is able to discriminate stress fields from an heterogeneous distribution of fault slip data.

In the case of the LOFS exposure they obtained a strike-slip stress tensor given by: σ_1 = N14W/03N, σ_3 = N78E/32E, which is consistent with normal-sinistral faulting in the N83W/65SW core. Likewise, the style of fracture-controlled permeability in most of the structural elements within the damage zone is in agreement with this stress field (Figure 4-2a): the dominant extensional (±shear) discontinuities (hydrothermal breccias, veins, and vein-faults) mostly occur at 0-30° from the maximum principal stress σ_1. In addition, the least abundant shear fractures (faults) occur at angles that vary between 20-80° from σ_1, and also are compatible with these stress conditions.

On the other hand, in the ALFS outcrop, Pérez-Flores *et al.* (2015) obtained two stress tensors: (1) a strike-slip solution with σ_1 = N110E/19SE and σ_3 = N11E/11N; and (2) a transtensional solution with σ_1 = N133W/45SW and σ_3 = N4W/32N. In this case, the genesis of the dominant structural elements within the damage zone (fault-localized hydrothermal breccias) is compatible with the strike-slip stress field (Regime 1 in Figure 4-2b): shear discontinuities (cataclastic bands within fault-localized hydrothermal breccias) mostly occur at 5° from the maximum principal stress σ_1. However, only some of the extensional discontinuities (hydrothermal breccias and veins) respond to this stress field. In particular, hydrothermal breccias are concentrated at 0-5° from σ_1 and their occurrence is compatible with the presented stress field. Nevertheless, veins are at 70° from σ_1.

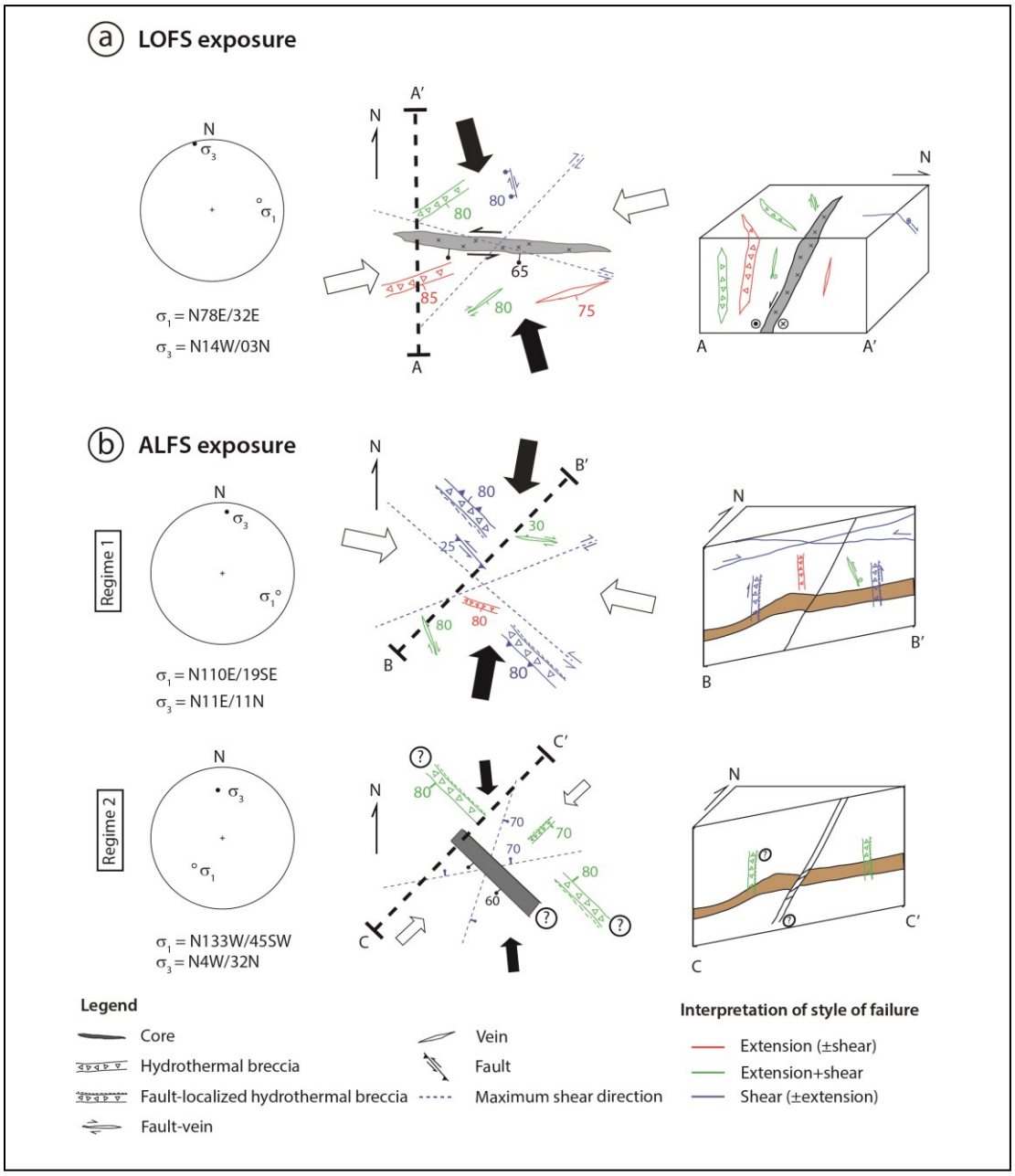

Figure 4-2. a) Cartoon illustrating the core and structural elements within the damage zone of the LOFS outcrop. Maximum shear direction θ_{MAX} was drawn considering a typical coefficient of friction μ=0.75 in an intact rock, i.e. θ_{MAX} =35, measured from σ_1 b) Cartoons illustrating the compatible structural elements in Regime 1, and reactivation (Regime 2) of core and structural elements within the damage zone of the ALFS outcrop. Maximum shear direction was obtained as explained as in (*a*). Principal styles of deformation inferred from meso- and microscopic textures are color-coded: red indicates failure in extension; green, failure in hybrid extension+shear; and blue, shear failure. Black and white arrows indicate the direction of the least principal stress σ_3 and the greatest principal stress σ_1, correspondingly.

Similarly, hybrid extensional+shear fractures (vein-faults) occur at 50° from σ_1. Consequently, the least abundant veins and vein-faults are not compatible with the near-Andersonian strike-slip regime. On the other hand, the second non-Andersonian transtensional tensor documents a rotation between σ_1 and σ_2, σ_1 becoming more vertical. In this manner, transtensional faulting in the ALFS core, and extensional (±shear) reactivation of misoriented fault-localized hydrothermal breccias could be associated to this regime (Regime 2 in Figure 4-2b), only possible under particular fluid overpressure conditions discussed later (Section 4.4).

In sum, the previous observations and the rupture cycle proposed before, jointly suggest that: (1) the studied splay fault of the LOFS cyclically fails in transtension under a near-Andersonian strike-slip regime (i.e. $\sigma_2 \approx \sigma_V$) and (2) the analyzed segment of the ALFS records switches in the outcrop-scale stress regimes, changing between failure in transpression under a near-Andersonian strike-slip regime ($\sigma_2 \approx \sigma_V$) and failure in transtension under a non-Andersonian transtensional regime (i.e. $\sigma_x \neq \sigma_V$, for x=1,2,3).

4.3 Zeolite-bearing structures and temperature-depth conditions

Zeolite-bearing structures have been widely used to establish the temperature stability in active geothermal systems (e.g. Browne, 1978 and references therein). In general, the suggested temperatures are in fairly good agreement with experimental results (Liou *et al.*, 1987). However, pore fluid pressures in experimental environments do

not account for dynamic pressure effects, not necessarily neglectable in the case of shallow hydrothermal systems (Kristmannsdóttir and Tómasson, 1978), so these pore fluid pressures were not considered in the structural analysis.

The dominant minerals detected in the study areas are Ca and Ca(-Na) zeolites (Figure 3-3), usually found in geothermal systems as a result of the interaction of chloride hydrothermal fluids of near-neutral pH and volcanic rocks (Browne, 1993). Detected mineralogy indicates the dominance of laumontite, the best index mineral for zeolite facies metamorphism (Liou *et al.*, 1991), locally found in the following assemblages: (1) laumontite + stilbite, which indicates crystallization close to 110ºC (in the LOFS exposure); (2) laumontite + scolecite at 120ºC (in the ALFS exposure); and (3) laumontite + wairakite, at 210ºC (in the ALFS exposure). The stability temperature interval proposed for these associations is consistent with previous recorded zeolite temperature in active geothermal systems (Kristmannsdóttir and Tómasson, 1978) and also with experimental P-T conditions for Ca-zeolites in the presence of excess quartz and fluid (Liou *et al.*, 1991). Moreover, two invariant points have been proposed for the stable coexistence of (Liou *et al.,* 1991): i) stilbite, heulandite and laumontite at *ca*. 60 MPa and 140ºC; and ii) yugawaralite, wairakite and laumontite at *ca*. 50 MPa and 230°C (Figure 4-3). Under the assumption that phases were in equilibrium, structural conditions suggest a conjectural P-T trajectory as shown in Figure 4-3. In this path, the system increases its temperature and decreases fluid pressure, which is consistent with exhumation temporarily related to fault zone activity.

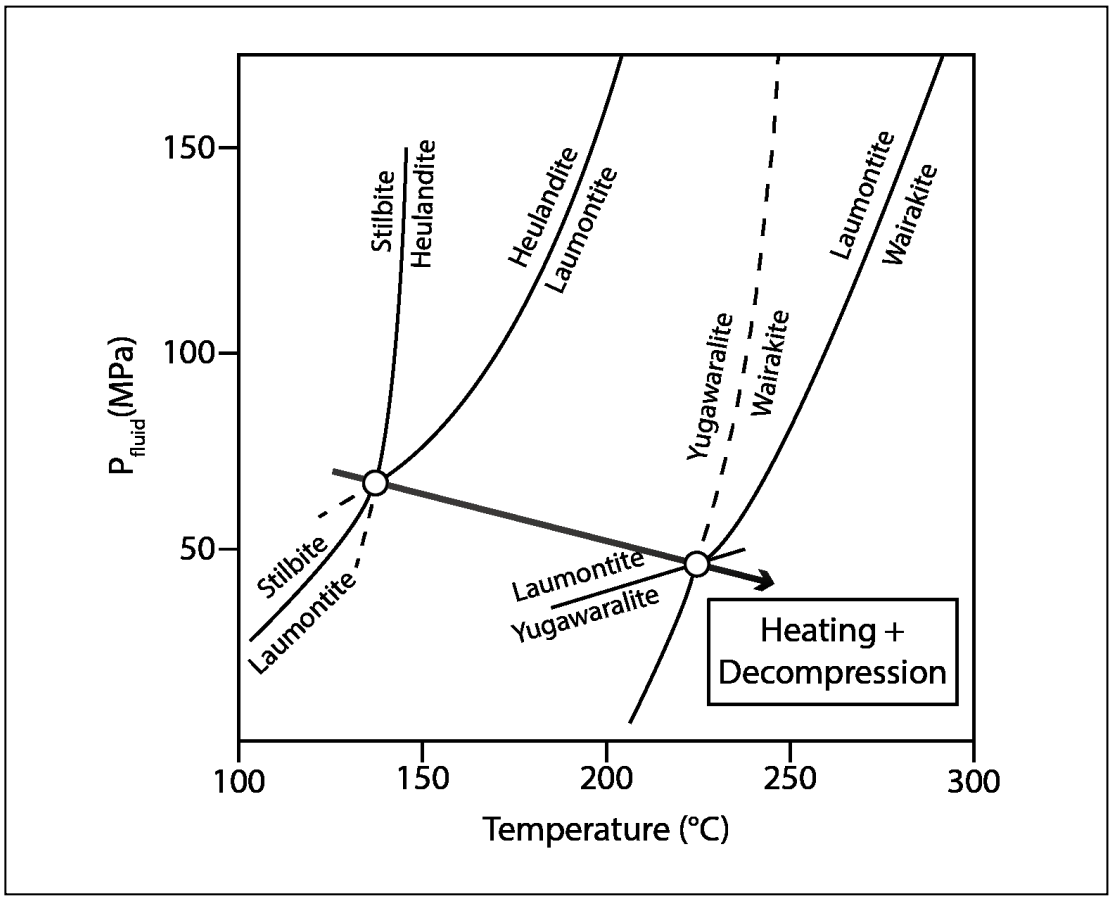

Figure 4-3. Experimental P-T conditions for the stable coexistence of: i) stilbite, heulandite and laumontite at *ca*. 60 MPa and 140ºC; and ii) yugawaralite, wairakite and laumontite at *ca*. 50 MPa and 230°C. Geological conditions suggest a heating and decompression of the systems, from the transition from the first to the second invariant point. Modified from Liou *et al.* (1991).

In addition, following experimental P-T determinations of Liou *et al*. (1991), transition from laumontite to wairakite throughout yugawaralite in the ALFS exposure could suggests high metamorphic gradient under a high P_{H2O}/P_{TOTAL} ratio.

The paleodepth of these exposures at the time of vein formation is unknown, but a good available proxy are documented geothermal gradients within the volcanic arc in the Andes (Aravena and Lahsen, 2012; Aravena *et al.*, 2016), which can be as high as *ca.* 200°C/km in high enthalpy environments. Since this kind of values are

anomalous in the Andes, two conservative and conjectural gradients were considered: 60°C/km and 100°C/km. Using the upper limit temperature of 210ºC (laumontite + wairakite), such gradients deliver conjectural depths between 2.1-3.5 km.

4.4 Failure envelope and conditions for brittle failure

Here I take a quantitative approach, modeling failure envelopes in the λ–σ space to study: (1) the origin of fracture-controlled, fault-related permeability and (2) the style of reactivation of inherited structural elements. The structures in the LOFS and ALFS exposures seem to have formed under their own unique, near-Andersonian strike-slip stress regime (Figure 4-2a, b). However, field evidence suggests that the ALFS exposure reactivates in extension (±shear) (Figure 4-1) in a non-Andersonian transtensional stress field (Regime 2 in Figure 4-2b).

Cox (2010) provided the theoretical framework necessary to construct λ–σ failure diagrams in structural arrays with Andersonian stress regimes in which the medium principal stress σ_2 lies on the fracture plane, considering two scenarios: (1) intact rock and (2) re-shear of cohesionless pre-existing fault. I modelled the near-Andersonian strike-slip regimes using Cox's scheme. To depict these graphs I used: (1) the depths inferred from the mineralogy at the time of vein formation (2.1 and 3.5 km depth); (2) a representative coefficient of internal friction μ=0.75 (considering that rocks at elevated temperatures often seal and regain cohesive strength on the timescales of rupture recurrence, following Cox, 2005); and (3) a tensile strength T=15 MPa and a

density of ρ=2450 kg/m^3 (expected for an andesite, following Rowland and Sibson, 2004). Cold hydrostat and lithostatic pore fluid factors are shown for reference. Typical overpressures in active geothermal areas are also depicted for reference (λ_V>20% above cold hydrostatic pressure, following Rowland and Simmons, 2012).

To model failure conditions in the non-Andersonian transtensional regime, I extended the analysis to a general case, considering the reactivation of previously existing discontinuities. Such a scenario implies that σ_2 is not necessarily contained on the plane of the inherited structure. For the previous reasons, this method allows to study extremely complex structural settings, incorporating the effect of any rotation of the principal stresses with respect to the inherited anisotropy. The mechanical fundament of this analysis is that the principal stress field can be projected on the plane of interest, which produces both a tangential and normal stress on the pre-existing surface (governing equations of the stress projection and failure envelope construction can be found in Appendix H). The generalized λ–σ diagrams were obtained projecting the principal stresses of Pérez-Flores *et al.*, (2015) on a representative fault-localized hydrothermal breccia (N45°W/80°SW). The depths and mechanical properties are the same as those of the Andersonian case.

In both cases, failure envelopes are color-coded to indicate the mode of failure: red lines indicate failure in extension; green lines, failure in extension + shear; and blue lines, failure in shear. The graphs illuminate about some important points in the

activation and permeability enhancement of the studied outcrops of the LOFS and the ALFS (Figure 4-4):

(1) In the LOFS exposure, field evidence demonstrates that the Andersonian strike-slip transtensional tensor preferentially generates extensional (±shear) structures. This style of deformation *is possible* under typical ranges of pore fluid pressures (cold hydrostatic and typical overpressure) and low depth (2.1 km) (point A in Figure 4-4). Nonetheless, between the same ranges of fluid pressures and greater depth (3.5 km), only shear failure is possible. This suggests that the proposed style of fracture-controlled permeability in the studied exposure of the LOFS is likely to develop at depths < 2.1 km.

Stress regime	λ–σ diagram	Textural evidence LOFS exposure	Textural evidence ALFS exposure
Andersonian strike-slip regime $\sigma_2 = \sigma_V$ = constant	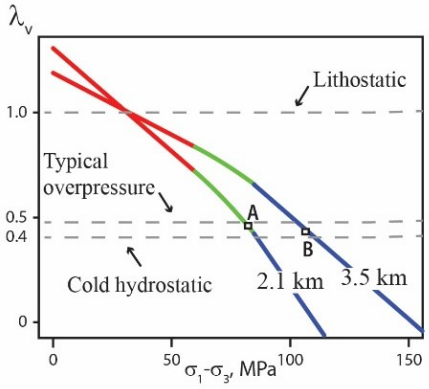	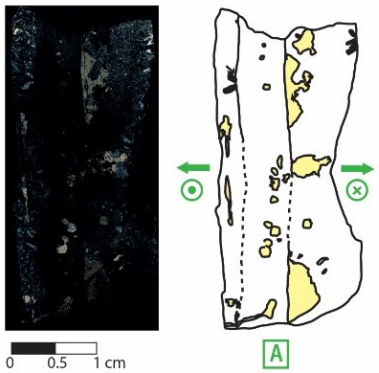	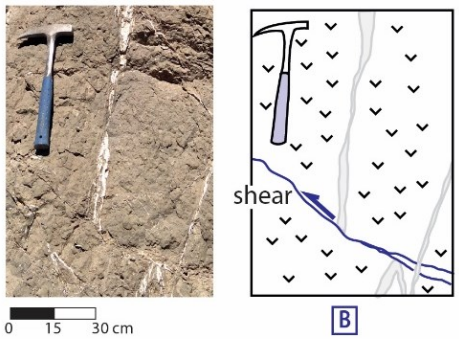
Non-Andersonian transtensional regime $\sigma_x \neq \sigma_V$, x=1,2,3	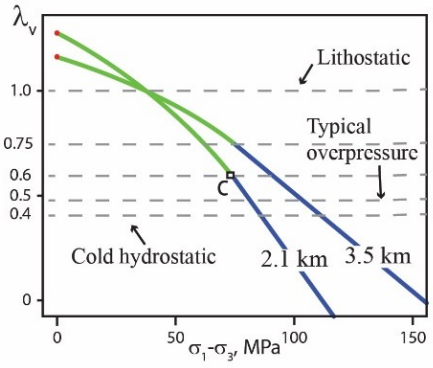		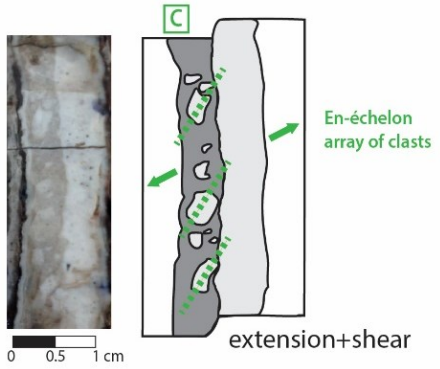

Figure 4-4. Failure envelopes in the λ–σ space (after Cox, 2010). This envelopes show the effect of varying the depth (obtained from the zeolitic assemblages) in the mode of brittle failure. Failure curves are color-coded: red = extension, green = extension + shear failure, blue = shear failure. Cold hydrostatic and lithostatic pore fluid factors are depicted, along with typical overpressures in active geothermal areas (Taupo Volcanic Zone) (Rowland and Simmons, 2012). See text for discussion.

(2) In the case of the ALFS exposure, field evidence demonstrates that phases of Andersonian strike-slip tectonics preferentially generate shear structures. Such a type of failure is possible under typical ranges of pore fluid pressures and depths varying between 2.1 - 3.5 km (e.g. point B in Figure 4-4). This reinforces the idea that the ALFS exposure was active under such depths. However, field evidence suggests that a switch to a non-Andersonian transtensional regime generates hybrid extensional (±shear) failure in the inherited structures of the damage zone (e.g. point C in Figure 4-4). This type of deformation *is not possible* under typical ranges of pore fluid pressures. In fact, it requires $\lambda_V \geq 0.6$ for z=2.1 km (λ_V >50% above cold hydrostatic pressure) and $\lambda_V \geq 0.75$ for z=3.5 km (λ_V >88% above cold hydrostatic pressure). When comparing the plots of both tectonic states of stress, it can be observed that a switch from an Andersonian strike-slip to a non-Andersonian transtensional regime involves increasing pore fluid pressures at a minimum percentage of 50% (z=2.1 km) and 15% (z=3.5 km) (Figure 4-4)

The proposed rupture model is consistent with geological observations regarding crustal seismic activity of Dempsey *et al.* (2014): extensional/hybrid reactivation of shear fractures has been observed to require elevated fluid pressures in zeolite-bearing normal faults, involving an initial stage of fluid ingress, then trapped and overpressured, leading to fluid-assisted rupture and mineral cementation (Dempsey *et al.*, 2014).

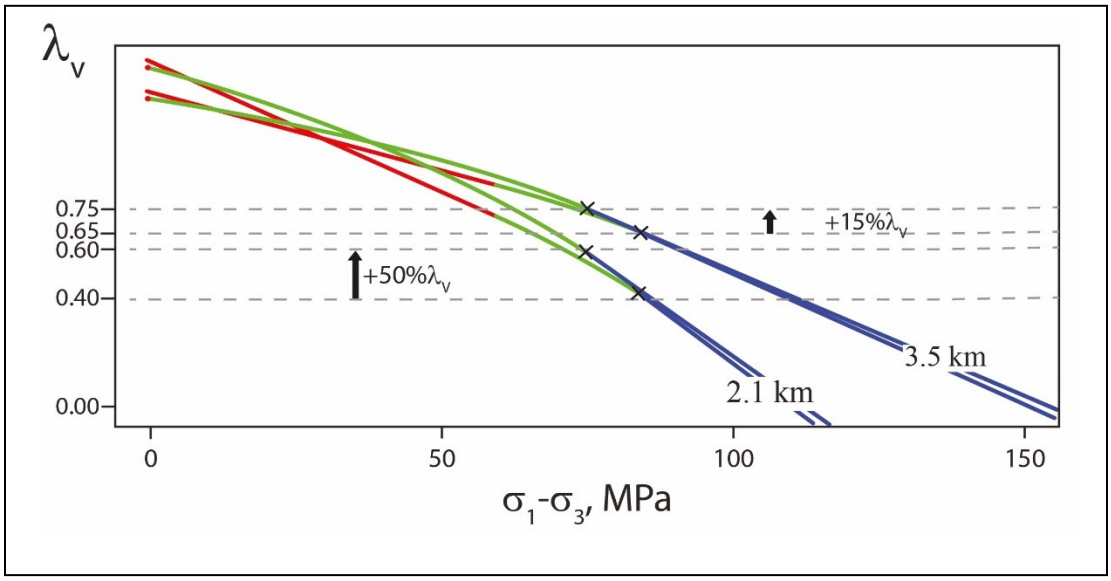

Figure 4-5. Comparison of the tectonic regimes registered in the ALFS exposure in the λ–σ space. Modes of failure are color-coded as in Figure 4-6. Points of transition between shear and hybrid extension+shear failure are marked with crosses, with their associated pore fluid factors. Black arrows indicate the minimum percentage increase in pore fluid pressures on switches between Andersonian strike-slip and non-Andersonian transtensional regimes.

A similar approach has been used by Hashimoto and Eida (2015), where pore pressure factors are calculated for vein development in an accretionary complex. Using the multiple inverse method for stress inversion (and therefore non-Andersonian regimes), they calculate τ and σ_n for all planes corresponding to the vein elements identified, using a normalized Mohr's circle (differential stress $\sigma = 1$ and $\sigma_3 = 0$). Following, effective friction coefficient is obtained from the slope between critically loaded vein planes in the normalized Mohr's circle (both veins with the minimum and maximum slip tendency, $T_s = \frac{\tau}{\sigma_n}$) (following Morris *et al.*, 1996), by using a non-cohesive Mohr-Coulomb failure criteria. Finally, pore pressure factors are calculated from the analytical theory of Coulomb wedges (Dahlen, 1984),

depending inversely of the effective friction coefficient. However, I argue that the method presented here is more representative of fracture-vein systems development. In this work, the structural data used for stress inversion is entirely different of the vein system upon which the pore pressure analysis was undertaken. Therefore, any recursive inference is avoided. On the other hand, cohesion must be considered in failure analysis, especially given the significance of healing processes in hydrothermal systems (Tenthorey *et al.*, 2003). Moreover, as presented in this work, textural analysis evidences not only the existence of shear failure, but extension and hybrid failure also, implying that other failure criteria rather than Mohr-Coulomb must be used to capture these failure mechanisms (such as generalized Griffith). Finally, considering an average orientation of a fracture-vein system, as done here, may lead to a better approximation of pore fluid factors, in opposite to defining two end-members of the data set, which is rather sensitive to the choice of the critically loaded structural elements.

4.5 Electrical resistivity model and hydrothermal mineralogy

The electrical resistivity sections in plan view were obtained by *in situ* measurements, and therefore, thus the electrical response of such profiles corresponds to the studied fault zones; in turn, the cross-section profiles were obtained from electrodes installed in the ground, so the registered anomalies could correspond to the integrated response of a shallow coverage of sediments, plus upper rock layers. Additionally, it could correspond to the accumulation of water within the porous sediment layers (e.g.

Colella *et al.*, 2004). Given all these uncertainties, I decided to focus the analysis in the plan view profiles only.

When crossing out the information from the structural mapping and the 2D electrical survey performed with the electrodes directly installed in the rock, it can be observed that the architectural domains of outcrops 1 and 2 are recognized in the geoelectrical section (Figure 4-7 and Figure 4-8): in both cases the core is a relative conductor with respect to the more resistive hanging and footwall blocks (Figure 3-10, domain 2 in Figure 4-8 and Figure 4-7). Statistical comparison between resistivity values in the hanging wall and the footwall is not necessarily representative in the case of the splay fault of the LOFS, since the hanging wall has a comparatively small sample (Figure 3-10). However, in the ALFS segment, the hanging wall and the footwall blocks are statistically comparable. A humble variation of resistivity values compared to the dispersion of the data can be observed (Figure 3-10), where the more damaged hanging wall is slightly more conductive than the less fractured footwall. Therefore, only a slight resistivity difference between the damages zones of outcrop 1 and 2 should be identified, despite the fact that greater damage is clearly seen in the hanging wall block of both exposures.

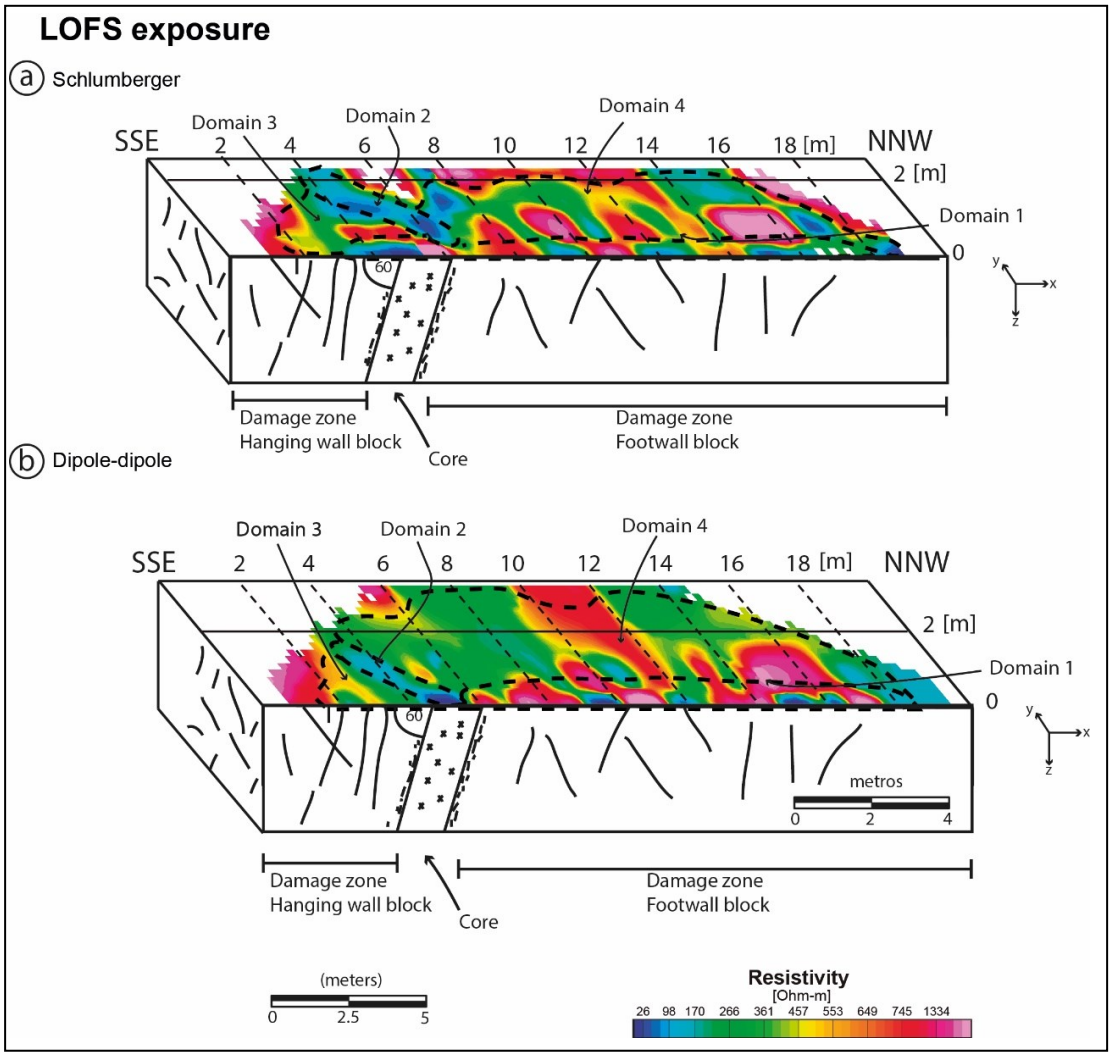

Figure 4-7. Cartoon illustrating the combined structural and electrical results. Domain 1 corresponds to the weathered volume of exposed rock; domain 2 is the fault core (a relative conductor); domain 3 represents the hanging wall block; and domain 4 is the footwall block.

An interesting observation regarding fault zone geometry is that the different performed surveys could reflect the strike of the core: the outcrop 1 (LOFS exposure) displays a WNW-striking conductor body and the outcrop 2 (ALFS exposure) shows a NW-striking body in the same positions of the respective cores, as indicated by the structural mapping. Additionally, the spatial dimensions of the cores determined by

the structural mapping are in fair good agreement with the geoelectrical measurements. However, the cross-section resistivity profile (electrodes installed in the ground) was not able to discriminate the dip of the fault cores.

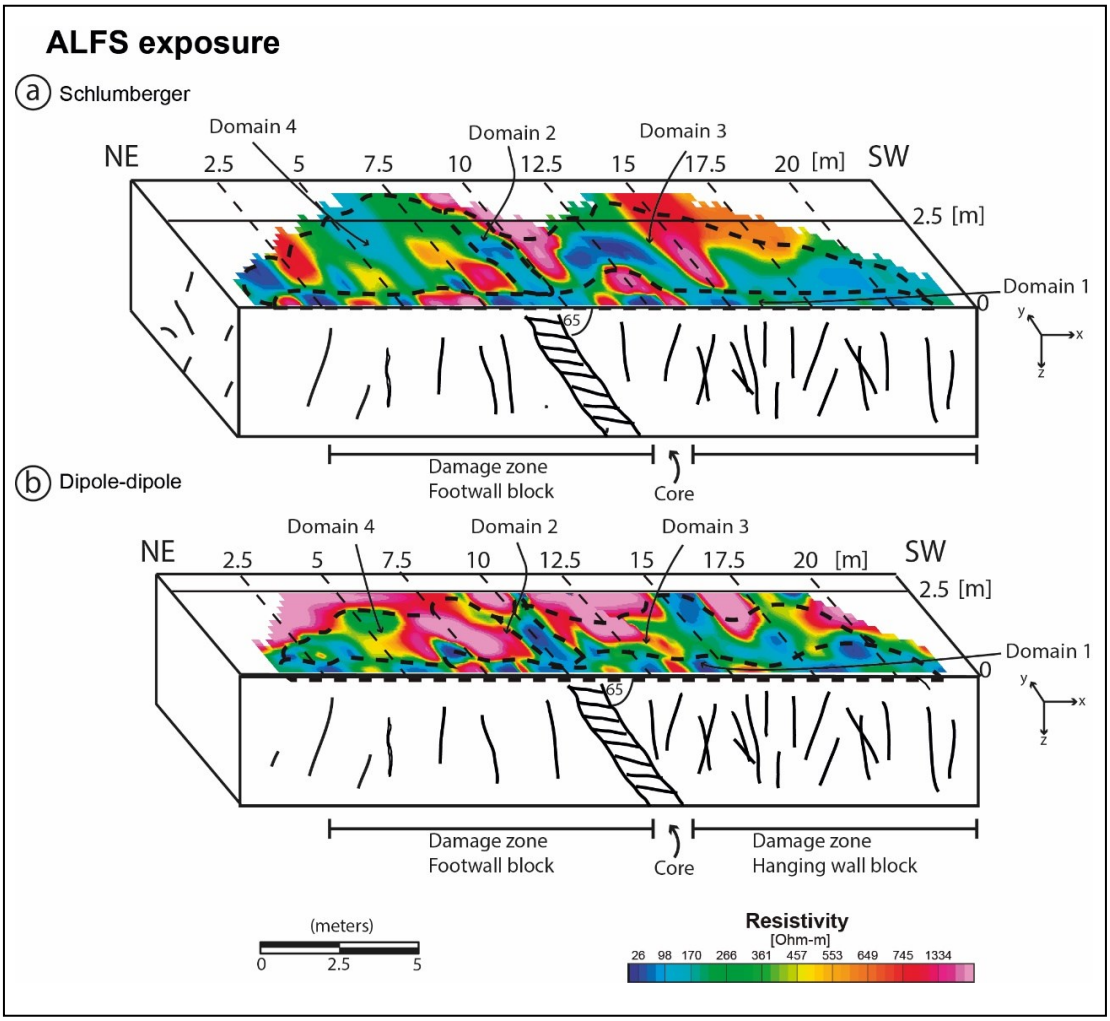

Figure 4-8. Cartoon illustrating the combined structural and electrical results in the LOFS exposure. Domain 1 corresponds to the weathered volume of exposed rock; domain 2 is the fault core (a relative conductor); domain 3 represents the hanging wall block; and domain 4 is the footwall block. See text for discussion.

The obtained resistivity values for the cores are in fair good agreement with the observed resistivities in other works, where the faults are always shown as a relative conductor with values that usually range between 1-200 ohm-m (Giano *et al.*, 2000;

Storz *et al.*, 2000; Suzuki *et al.*, 2000; Unsworth *et al.*, 2000; Caputo *et al.*, 2007; Díaz *et al.*, 2014). The comparison between the main structural domains (core *vs.* damage zone) was not possible, since in the revised works no distinction between fault core and damage zone was made.

In shallow structural environments, the measured electrical resistivity is determined by water content, rock mineralogy, concentration of dissolved ions, and temperature (Grant and West; 1965, Zohdy *et al.*, 1974; Revil *et al.*, 1998). The effect of water content and porous media has been widely recognized as the first order factor for measured electrical resistivity in sedimentary contexts and also in fault zones (Colella *et al.*, 2004; Caputo *et al.*, 2007; Ball *et al.*, 2010; Díaz *et al.*, 2014), suggesting that more water content and more porous environments result in a decrease in electrical resistivity. For this reason, an interesting point is how the conductive core and slightly-conducive hanging wall could be trapping more water than the less fractured, slightly-resistive footwall. I propose that the observed relative conductivity of the core and the fractured hanging wall is a reflection of the prevailing hydrothermal mineralogy: in both exposures the core and the structural elements within the damage zones are zeolite-bearing structures. Zeolites are alumina-rich tectosilicates that are industrially used as commercial adsorbents due to their microporous nature (e.g. Bish and Ming, 2001). This makes zeolites natural water-bearing materials, which could explain the measured resistivities. This idea is reinforced when comparing with the estimated hydrothermal mineralogy proportion in both outcrops (Table 3-1). The biggest areal percentage of zeolites are in the conductor cores (δ_C=12-37.5%), which is one order of magnitude more than the hanging and footwall blocks (δ_H=7.10 -9.60%

and δ_F=2.90-5.60%, respectively). Likewise, the modestly-conductor hanging wall has slightly-higher proportion of hydrothermal mineralogy, compared to the resistive footwall block. This analysis suggests that there is a positive correlation between damage and electrical conductivity, corroborated by combining the results from the structural mapping, XRD mineralogy and electrical measurements.

4.6 Formation of shallow hydrothermal systems and structural targets for geothermal exploration

The Andean Earthquake Cycle has two distinctive stages (e.g. González *et al.*, 2003; Aron *et al.*, 2013): (1) the interseismic period (*Andean interseismic*), that provides the long-term stress conditions and occurs between each megathrust interplate earthquake (*ca.* $M_w > 8$) and is characterized by a compression of the continental plate, and (2) co- and postseismic period (*Andean co- and postseismic*), respectively produced during and after a megathrust interplate earthquake, that provides short-term stress conditions, where a relaxation of the continental plate takes place. Multi-scale structural analyses suggest that the fundamental mechanical principles governing fault zone behavior remain scale-invariant, at least between 9 orders of magnitude (from the cm to the km scale) (Jensen *et al.*, 2011). In this manner, the meso- and micro structural analysis presented here could illuminate about a more regional behavior of the crustal LOFS and ALFS.

Assuming the observed meso- and microstructural features can extrapolate to a regional behavior, a proposed mechanism for the formation of metric-scale shallow

hydrothermal systems in the Southern Andes is summarized in Figure 4-9. The N83°W/65°S studied splay fault of the LOFS seems to accommodate a tensor apparently coupled with long-term stress conditions during Andean interseismic. Continuous fluid flow through EW to NE-striking discontinuities, favorably oriented for transtensional failure, seems to develop under this regime. The idea of *constant* failure is supported by textural features summarized in Section 4.1, and also by the occurrence of NNE-striking dextral slip surfaces (microstructural map in Figure 3-5), here interpreted to have formed under *progressive* shear. The N45°W/60°SW specific segment of the ALFS is severely misoriented with respect to the prevalent stress conditions, likely producing a near-Andersonian strike-slip regime, although transpressional failure may be induced under comparatively low pore fluid pressures (Figure 4-9). Such a scenario could promote the generation of fault bound compartments (e.g. below the attrition breccia in Figure 3-7), which may facilitate the storage of over pressured hydrothermal fluids. The existence of such compartments has also been inferred by other authors (e.g. Sánchez, 2015), who suggest that the WNW-striking faults of the ALFS, unfavorable oriented for reactivation under the prevalent stress conditions, promote long-time residence of magma (e.g. Cembrano and Lara, 2009).

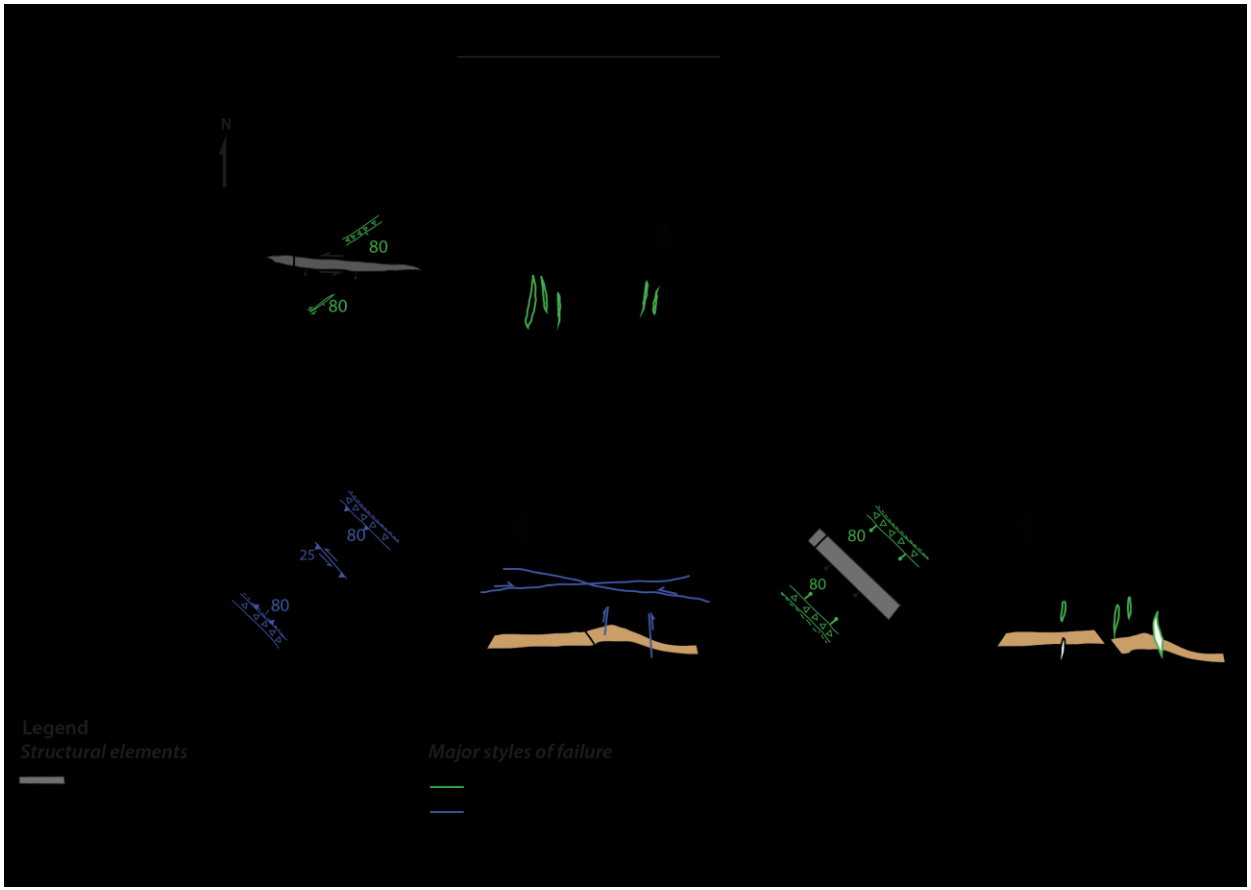

Figure 4-9. Conceptual model of the formation of shallow hydrothermal systems in the Southern Andes. The LOFS exposure registers continuous fluid flow through NE to EW-striking extensional discontinuities, probably under long-term stress conditions (Andean interseismic), expressed as a strike-slip stress tensor. The behavior during Andean co/postseismic is not registered in the studied local splay fault. On the other hand, the ALFS specific segment records a switch in the tectonic regime, from a strike-slip stress tensor that favors failure in shear, probably produced by long-term stress conditions. Such a scenario could promote the storage of increasingly overpressured fluids under capping structures, facilitating expulsions in large volumes after during a reversion to a to a transtensional stress regime. See text for further discussion.

This work provides additional evidence, suggesting that a kinematic switch to a non-Andersonian transtensional regime could facilitate expulsions in large volumes within vertical high-flux pathways, possibly triggered by the co- and postseismic relaxation of the continental plate after a subduction megathrust earthquake, as already documented in crustal fore-arc faults in the Andean Margin (e.g. González *et al.*, 2003; Farías *et al.*, 2011; Aron *et al.*, 2013)

In summary, long-term stress conditions favor: (1) the storage of hydrothermal reservoirs associated to the ALFS faults, and (2) continuous fluid flow through vertical high-flux conduits in the EW-striking faults of the LOFS. Therefore, the interplay between the activation of the studied systems allows two of the basic requirements for the occurrence of geothermal systems: an architecture that permits the transportation of previously stored hydrothermal fluids. In this manner, these results suggest that targets of geothermal exploitation are areas of interaction between the NW-striking and EW-striking faults of the ALFS and LOFS, respectively. Furthermore, the electrical resistivity models of the exposures suggest that structural domains respond as conductive anomalies, when they are proportionally filled with more hydrothermal material (and therefore, larger volumes of fluids have flown in such domains), which could indicate that episodic fluid flow occurred in both the core and damage zones of the studied exposures.

These results provide new insights on the behavior of tectonically controlled geothermal systems in the Southern Andes, and could help to constrain efficient

strategies for geological and geophysical prospection of blind geothermal systems.

5. CONCLUSIONS

The Liquiñe-Ofqui Fault System (LOFS) and the Arc-oblique Long-lived Fault System (ALFS) domains were studied on the outcrop-scale, based on its textural, mineralogical and structural features. The main conclusions of this work are:

(1) The studied exposures of the LOFS and the ALFS have simple cores and asymmetric damage zones, with more fracture density in the hanging wall than in the footwall block. Additionally, the damage zone in the hanging wall block of both exposures has greater areal proportion of hydrothermal mineralogy than the footwall. Five families were distinguished in the analyzed outcrops: (i) hydrothermal breccia (LOFS exposure: N5-90°E/80-85°S, ALFS exposure: N45-85°W/80°S); (ii) fault-localized hydrothermal breccia (LOFS exposure: not present, ALFS exposure: 45°W/80°SW); (iii) vein (LOFS exposure: N50-60°E/85°S, ALFS exposure: 20-35°W/85°S); (iv) fault-vein (LOFS exposure: dextral-reverse and dextral-normal N65-90°E/80°S surfaces, ALFS exposure: sinistral N5-45°W/subvertical surfaces); (v) fault (LOFS exposure: dextral-reverse N5-45°E/subvertical surfaces, ALFS exposure: reverse N40-50°W/25-30°S surfaces).

(2) In the LOFS outcrop, mostly hydrothermal breccias occur, and therefore this exposure registers a dominance of failure in extension (±shear). In turn, in the ALFS segment, fault-localized hydrothermal breccias preferentially

occur, and consequently this outcrop registers two alternated modes of brittle failure: (1) extensional (±shear) and (2) shear (±extensional) failure.

(3) The dominant minerals detected through XRD in the study areas are Ca-Na rich zeolites, found in geothermal systems as a result of the interaction of chloride hydrothermal fluids of near-neutral pH and volcanic rocks. Syntectonic zeolites in the damage zones of the LOFS and the ALFS exposures suggest certain temperatures (LOFS: 110-170ºC and 120ºC; ALFS: 110-170ºC, 120ºC and 210ºC), that combined typical intra-arc geothermal gradients indicate approximate paleodepths between 2.1-3.5 km at the time of vein formation.

(4) Architectural features in the studied exposures suggest that: (1) the analyzed splay fault of the LOFS cyclically fails in transtension under a near-Andersonian strike-slip regime (i.e. $\sigma_2 \approx \sigma_V$) and (2) the analyzed segment of the ALFS suggests switches in the outcrop-scale stress regimes, changing between failure in transpression under a near-Andersonian strike-slip regime ($\sigma_2 \approx \sigma_V$) and failure in transtension under a non-Andersonian transtensional regime (i.e. $\sigma_X \neq \sigma_V$, for x = 1, 2, 3).

(5) Modeled failure envelopes in the λ-σ space indicate that: (1) in the LOFS exposure, failure in the Andersonian strike-slip likely occurs between typical ranges of pore fluid pressures and low depth (<2 km); and (2) in the ALFS exposure, a switch from an Andersonian strike-slip to a non-Andersonian

transtensional regime generates hybrid extensional+shear structures, only possible at overpressures given by $\lambda_V \geq 0.6$ for z=2.1 km (λ_V >50% above cold hydrostatic pressure) and $\lambda_V \geq 0.75$ for z=3.5 km (λ_V >88% above cold hydrostatic pressure).

(6) Geoelectrical measurements indicate that the cores in the metric-scale exposures of the LOFS and ALFS is shown as a clear, localized relative conductor (1-200 ohm-m) and the fractured damage zone in the hanging wall block is a slightly conductive volume compared to the less fractured damage zone in the footwall. Electrical conductivity is in good correlation with the areal proportion of zeolitic mineralogy within the structural domains, which suggests that there is a positive correlation between damage and electrical conductivity. Consequently, this work provides direct proof that electrical methods can be used to characterize blind inactive or active fault zones.

(7) Finally, related to geothermal exploration, long-term stress conditions in the northern end of the LOFS favor: (1) the storage of increasingly overpressured fluids in hydrothermal reservoirs associated to the ALFS faults, and (2) continuous fluid flow through vertical high-flux conduits in the EW-striking faults of the LOFS. Geothermal exploitation requires an architecture that both cumulates and transports hydrothermal fluids, which could be given by the interactions of the NW-striking and EW-striking faults of the ALFS and LOFS, respectively.

REFERENCES

Anderson, M. (1951) *The Dynamics of Faulting*, 2nd Editio. Edinburgh.

Arancibia, G., Cembrano, J. and Lavenu, A. (1999) Transpresión dextral y partición de la deformación en la Zona de Falla Liquiñe-Ofqui, Aisén, Chile (44-45°S). *Revista geológica de Chile*.

Aravena, D. and Lahsen, A. (2012) Assessment of Exploitable Geothermal Resources Using Magmatic Heat Transfer Method , Maule Region , Southern Volcanic Zone , Chile. *GRC Transactions* **36**, 1307–1314.

Aravena, D., Muñoz, M., Morata, D., Lahsen, A., Parada, M. A. and Dobson, P. (2016) Assessment of high enthalpy geothermal resources and promising areas of Chile. *Geothermics* **59**, 1–13. doi:10.1016/j.geothermics.2015.09.001

Araya, J. (2005) *Geometría de los depósitos y plutones del Jurásico superior-Cretácico Inferior en la Cordillera de la Costa entre Taltal (25°30'S) y Vallenar (28°35'). Una aproximación geológica y geofísica integrada.* Universidad de Chile.

Aron, F., Allmendinger, R., Cembrano, J., González, G. and Yáñez, G. (2013) Permanent fore-arc extension and seismic segmentation: Insights from the 2010 Maule earthquake, Chile. *Journal of Geophysical Research: Solid Earth* **118**(2), 724–739. doi:10.1029/2012JB009339

Ball, L. B., Ge, S., Caine, J. S., Revil, A. and Jardani, A. (2010) Constraining fault-zone hydrogeology through integrated hydrological and geoelectrical analysis. *Hydrogeology Journal* **18**(5), 1057–1067. doi:10.1007/s10040-010-0587-z

Balsamo, F., Storti, F. and Salvini, F. (2010) Structural and petrophysical evolution of extensional fault zones in low-porosity, poorly lithified sandstones of the Barreiras Formation, NE Brazil. *Journal of Structural Geology*.

Beeler, N. M. and Hickman. (2004) Stress-induced, time-dependent fracture closure at hydrothermal conditions. *Journal of Geophysical Research* **109**(B2), B02211. doi:10.1029/2002JB001782

Biggs, J., Nissen, E., Craig, T., Jackson, J. and Robinson, D. P. (2010) Breaking up the hanging wall of a rift-border fault: The 2009 Karonga earthquakes, Malawi. *Geophysical Research Letters* **37**(11), n/a–n/a. doi:10.1029/2010GL043179

Bish, D. and Ming, D. (2001) Natural zeolites: occurrence, properties, applications.

Bish, D. and Post, J. (1989) Modern Powder Diffraction. *Review in Mineralogy* **20**(Mineralogical Society of America).

Bons, P. D., Elburg, M. A. and Gomez-Rivas, E. (2012) A review of the formation of

tectonic veins and their microstructures. *Journal of Structural Geology* **43**, 33–62. doi:10.1016/j.jsg.2012.07.005

Brown, S., Caprihan, A. and Hardy, R. (1998) Experimental observation of fluid flow channels in a single fracture. *Journal of Geophysical Research* **103**(B3), 5125. doi:10.1029/97JB03542

Browne, P. (1978) Hydrothermal alteration in active geothermal fields. *Annual review of Earth and Planetary Sciences* **6**, 229–250.

Browne, P. (1993) Application of mineralogical methods to asses the thermal stabilities of Geothermal Reservoirs. *Eighteenth Workshop on Geothermal Reservoir Engineering*. California.

Caine, J., Evans, J. and Forster, C. (1996) Fault zone architecture and permeability structure. *Geology*.

Caputo, R., Salviulo, L., Piscitelli, S. and Loperte, A. (2007) Late Quaternary activity along the Scorciabuoi Fault (Southern Italy) as inferred from electrical resistivity tomographies.

Cembrano, J., Hervé, F. and Lavenu, A. (1996) The Liquine Ofqui fault zone: a long-lived intra-arc fault system in southern Chile. *Tectonophysics*.

Cembrano, J. and Lara, L. (2009) The link between volcanism and tectonics in the southern volcanic zone of the Chilean Andes: A review. *Tectonophysics* **471**(1-2), 96–113. Elsevier B.V. doi:10.1016/j.tecto.2009.02.038

Cembrano, J. and Lara, L. (2009) The link between volcanism and tectonics in the southern volcanic zone of the Chilean Andes: a review. *Tectonophysics*.

Cho, M., Maruyama, S. and Liou, J. (1987) An experimental investigation of heulandite-laumontite equilibrium at 1000 to 2000 bar P fluid. *Contributions to Mineralogy and Petrology*.

Cole, J. (1990) Structural control and origin of volcanism in the Taupo volcanic zone, New Zealand. *Bulletin of volcanology*.

Colella, A., Lapenna, V. and Rizzo, E. (2004) High-resolution imaging of the High Agri Valley Basin (Southern Italy) with electrical resistivity tomography. *Tectonophysics* **386**(1-2), 29–40. doi:10.1016/j.tecto.2004.03.017

Cox, S. (2005) Coupling between deformation, fluid pressures, and fluid flow in ore-producing hydrothermal systems at depth in the crust. *Economic Geology* **100th Anni**, 39–75.

Cox, S. (2010) The application of failure mode diagrams for exploring the roles of

fluid pressure and stress states in controlling styles of fracture-controlled permeability enhancement in faults and shear zones. *Geofluids* **10**, 217–233. doi:10.1111/j.1468-8123.2010.00281.x

Dahlen, F. A. (1984) Noncohesive critical Coulomb wedges: An exact solution. *Journal of Geophysical Research* **89**(B12), 10125. doi:10.1029/JB089iB12p10125

Deer, W., Howie, R., Wise, W. and Zussman, J. (2004) Framework silicates: silica minerals, feldspathoids and the zeolites.

Dempsey, E., Holdsworth, R., Imber, J., Bistacchi, A. and Toro, G. Di. (2014) A geological explanation for intraplate earthquake clustering complexity: The zeolite-bearing fault/fracture networks in the Adamello Massif (Southern Italian Alps). *Journal of Structural Geology* **66**, 58–74.

Díaz, D., Maksymowicz, A., Vargas, G., Vera, E., Contreras-Reyes, E. and Rebolledo, S. (2014) Exploring the shallow structure of the San Ramón thrust fault in Santiago, Chile (~33.5° S), using active seismic and electric methods. *Solid Earth* **5**(2), 837–849. doi:10.5194/se-5-837-2014

Dong, G., Morrison, G. and Jaireth, S. (1995) Quartz textures in epithermal veins, Queensland; classification, origin and implication. *Economic Geology*.

Farías, M., Comte, D., Roecker, S., Carrizo, D. and Pardo, M. (2011) Crustal extensional faulting triggered by the 2010 Chilean earthquake: The Pichilemu Seismic Sequence. *Tectonics* **30**(6), n/a–n/a. doi:10.1029/2011TC002888

Faulkner, D., Lewis, A. and Rutter, E. (2003) On the internal structure and mechanics of large strike-slip fault zones: field observations of the Carboneras fault in southeastern Spain. *Tectonophysics*.

Faulkner, D. R., Jackson, C. A. L., Lunn, R. J., Schlische, R. W., Shipton, Z. K., Wibberley, C. A. J. and Withjack, M. O. (2010) A review of recent developments concerning the structure, mechanics and fluid flow properties of fault zones. *Journal of Structural Geology* **32**(11), 1557–1575. doi:10.1016/j.jsg.2010.06.009

Folguera, A., Ramos, V. A. and Melnick, D. (2002) Partición de la deformación en la zona del arco volcánico de los Andes neuquinos (36-39°S) en los últimos 30 millones de años. *Revista geológica de Chile* **29**(2), 227–240. Servicio Nacional de Geología y Minería. doi:10.4067/S0716-02082002000200005

Giano, S. I., Lapenna, V., Piscitelli, S. and Schiattarella, M. (2000, December 25) Electrical imaging and self-potential survayes to study the geological setting of the Quaternary, slope depositsin the Agri high valley (Southern Italy). *Annals of Geophysics*. doi:10.4401/ag-3642

González, G., Cembrano, J., Carrizo, D., Macci, A. and Schneider, H. (2003) The link

between forearc tectonics and Pliocene–Quaternary deformation of the Coastal Cordillera, northern Chile. *Journal of South American Earth Sciences* **16**(5), 321–342. doi:10.1016/S0895-9811(03)00100-7

Grant, F. and West, G. (1965) Interpretation theory in applied geophysics: part 3, electrical conduction and electromagnetic induction methods.

Jébrak, M. (1997) Hydrothermal breccias in vein-type ore deposits: A review of mechanisms, morphology and size distribution. *Ore Geology Reviews* **12**(3), 111–134. doi:10.1016/S0169-1368(97)00009-7

Jensen, E., Cembrano, J., Faulkner, D., Veloso, E. and Arancibia, G. (2011) Development of a self-similar strike-slip duplex system in the Atacama Fault system, Chile. *Journal of Structural Geology* **33**(11), 1611–1626. doi:10.1016/j.jsg.2011.09.002

Kristmannsdóttir, H. and Tómasson, J. (1978) Zeolite zones in geothermal areas in Iceland. *Natural Zeolites: Occurrence, Properties, Use* 277–284.

Krupp, R. and Seward, T. (1987) The Rotokawa geothermal system, New Zealand; an active epithermal gold-depositing environment. *Economic Geology*.

Lange, D., Cembrano, J., Rietbrock, A., Haberland, C., Dahm, T. and Bataille, K. (2008) First seismic record for intra-arc strike-slip tectonics along the Liquiñe-Ofqui fault zone at the obliquely convergent plate margin of the southern Andes. *Tectonophysics* **455**(1-4), 14–24. doi:10.1016/j.tecto.2008.04.014

Lavenu, A. and Cembrano, J. (1999) Compressional-and transpressional-stress pattern for Pliocene and Quaternary brittle deformation in fore arc and intra-arc zones (Andes of Central and Southern. *Journal of Structural Geology*.

Liou, J. G., Capitani, C. de and Frey, M. (1991) Zeolite equilibria in the system CaAl2Si 2O8 - NaAlSi3O8 - SiO2 - H2O. *New Zealand Journal of Geology and Geophysics* **34**(3), 293–301. doi:10.1080/00288306.1991.9514467

Liou, J., Maruyama, S. and Cho, M. (1987) Very low-grade metamorphism of volcanic and volcaniclastic rocks-mineral assemblages and mineral facies. *Low temperature metamorphism*.

Lowrie, W. (2007) *Fundamentals of Geophysics*.

Lunn, R. J. and Willson, J. (2008) Simulating brittle fault growth from linkage of preexisting structures. *Journal of Geophysical Research*.

Main, I., Kwon, O., Ngwenya, B. and Elphick, S. (2000) Fault sealing during deformation-band growth in porous sandstone. *Geology*.

Melnick, D., Bookhagen, B., Strecker, M. R. and Echtler, H. P. (2009) Segmentation of megathrust rupture zones from fore-arc deformation patterns over hundreds to millions of years, Arauco peninsula, Chile. *Journal of Geophysical Research* **114**(B1), B01407. doi:10.1029/2008JB005788

Melnick, D. and Echtler, H. (2006) Morphotectonic and geologic digital map compilations of the south-central Andes (36–42°S). *The Andes*.

Moreno, M., Melnick, D., Rosenau, M., Bolte, J., Klotz, J., Echtler, H., Baez, J., et al. (2011) Heterogeneous plate locking in the South–Central Chile subduction zone: Building up the next great earthquake. *Earth and Planetary Science Letters* **305**(3-4), 413–424. doi:10.1016/j.epsl.2011.03.025

Morris, A., Ferrill, D. A. and Henderson, D. B. (1996) Slip-tendency analysis and fault reactivation. *Geology* **24**(3), 275–278. doi:10.1130/0091-7613(1996)024

Morrow, C. A., Moore, D. E. and Lockner, D. A. (2001) Permeability reduction in granite under hydrothermal conditions. *Journal of Geophysical Research* **106**(B12), 30551. doi:10.1029/2000JB000010

Nesse, W. (2000) Introduction to mineralogy.

Olson, J. E. and Pollard, D. D. (1991) The initiation and growth of en échelon veins. *Journal of Structural Geology* **13**(5), 595–608. doi:10.1016/0191-8141(91)90046-L

Pérez-Flores, P., Cembrano, J., Sánchez-Alfaro, P. and Veloso, A. (2015) Tectonics, magmatism and fluid flow in a strike-slip setting: The northern termination of the Liquiñe-Ofqui Fault System, Chile. *XIV Congreso Geológico Chileno*, 4. La Serena.

Petit, J. P. (1987) Criteria for the sense of movement on fault surfaces in brittle rocks. *Journal of Structural Geology* **9**(5-6), 597–608. doi:10.1016/0191-8141(87)90145-3

Raith, M., Raase, P. and Reinhardt, J. (2012) *Guide to Thin Section Microscopy*, 2nd Editio.

Ramsay, J. G. (1980) Shear zone geometry: A review. *Journal of Structural Geology* **2**(1-2), 83–99. doi:10.1016/0191-8141(80)90038-3

Ramsay, J. G. (1980) The crack–seal mechanism of rock deformation. *Nature* **284**(5752), 135–139. doi:10.1038/284135a0

Reuther, C., Potent, S. and Bonilla, R. (2003) Crustal stress history and geodynamic processes of a segmented active plate margin; south-central Chile: the Arauco Bío-bío Trench Arc Systems. *Congreso Geológico Chileno*.

Revil, A., Cathles, L. M., Losh, S. and Nunn, J. A. (1998) Electrical conductivity in shaly sands with geophysical applications. *Journal of Geophysical Research* **103**(B10),

23925. doi:10.1029/98JB02125

Rivera, O. and Cembrano, J. (2000) Modelo de formación de cuencas volcano-tectónicas en zonas de transferencia oblicuas a la cadena andina: el caso de las cuencas Oligo-Miocenas de Chile. *Congreso Geológico Chileno*.

Rivera, O. and Yáñez, G. (2009) Naturaleza y rol de estructuras translitosféricas en la evolución del arco volcánico oligo-mioceno de Chile Central entre los 32 y 34 S. *Congreso Geológico Chileno*.

Rosenau, M., Melnick, D. and Echtler, H. (2006) Kinematic constraints on intra-arc shear and strain partitioning in the southern Andes between 38°S and 42°S latitude. *Tectonics* **25**(4). doi:10.1029/2005TC001943

Rowland, J. V. and Sibson, R. H. (2004) Structural controls on hydrothermal flow in a segmented rift system, Taupo Volcanic Zone, New Zealand. *Geofluids* **4**(4), 259–283. doi:10.1111/j.1468-8123.2004.00091.x

Rowland, J. V. and Simmons, S. F. (2012) Hydrologic, magmatic, and tectonic controls on hydrothermal flow, Taupo Volcanic Zone, New Zealand: Implications for the formation of epithermal vein deposits. *Economic Geology* **107**(3), 427–457. doi:10.2113/econgeo.107.3.427

Rowland, S., Duebendorfer, E. and Schiefelbein, I. (2013) Structural analysis and synthesis: a laboratory course in structural geology.

Salfity, J. (1985) Lineamientos transversales al rumbo Andino en el noroeste Argentino. *IV Congreso Geologico Chileno*. Antofagasta.

Sánchez, P. (2015) *Interplay between brittle deformation, fluid-rock interaction and mineralization in hydrothermal systems from the Southern Andes*. Universidad de Chile.

Sánchez, P., Pérez-Flores, P., Arancibia, G., Cembrano, J. and Reich, M. (2013) Crustal deformation effects on the chemical evolution of geothermal systems: the intra-arc Liquiñe–Ofqui fault system, Southern Andes. *International Geology Review* **55**(11), 1384–1400. Taylor and Francis. doi:10.1080/00206814.2013.775731

Sibson, R. H. (1977) Fault rocks and fault mechanisms. *Journal of the Geological Society*.

Sibson, R. H. (1986) Brecciation processes in fault zones: Inferences from earthquake rupturing. *Pure and Applied Geophysics PAGEOPH* **124**(1-2), 159–175. doi:10.1007/BF00875724

Sibson, R. H. (1989) Earthquake faulting as a structural process. *Journal of Structural Geology*.

Sibson, R. H. (1990) Conditions for fault-valve behaviour. *Geological Society, London, Special Publications* **54**(1), 15–28. doi:10.1144/GSL.SP.1990.054.01.02

Sibson, R. H. (1998) Brittle failure mode plots for compressional and extensional tectonic regimes. *Journal of Structural Geology* **20**(5), 655–660. doi:10.1016/S0191-8141(98)00116-3

Sibson, R. H. (1998) Brittle failure mode plots for compressional and extensional tectonic regimes. *Journal of Structural Geology* **20**(5), 655–660. doi:10.1016/S0191-8141(98)00116-3

Sibson, R. H. (2000) Fluid involvement in normal faulting. *Journal of Geodynamics* **29**(3-5), 469–499. doi:10.1016/S0264-3707(99)00042-3

Sibson, R. H. (2003) Thickness of the seismic slip zone. *Bulletin of the Seismological Society of America*.

Sillitoe, R. H. (2010) Porphyry Copper Systems. *Economic Geology* **105**(1), 3–41. doi:10.2113/gsecongeo.105.1.3

Simpson, C. and Schmid, S. (1983) An evaluation of criteria to deduce the sense of movement in sheared rocks. *Geological Society of America Bulletin* **94**(11), 1281–1288. doi:10.1130/0016-7606(1983)94

Somoza, R. and Ghidella, M. E. (2005) Convergencia en el margen occidental de América del Sur durante el Cenozoico: subducción de las placas de Nazca, Farallón y Aluk. *Revista de la Asociación Geológica Argentina* **60**(4), 797–809. Asociación Geológica Argentina.

Stein, R., King, G. and Rundle, J. (1988) The growth of geological structures by repeated earthquakes. Field examples of continental dip-slip faults. *Journal of Geophysical Research* **93**.

Storz, H., Storz, W. and Jacobs, F. (2000) Electrical resistivity tomography to investigate geological structures of the earth's upper crust. *Geophysical Prospecting* **48**(3), 455–471. doi:10.1046/j.1365-2478.2000.00196.x

Suarez, M. and Emparan, C. (1995) The stratigraphy, geochronology and paleophysiography of a Miocene fresh-water interarc basin, southern Chile. *Journal of South American Earth Sciences* **8**(1), 17–31. doi:10.1016/0895-9811(94)00038-4

Suárez, M. and Emparan, C. (1988) Geocronología y asociación de facies volcánicas y sedimentarias del Mioceno de Lonquimay, Chile (Lat. 38-39 S). *Congreso Geológico Chileno*.

Suárez, M. and Emparán, C. (1997) Hoja Curacautín, Regiones de la Araucanía y del

Bío-bío. *Servicio Nacional de Geología y Minería* **71**, 105 p Map 1:250.000.

Suzuki, K., Toda, S., Kusunoki, K., Fujimitsu, Y., Mogi, T. and Jomori, A. (2000) Case studies of electrical and electromagnetic methods applied to mapping active faults beneath the thick quaternary. *Engineering Geology* **56**(1-2), 29–45. doi:10.1016/S0013-7952(99)00132-5

Swapp, S. (2015) Scanning Electron Microscopy (SEM). *University of Wyoming*. Retrieved from http://serc.carleton.edu/research_education/geochemsheets/techniques/SEM.html

Taylor, G., Grocott, J., Pope, A. and Randall, D. (1998) Mesozoic fault systems, deformation and fault block rotation in the Andean forearc: a crustal scale strike-slip duplex in the Coastal Cordillera of northern Chile. *Tectonophysics*.

Telford, W. M., Geldart, L. P. and Sheriff, R. E. (1990) *Telford - Applied Geophysics*. *Book*.

Tenthorey, E., Cox, S. F. and Todd, H. F. (2003) Evolution of strength recovery and permeability during fluid–rock reaction in experimental fault zones. *Earth and Planetary Science Letters* **206**(1-2), 161–172. doi:10.1016/S0012-821X(02)01082-8

Unsworth, M., Bedrosian, P., Eisel, M., Egbert, G. and Siripunvaraporn, W. (2000) Along strike variations in the electrical structure of the San Andreas Fault at Parkfield, California. *Geophysical Research Letters* **27**(18), 3021–3024. doi:10.1029/2000GL011476

Ward, S. (1990) Resistivity and induced polarization methods. *Geotechnical and environmental geophysics*.

Weisenberger, T. and Bucher, K. (2010) Zeolites in fissures of granites and gneisses of the Central Alps. *Journal of Metamorphic Geology*.

Wilson, C. J. L. (1994) Crystal growth during a single-stage opening event and its implications for syntectonic veins. *Journal of Structural Geology* **16**(9), 1283–1296. doi:10.1016/0191-8141(94)90070-1

Woodcock, N. H. and Mort, K. (2008) Classification of fault breccias and related fault rocks. *Geological Magazine* **145**(03), 435–440. Cambridge University Press. doi:10.1017/S0016756808004883

Yamaji, A. (2000) The multiple inverse method: a new technique to separate stresses from heterogeneous fault-slip data. *Journal of Structural Geology* **22**(4), 441–452. doi:10.1016/S0191-8141(99)00163-7

Zhdanov, M. S. (2009) *Geophysical Electromagnetic Theory and Methods*.

Zohdy, A., Eaton, G. and Mabey, D. (1974) Application of surface geophysics to ground-water investigations.

APPENDIX

APPENDIX A: FUNDAMENTALS OF STRUCTURAL MAPPING

A.1 Geometrical attitude of planes and lines

Many geological elements can be spatially represented as planes or lines. Such representation constitutes the basis for spatial, geometrical, statistical kinematic and dynamic analyses. The geometrical attitude of a plane or line refers to the spatial orientation of that plane or line.

Planes are get fully characterized in space by two parameters known as *strike* and *dip* (Figure A-1a). The strike (ρ in Figure A-1a) is the angle between the horizontal line formed by the intersection of the plane of interest and a horizontal plane and the North; the strike is the vertical angle (μ in Figure A-1a) of an inclined plane measured in the dip direction (DD in Figure A-1a).

Analogously, lines are spatially characterized by two parameters known as *trend* and *plunge* (Figure A-1b). The trend (δ in Figure A-1b) is the angle between the projection of the line of interest in a horizontal plane and the North; the plunge is the vertical angle (β in Figure A-1b) between the projection of the line of interest in a horizontal plane and such line. Linear geologic elements are usually over a plane of known geometrical attitude. In that case, the geometrical attitude of that line can be represented by an angle referred to as *pitch* or *rake* (r in Figure A-1b). The rake is the angle formed by the line of interest and a horizontal line, measured in the plane that contains them.

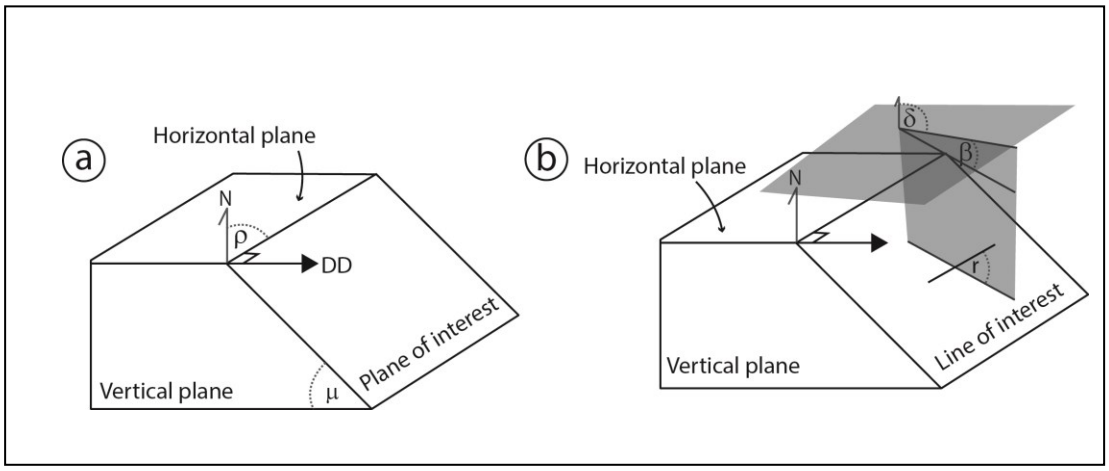

Figure A-1. a) Strike and dip of a plane. b) Trend and plunge of a line.

A.2 Brittle kinematic indicators (modified from Petit, 1987)

The determination of direction and sense of movement on slip surfaces (normal, reverse, dextral, sinistral– or any combination) is a basic requirement in brittle structural mapping. A useful way of determining the slip-sense is the direct observation of fault planes which may show not only striation, assumed parallel to the slip direction, but also minor repetitive structures making an angle with the fault plane. Such repeated secondary structures indicate the sense of movement and can be divided into three groups: (1) group T, including repetitive tension fractures at nearly 45º from the plane of principal movement M; (2) group R, including all types showing secondary striated shear fractures at nearly 15º and 75º from the plane of principal movement M; (3) group P, including all kinds that show secondary shear fractures at <10º from the plane of principal movement M.

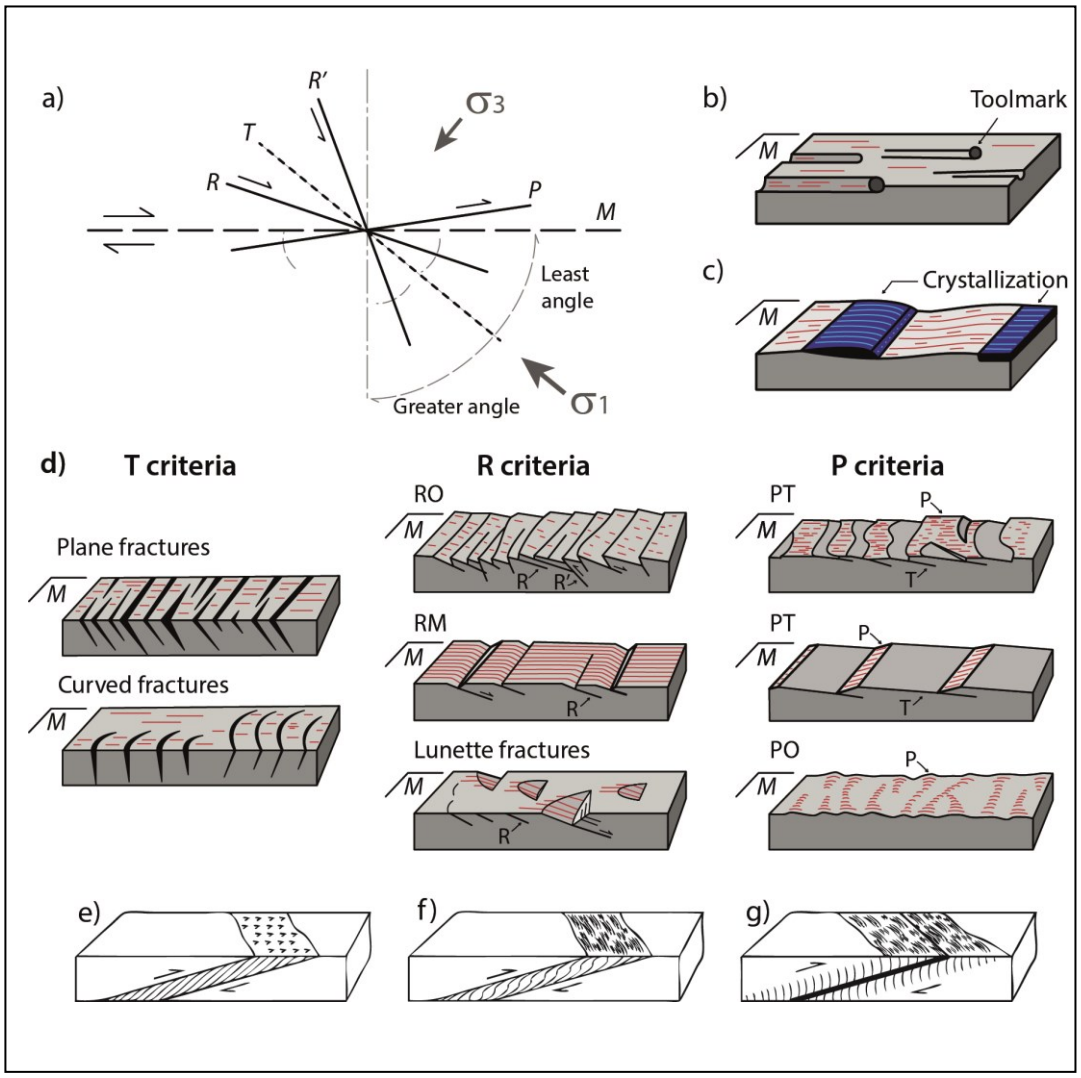

Figure A-2. Brittle kinematic indicators. a) cartoon showing angles between secondary structures and the fault plane (M). b) Toolmarks. c) Steps filled with hydrothermal minerals; d) T, R y P criteria ; e) Foliated gouge f) Sigmoidal cleavage in fault gouge; g) Cleavage in carbonates. Modified from de Petit, (1987) and Allmendinger (1990).

The recognition of these fractures in the field, and the careful comparison with the available models for the T, R and P fractures allows the interpretation of the sense of movement. The criteria for field recognition and determination of sense of movement can be shortly summarized as following: (1) secondary T fractures are recognized because they are not striated. T fractures can be open or infilled with hydrothermal minerals;

(2) secondary R fractures are recognized when the mean fault plane M is fully striated and joined with repeated striated R fractures at small angles to the fault plane; (3) secondary P fractures are recognized when the fault plane is always incompletely striated, where the bruised surface appears localized on the side of the asperities facing the movement of the missing block.

A.3 Textural features of veins in brittle structural domains

In a broad sense, veins are defined as mineral aggregates that precipitated from a fluid in dilatational sites in a process referred to as crack-seal event. Veins exhibit a wide range of internal structures or *textures* resulting from different combinations of crystal shape (blocky, fibrous, etc.) and growth direction (from the wall into the vein or in the opposite direction) (Bons *et al.*, 2012). For present purposes, it is convenient to make a distinction between primary and secondary textures in veins. Primary textures are defined here as the textures resulting from a single crack-seal event, whereas secondary textures result from at least two crack-seal events.

Different primary textures in veins belonging to tectono-hydrothermal systems have been recognized: massive, crustiform, cockade, colloform, moss, comb and zonal (Dong *et al.*, 1995 and references therein). Secondary textures, in turn, are defined here as brecciated textures, where at least two crack-seal events are recorded. A breccia is classically understood as a discontinuity composed of clasts and a matrix, and hydrothermal breccias are composed of hydrothermal matrix.

Hydrothermal breccias with hydrothermal clasts and matrix are defined here as secondary textures, so the clasts represent the first crack-seal event and the matrix represents the second crack-seal event.

A.4 Strengths and limitations

The most important strength of the structural mapping is that the determination of geometrical attitudes is a fast (<2 minutes per element) and with little margin of error. However, the natural limitation of determining the sense of shear using brittle kinematic indicators, and describing the textures in the discontinuities of the damage zones, is that inferences depend critically on the experience of the observer, being possible to have a range of variation in the interpretation of the geological processes involved in the genesis of such discontinuities.

APPENDIX B: FUNDAMENTALS OF OPTICAL MICROSCOPY

B.1 Fundamentals of optical mineralogy

In the wave theory, light is considered as a form of electromagnetic radiation that has electric and magnetic vectors vibrating in perpendicular angles. To understand the interaction between light and minerals, the forces arising from the magnetic component can be ignored, so only the electric vector will be considered in the discussion ahead.

Regular light coming directly from the Sun or a bulb vibrates in all directions at right angles to the direction of propagation. If the vibration of the light is constrained to a single plane, it is called *plane polarized light*. Modern petrographic microscopes use plane polarized light filtered by a polarizing film in the optical pathway. The polarizing film is an optically anisotropic material, which means that when light passes through and out of the polarizing film, its velocity is different in different directions. In this manner, the unpolarized light split into two plane polarized waves orthogonal to each other. One of the rays is weakly absorbed and passes through the polarizing film; the other one is just absorbed and eliminated.

The interaction of light and matter (through reflection, refraction and dispersion) depends on the nature of the material in which the light travels. For present purposes, it is necessary to make a distinction between optically isotropic and anisotropic materials. An optically isotropic material has the same average electron density in all directions, and therefore the velocity of ray of light that passes through it is the same in all directions. Geological examples of this kind

of materials are volcanic glass and minerals that belong to the isometric system. In turn, an optically anisotropic material has lower symmetry than isometric crystals, and the electron density varies according to the direction. Most of the rock-forming minerals, and the minerals studied in this work, are naturally anisotropic, so the atoms of such materials do not interact are unable to interact with light in the same way in all directions. Thus, the velocity or the absorption characteristics (color) of light vary with direction. The different optical properties of anisotropic minerals serve as the basis of mineral and textural identification. To study such variation, the petrographic microscope can be used.

B.2 Petrographic microscope

There are several types of petrographic microscopes, everyone different from each other in detail, but they all have fundamentally the same design and construction. From bottom to top, most of the optical microscopes are composed of: an illuminator, from which plane polarized light is provided; a lower polarizer or simply polarizer; a condensing lens; a microscope stage; a set of objective lenses; an upper polarizer, or simple analyzer; a Bertrand lens; and, finally, a pair of oculars. The general functioning of the different parts of the petrographic microscope will be revised in the following sections.

a. Illuminator

Most of the modern microscopes are equipped with an lightbulb mounted in the base to provide transmitted light. The light of the bulb is directed upward with a combination of lenses and mirrors. Then, the

light is filtered with a piece of blue glass that balances the artificial light, so it is similar to the sunlight. Some microscopes are also equipped with an aperture diagram that controls the size of the are illuminated in the thin section.

b. Lower polarizer

A lower polarizer basically consists of a polarizing film. In some microscopes, the lower polarizer can be rotated so the direction of the out coming polarized light may be controlled. Polarizers are also referred to as **Nicols** because Nicol calcite prisms were used in the early microscopes to polarize the light.

c. Condensing lens

A condensing lens consists of a series of lenses that serve to concentrate the light in the area right behind the objectives. Since the light that reaches the sample from the condensing lens is moderately convergent, this type of illumination may also be referred to as orthoscopic illumination.

d. Microscope stage

The circular stage of the petrographic microscopes is mounted on bearings so it can be smoothly rotated. The goniometer on the outside edge of the stage may be used to accurately determine angles of rotation.

e. Objective lenses

The objective lenses provide the primary magnification of the optical system, constituting the most important part of the microscope. The

used microscopes had different magnifications, e.g. 2x, 4x, 10x, 20x and 40x.

f. Upper polarizer (analyzer)

The upper polarized is also called analyzer. It is located up the objective lenses, and it is mounted in such a way that it can be inserted or removed the optical pathway. Just as in the lower polarizer, it is composed of a polarizing film, though Nicol prisms or equivalents are widely used in old microscopes. The direction of vibration of the upper polarizer can be adjusted in some microscopes, but it is usually orthogonal to that of the lower polarizer. When the upper polarizer is inserted, it is said that the upper and lower polarizer are **crossed**; when there is nothing on the microscope stage, the field of view is dark because all the light from the lower polarizer is absorbed in the analyzer. If the upper polarizer is removed, the view through the microscope is with **plane light** because the light from the lower polarizer is plane polarized.

g. Bertrand lens

The Bertrand lens is a small optical element mounted just below the ocular on a pivot or slide. It may be introduced in the optical pathway to observe optical phenomena called interference figures, which are very useful when trying to discriminate between minerals.

h. Oculars

Oculars are lenses that magnify the image provided by the objective lens and focus the light so it can be accepted by the human eye.

Magnification in the used microscopes was 10x. The total magnification of the microscope is the magnification of the objective lens times the magnification of the oculars.

B.3 Strengths and limitations

The microscopic observation of rocks and textures remains one of the classic, and to this day indispensable, mineralogical methods of analysis. The greatest advantage of optical microscopy is that it provides a non-destructive way to identify crystalline or amorphous solid materials with relatively high spatial resolution allows an estimate of chemical compositions and is a first step to the history of formation of rocks. The limitations of optical microscopy are that chemical composition of complex solutions is impossible to make, as well as the identification of minerals too fine-grained to be identified (which is the case of zeolites and clay minerals) (modified from Raith *et al.*, 2012).

APPENDIX C: FUNDAMENTALS OF SCANNING ELECTRON MICROSCOPY WITH ENERGY DISPERSIVE MICROSCOPY

C.1 Basic concepts

The Scanning Electron Microscopy (SEM) uses a high-energy electron beam to generate a variety of signals on the surface of solid samples. The signals derived from the interaction between the electron beam and the sample reveal information such as external morphology (texture), chemical composition and crystalline structure, and orientation of the studied material. In most of its applications, the data are collected over a selected area of the sample, and a 2D image can be generated to show changes in textural, chemical or preferred orientation of the sample. The magnification usually ranges between 20X-30,000X, with a spatial resolution between 50-100 nm. The SEM is also capable of doing punctual chemical analyses when it is equipped with an Energy Dispersive Spectrometer (SEM-EDX) (modified from Swapp, 2015).

The basic geometry of a SEM consists of an electron source, called “gun”; a series of electromagnetic lenses that focuses and accelerate the generated electrons; a vacuum chamber in a mobile stage, which prevents the interference between the electron beam and molecules of gas an vapor; and finally, detectors such as EDX for elemental chemical analysis.

C.2 Strengths and limitations

The greatest strengths of the SEM are they are relatively easy to operate, and once the thin sections are prepared, sample preparation is minimal.

Data acquisition is rapid (<5 minutes per image or spot analyses). Between the limitations of the SEM, samples must be stable at vacuum conditions (10^{-6}-10^{-5} torr). Also, EDX detectors have problems detecting light elements with atomic numbers < 11 (Na).

APPENDIX D: FUNDAMENTALS OF X-RAY POWDER DIFFRACTION

D.1 X-ray powder diffraction

The physico-chemical properties of minerals indicate that they consist of a regular repetition of atoms arrays. X-rays can be used to study samples with zeolites or clays, too little to observe in the hand sample or the petrographic microscope, and which turned out to be the case of the samples in this study. The interaction of X-rays with the crystalline structure of minerals results in the diffraction of X-rays at an angle θ, produced on a crystal face with interatomic spacing d. The equation is known as Bragg's law, and states as following (Nesse, 2000):

$$n\lambda = 2d\sin(\theta) \quad \text{(B.1)}$$

Where n is an integer number reflecting that scattered wavefronts are in phase, and λ is the wavelength of the incident beams. According to Bragg's law, each mineral has a unique set of known d-spacings that produce maximum diffraction. In this manner, matching the d-spacings of an unknown mineral to an standard provides the means to identify the phases present in the sample.

The instrument used in XRD analyses is called diffractometer, where the intensity of diffracted X-rays is recorded as the sample and detector rotate through certain angles θ. A peak in intensity occurs when the mineral contains lattice planes with d-spacings appropriate to diffract X-rays at that value of θ. The peaks are recorded in a graph known as diffractogram, the final product used to mineral identification. The detailed explanation of the performance of an X-

Ray diffractometer and the physical fundaments of this technique are explained in Appendix B.

In the next sections sample preparation and data acquisition, and the interpretation of the obtained diffractograms data will discussed.

A diffractometer is composed of: (i) an X-Ray tube, where the X-Rays are generated; (ii) a sample holder, where the X-Rays interact with the sample; (iii) a detector, where the response of the previous interaction is recorded; and (iv) a goniometer under the sample holder, that orientates the sample in a favorable direction for the analysis, as it will be discussed later. The next sections explain the theoretical fundaments on the functioning of the X-Ray Diffractometer based on (Nesse, 2000).

a. **Generation of X-Rays**

The X-Rays are part of the electromagnetic field, and have interatomic-scale wavelengths that range between 0.1-10 Å. In a conventional diffractometer, the X-Rays are generated in an X-Ray Tube, which is made out of a filament, an objective and a filter window. The filament, also named cathode, generates the electron due to a temperature rise. These free electrons are dramatically accelerated at high voltage (*ca.* 20-100 kV) towards the objective. Due to the interaction between the electron and the objectives, two types of X-Rays are generated: characteristic and continuus-spectrum X-Rays. The objective is basically a conductive layer, usually made of Mo, Fe or Cr. When the electrons produced in the filament impact the objective, a change in the

electron configuration of the objective's atoms can be produced. When the electron configuration is not affected by the incidence of the electron beam, continuus-sprectum X-Rays are produced; in turn, when a change in the electron configuration is achieved, characteristic X-Rays are produced. The continuus-spectrum X-Rays are produced when the incident electron beam is unable to release electron from the objective. This is translated as a slowdown in the electrons of the objective, so the energy they contained is released as electromagnetic radiations in different wavelengths and significant amounts of heat. The characteristic spectrum is produced when the high-energy electrons dislocate any electron in the first atomic level (n=1 or level K). Almost instantly, an external electron (e.g. n=2 or level L; n=3 or level M) jumps right into the position that the previous electron used, emitting X-Rays of characteristic wavelength. The wavelength λ (in angstroms) is related to the difference in the energy of the atomic level ΔE through the equation:

$$\lambda = hc = 12.4\ \Delta E \qquad \text{(B.2)}$$

Where c is the speed of light, and h is the Planck's constant. Most of the electrons fall from the level L or M, producing characteristic wavelengths, denominated Kα y Kβ respectively. Naturally, ΔE in the case of the L-K jump is less than the M-K jump, which translates in a greater Kα than Kβ. Table B-1 summarizes the different wavelengths according to the material of the objective and the electron jump.

Table B-1. Wavelengths corresponding to the material of the X-Ray diffractometer objective.

Wavelength (Å)/Material	Mo	Cu	Fe	Cr
Kβ	0.63225	1.38217	1.75653	2.084479
Kα	0.71070	1.54180	1.93730	2.29090

Finally, the success of the X-Ray diffraction analysis requires that the used characteristic wavelength remains constant. In other words, monochromatic X-Rays must be used. The way this is achieved is through the installation of a filter –known as window–at the exit end of the X-Ray tube.

b. **Interaction between the X-Rays and the sample**

The monochromatic wavelength used in X-Ray diffraction is a value near to 1-2 Å, similar to the interatomic spacing. The similarity in the dimensions of the wavelength and the atomic structure is the reason why the X-Rays are diffracted by the regularly distributed atoms of a crystal. It can be demonstrated that in 3D arrays maximum diffraction is produced in a certain angle θ, similar to the reflection angle. Consider the incident rays shown in Figure B-1, at an angle θ of the

crystal face with interatomic spacing *d*. The equation that relates these parameters is the following:

$$n\lambda = 2d\sin(\theta) \quad \text{(B.3)}$$

Where n is an integer number that represents that the scattered wavefronts are in phase and λ is the wavelength of the incident beams. The reflection of the X-Rays is the result of the diffraction within the crystalline structure, and it's only possible if the mineral grain is properly oriented. For an unknown mineral with interatomic spacing d it is extremely difficult to have it properly oriented for diffraction; furthermore, one single mineral has more than one interatomic spacing d. To solve these problems, one of the most common preparations for X-Ray diffraction can be used (for more information, see section 2.2), and the detector (where the data are collected) as well as the sample are rotated.

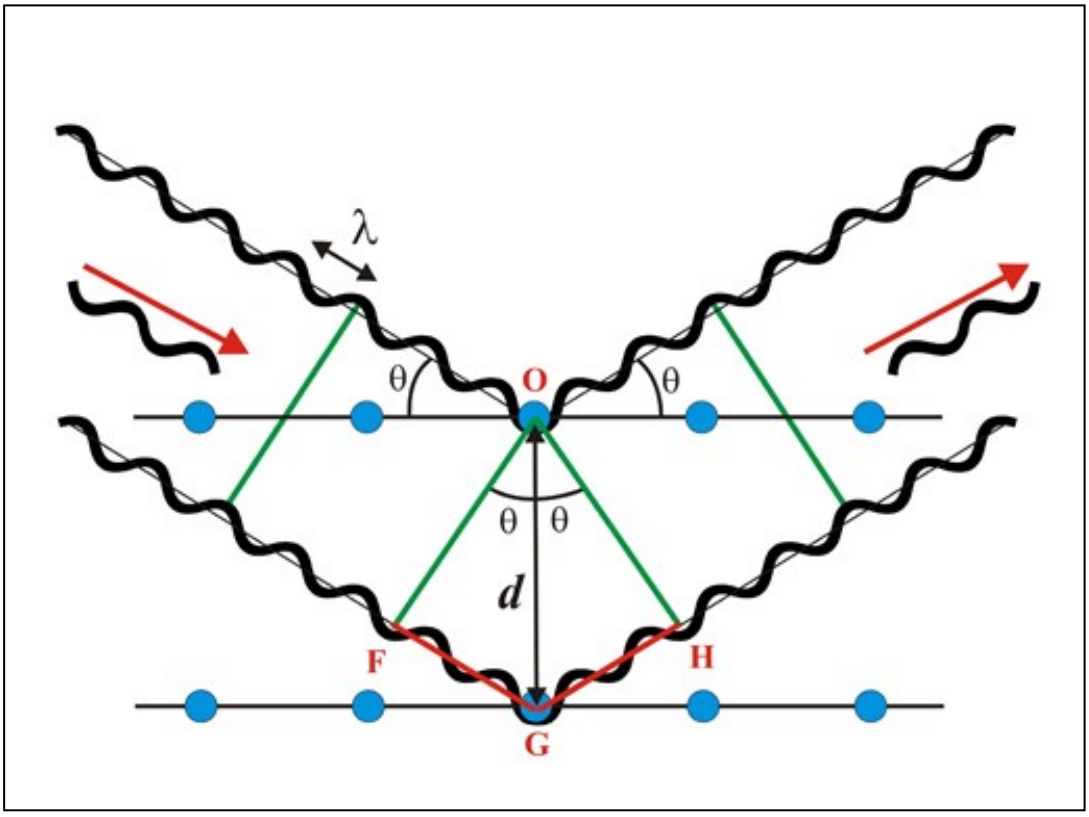

Figure B-1. Illustration of the Bragg's law. Two beams with identical wavelength and phase are scattered off two atoms within it. Constructive interference occurs when the path difference is equal to an integer number.

c. **Detector, goniometer and data acquisition**

For standard mineral identification using CuKα radiation, the detector is rotated from an angle 2θ varying from 5° until 70°, which allows a very complete range of interatomic spacings *d* to be identified (between 17.7 y 1.34 Å). In turn, the sample is rotated at an angle θ, and the intensity of received diffracted rays is recorded in a computer. The most common result of an X-Ray analysis is a graph known as *diffractogram,* which registers the different peaks (measured in relative intensity/second) as a function of the 2θ angle of the detector (Figure

B-2). A peak in X-Rays intensity means that the studied mineral has interatomic spacings *d* optimal to reflect in a certain angle θ, following the Bragg's law.

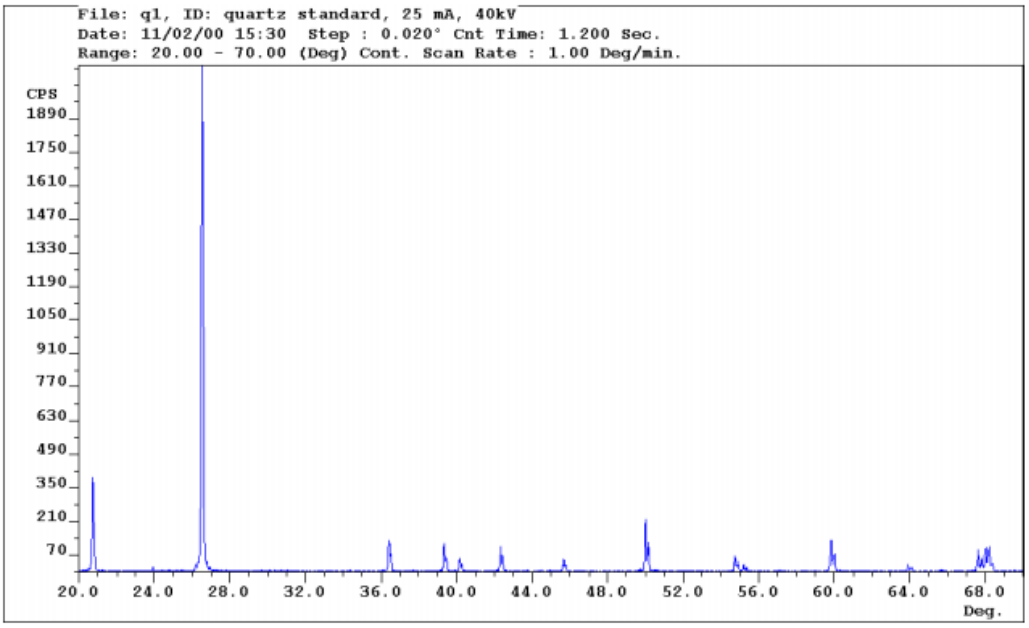

Figure B-2. Standard diffractogram of quartz (extracted from Smyth, 2015).

In this manner, each mineral has a unique set of peaks at specific angles of diffraction. When the diffractogram of a sample is obtained, the routine procedure for mineral identification consists on comparing such diffractogram with a standard (usually obtained from the International Centre for Diffraction Data, in its compilation named Powder Diffraction Data).

D.2 Strengths and limitations

Between the most remarkable strengths of X-Ray powder Diffraction there is the fact that diffractograms are relatively easy to obtain (<15-20 minutes), and in most cases it provides unambiguous mineral identification. Also, minimal sample preparation is required, and diffractometers are widely available. The limitations of this method is that homogeneous and single phase materials are better identified, requires tenths of gram the material to be studied, and for mixed minerals the limit of detection is nearly ~5% of the sample. Also, peak overlay can occur, difficulting the diffractogram interpretation.

APPENDIX E: FUNDAMENTALS OF GEOELECTRICAL MEASUREMENTS (MODIFIED FROM LOWRIE, 2007 AND REFERENCES THEREIN)

E.1 Geoelectrical measurements of the subsurface

Geoelectrical surveys are utilized for a wide variety of applications. For example, their application ranges from commercial use in the search of ore-bodies to scientific investigation in the exploration of the internal structure of the Earth.

Usually, electrical methods involve the detection of signals by the induction of electric and magnetic fields in the subsurface. Such methods require potential differences to be measured between implanted electrodes. For each measure, four collinear electrodes are utilized: two of them are used to supply a known and controlled current *I*; and the other two are used to measure the difference of potential differences *V*, produced by such induced current. With these parameters, resolving the Ohm's law and the Maxwell's equations, the unknown resistivity ρ is obtained with the following expression (Telford *et al.*, 1990):

$$\rho = 2\pi V I^{-1} G^{-1} \qquad \text{(E.1)}$$

Where *G* is known as geometrical factor, used to correct the relative distance between the points of current injection and voltage measurement and depends on the distance of the utilized configuration of electrode (Figure F-1).

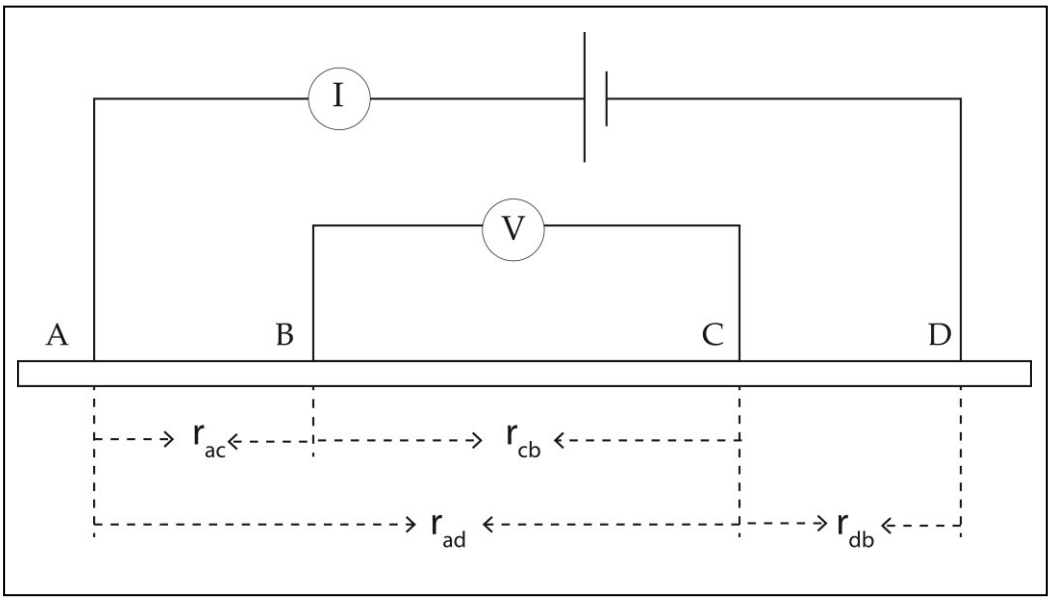

Figure F-1. General four-electrode configuration for resistivity measurement, consisting of a pair of current electrodes (A,B) and a pair of potential electrodes (C,D) (modified from Lowrie, 2007)

In any collinear four-electrode configuration the geometrical factor *G* is equal to:

$$G= (1/r_{AC}-1/r_{CB})- (1/r_{AD}-1/r_{DB}) \quad \text{(E.2)}$$

And r_{AC}, r_{CB}, r_{AD} and r_{DB} are the dipolar distances in Figure F-1. In this study, the dipole-dipole and Schlumberger configurations were used. In the Schlumberger configuration (Figure E-2a) the current and potential pairs of electrodes have a common mid-point, but the distances between adjacent electrodes differ. Let the separations of the current and potential electrodes be L and a, respectively. Substituting in the general formula, the geometrical factor G is:

$$G = a/(L^2-a^2) \quad \text{(E.3)}$$

In the double-dipole configuration (Figure E-2b) the spacing of the electrodes in each pair is a, while the distance between their mid-points is L, which is generally much larger than a. In this configuration, the geometrical factor is:

$$G = a^2/L(L^2-a^2) \quad \text{(E.4)}$$

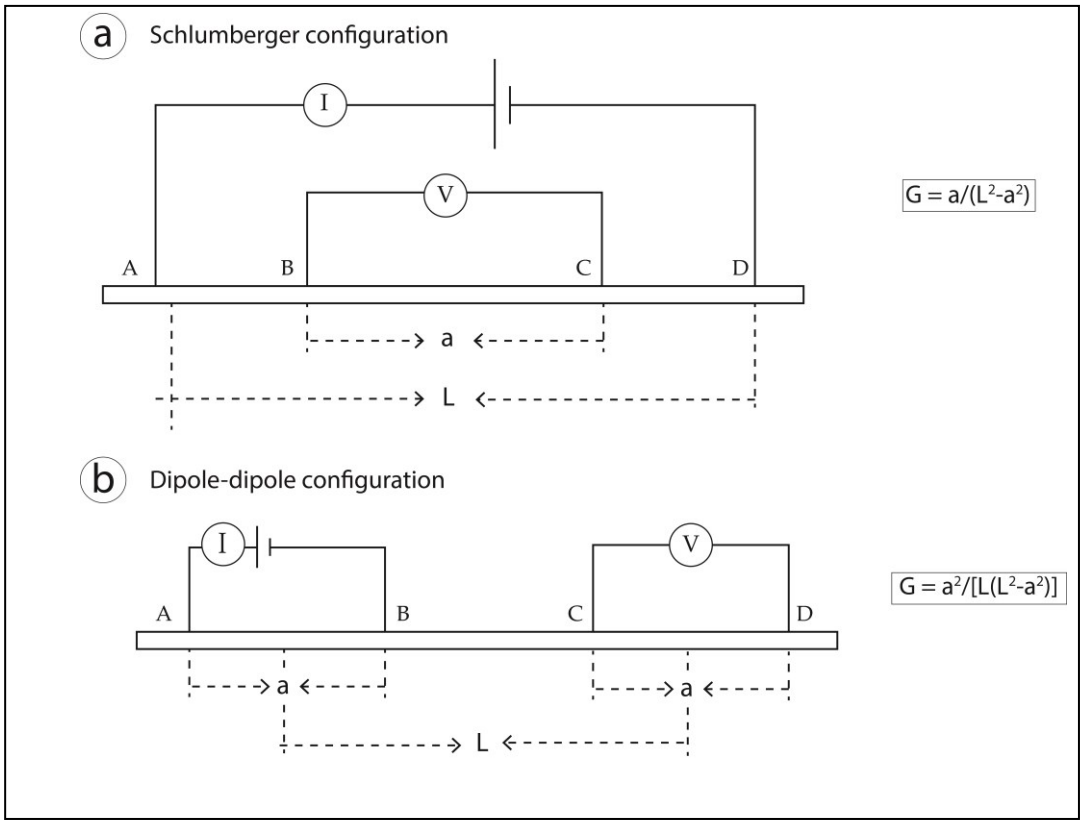

Figure E-2. Geometries of current and potential electrodes used in this study for (a) Schlumberger and (b) dipole-dipole configurations.

Once the electrodes are installed, the resistivity data acquisition can be completely controlled by a software that determines a 2D apparent

resistivity map of the subsurface. It is classically assumed that a linear array of electrodes delivers an apparent resistivity section that is perpendicular to the surface of installation and parallel to such linear array (e.g. Caputo *et al.*, 2007). The critical factor in the measured resistivity in shallow rocks is water content, followed by the concentration of dissolved ions, the prevalent mineralogy and the temperature (Grant and West, 1965, Revil *et al.*, 1998, Zohdy *et al.*, 1974). Electrical anomalies arise when resistivity contrasts are present in the studied zone.

E.2 Strengths and limitations

Between the most remarkable strengths of the 2D electrical survey is that data acquisition is fast (<1 hour per line). The utilized installation of electrodes in the rock produces an electrical response that certainly corresponds to the studied fault zones, whereas the installation of electrodes in the ground could produce a response that corresponds to the first soil strata and/or the studied fault zone. The used equipment 2D electrical survey (5m of maximum dipolar distance) provides an upper limit for the maximum penetration depth and the spatial resolution in a single electrical line (with a maximum penetration of *ca.* 75-100m, maximum spatial resolution of 2-5m), which could be a disadvantage in large-scale studies.

APPENDIX F: STRUCTURAL RESULTS

A complete dataset of the studied structural elements is provided in this appendix. Results from the LOFS exposure are summarized in Table F-1 and results from the ALFS exposure are summarized in Table F-2. Maps with preliminary structural classifications at a 1:50 scale are included (LOFS splay fault = Figures F-1 and F-2; ALFS segment = Figures F-3 and F-4).

Table F-1. Summarized results of the structural mapping of the LOFS splay fault.

ID	Geographical coordinates [PSAD56-UTM]		Geometrical attitude [RHR]			Structural element	Kinematics	Kinematic indicator
	N	E	Strike	Dip	Rake			
1	5733801.110	280574.558	74	84	n/a	Vein	n/a	n/a
2	5733801.409	280574.308	68	87	n/a	Vein	n/a	n/a
3	5733801.516	280574.218	104	75	n/a	Hydrothermal breccia	n/a	n/a
4	5733802.565	280573.337	35	52	n/a	Hydrothermal breccia	n/a	n/a
5	5733802.795	280573.144	264	80	n/a	Hydrothermal breccia	n/a	n/a
6	5733803.139	280572.855	7	76	n/a	Hydrothermal breccia	n/a	n/a
7	5733803.025	280572.952	10	66	12	Fault	Dextral-reverse	Steps + lunettes
8	5733802.795	280573.144	39	74	37	Fault	Dextral-reverse	Steps
9	5733803.254	280572.759	195	81	n/a	Hydrothermal breccia	n/a	n/a
10	5733803.407	280572.630	0	86	n/a	Hydrothermal breccia	n/a	n/a
11	5733803.944	280572.181	64	78	n/a	Hydrothermal breccia	n/a	n/a
12	5733804.020	280572.116	224	81	152	Fault-vein	Dextral-reverse	Quartz mineral fibers

ID	Geographical coordinates [PSAD56-UTM]		Geometrical attitude [RHR]			Structural element	Kinematics	Kinematic indicator
	N	E	Strike	Dip	Rake			
13	5733804.035	280572.103	58	54	n/a	Hydrothermal breccia	n/a	n/a
14	5733804.173	280571.988	74	84	18	Fault-vein	Dextral	Quartz +calcite mineral fibers
15	5733804.173	280571.988	60	87	20	Fault-vein	Dextral	Quartz mineral fibers
16	5733804.173	280571.988	50	85	25	Fault-vein	Dextral	Quartz + calcite mineral fibers
17	5733804.135	280572.020	206	86	n/a	Hydrothermal breccia	n/a	n/a
18	5733804.326	280571.859	86	76	32	Fault-vein	Dextral	Quartz mineral fibers
19	5733804.403	280571.795	143	83	21	Fault-vein	Dextral	Quartz mineral fibers
20	5733806.854	280569.739	62	85	n/a	Vein	n/a	n/a
21	5733807.083	280569.546	57	84	n/a	Vein	n/a	n/a
22	5733807.543	280569.160	65	88	n/a	Vein	n/a	n/a
23	5733808.845	280568.068	95	70	n/a	Vein	n/a	n/a
24	5733808.959	280567.971	60	73	n/a	Vein	n/a	n/a
25	5733809.304	280567.682	100	80	n/a	Hydrothermal breccia	n/a	n/a
26	5733809.610	280567.425	71	87	n/a	Hydrothermal breccia	n/a	n/a
27	5733809.725	280567.329	106	89	n/a	Vein	n/a	n/a
28	5733809.993	280567.104	71	76	n/a	Hydrothermal breccia	n/a	n/a
29	5733810.070	280567.040	82	88	n/a	Hydrothermal breccia	n/a	n/a
30	5733811.265	280566.037	248	77	140	Fault	Dexttral	Steps
31	5733811.333	280565.979	165	80	142	Fault	Sinistral-normal	Steps
32	5733811.410	280565.915	198	25	n/a	Vein	n/a	n/a
33	5733811.372	280565.947	24	23	n/a	Vein	n/a	n/a
34	5733811.640	280565.722	24	9	n/a	Vein	n/a	n/a
35	5733813.210	280564.405	66	81	n/a	Hydrothermal breccia	n/a	n/a

ID	Geographical coordinates [PSAD56-UTM]		Geometrical attitude [RHR]			Structural element	Kinematics	Kinematic indicator
	N	E	Strike	Dip	Rake			
36	5733814.052	280563.698	225	69	n/a	Hydrothermal breccia	n/a	n/a
37	5733814.129	280563.634	237	84	n/a	Hydrothermal breccia	n/a	n/a
38	5733814.358	280563.441	40	87	n/a	Hydrothermal breccia	n/a	n/a
39	5733819.528	280559.104	246	87	125	Fault	Dextral	Steps + lunettes

Table F-2. Summarized results of the structural mapping of the ALFS segment.

ID	Geographical coordinates [PSAD56-UTM]		Geometrical attitude [RHR]			Structural element	Kinematics	Kinematic indicator
	N	E	Strike	Dip	Rake			
1	5730618.00	287871.00	296	66	n/a	Fault-localized hydrothermal breccia	n/a	n/a
2	5730617.86	287870.86	119	72	n/a	Fault-localized hydrothermal breccia	n/a	n/a
3	5730617.86	287870.86	40	45	n/a	Fault-localized hydrothermal breccia	n/a	n/a
4	5730617.65	287870.65	274	60	17	Fault-vein	Dextral	Quartz mineral fibers
5	5730617.50	287870.50	109	72	167	Fault-localized hydrothermal breccia	n/a	n/a
6	5730617.29	287870.29	132	73	n/a	Fault-localized hydrothermal breccia	n/a	n/a

ID	Geographical coordinates [PSAD56-UTM]		Geometrical attitude [RHR]			Structural element	Kinematics	Kinematic indicator
	N	E	Strike	Dip	Rake			
7	5730616.94	287869.94	103	63	n/a	Fault-localized hydrothermal breccia	n/a	n/a
8	5730616.44	287869.44	170	75	n/a	Fault-localized hydrothermal breccia	n/a	n/a
9	5730615.91	287868.91	297	81	159	Fault-localized hydrothermal breccia	n/a	n/a
10	5730615.59	287868.59	100	41	n/a	Fault-localized hydrothermal breccia	n/a	n/a
11	5730615.17	287868.17	6	52	n/a	Fault-localized hydrothermal breccia	n/a	n/a
12	5730613.93	287866.93	130	76	n/a	Fault-localized hydrothermal breccia	n/a	n/a
13	5730613.36	287866.36	153	59	n/a	Fault-localized hydrothermal breccia	n/a	n/a
14	5730613.54	287866.54	135	69	n/a	Fault-localized hydrothermal breccia	n/a	n/a
15	5730612.98	287865.98	312	55	n/a	Fault-localized hydrothermal breccia	n/a	n/a
16	5730612.91	287865.91	180	71	n/a	Fault-localized hydrothermal breccia	n/a	n/a

ID	Geographical coordinates [PSAD56-UTM]		Geometrical attitude [RHR]			Structural element	Kinematics	Kinematic indicator
	N	E	Strike	Dip	Rake			
17	5730612.69	287865.69	162	74	n/a	Fault-localized hydrothermal breccia	n/a	n/a
18	5730612.69	287865.69	156	76	n/a	Fault-localized hydrothermal breccia	n/a	n/a
19	5730612.37	287865.37	135	85	n/a	Fault-localized hydrothermal breccia	n/a	n/a
20	5730611.77	287864.77	296	87	n/a	Fault-localized hydrothermal breccia	n/a	n/a
21	5730611.77	287864.77	183	85	n/a	Fault-localized hydrothermal breccia	n/a	n/a
22	5730611.14	287864.14	295	73	n/a	Hydrothermal breccia	n/a	n/a
23	5730611.14	287864.14	60	42	n/a	Fault-localized hydrothermal breccia	n/a	n/a
24	5730610.85	287863.85	95	87	n/a	Fault-localized hydrothermal breccia	n/a	n/a
25	5730610.75	287863.75	308	74	n/a	Fault-localized hydrothermal breccia	n/a	n/a
26	5730609.90	287862.90	342	81	n/a	Fault-localized hydrothermal breccia	n/a	n/a
27	5730609.71	287862.71	114	80	n/a	Fault-localized hydrothermal breccia	n/a	n/a

ID	Geographical coordinates [PSAD56-UTM]		Geometrical attitude [RHR]			Structural element	Kinematics	Kinematic indicator
	N	E	Strike	Dip	Rake			
28	5730609.26	287862.26	117	80	n/a	Hydrothermal breccia	n/a	n/a
29	5730609.16	287862.16	125	74	n/a	Hydrothermal breccia	n/a	n/a
30	5730609.16	287862.16	96	65	n/a	Hydrothermal breccia	n/a	n/a
31	5730609.37	287862.37	228	40	n/a	Fault-localized hydrothermal breccia	n/a	n/a
32	5730608.92	287861.92	304	70	n/a	Fault-localized hydrothermal breccia	n/a	n/a
33	5730608.02	287861.02	325	75	n/a	Fault-localized hydrothermal breccia	n/a	n/a
34	5730608.62	287861.62	300	60	n/a	Fault-localized hydrothermal breccia	n/a	n/a
35	5730607.65	287860.65	110	73	n/a	Fault-localized hydrothermal breccia	n/a	n/a
36	5730607.56	287860.56	320	66	n/a	Fault-localized hydrothermal breccia	n/a	n/a
37	5730607.02	287860.02	320	82	170	Fault-vein	Sinistral	Quartz + calcite mineral fibers
38	5730606.61	287859.61	175	84	10	Fault-vein	Sinistral	Quartz mineral fibers
39	5730605.94	287858.94	135	76	n/a	Fault-localized hydrothermal breccia	n/a	n/a

ID	Geographical coordinates [PSAD56-UTM]		Geometrical attitude [RHR]			Structural element	Kinematics	Kinematic indicator
	N	E	Strike	Dip	Rake			
40	5730605.83	287858.83	143	76	n/a	Fault-localized hydrothermal breccia	n/a	n/a
41	5730605.72	287858.72	125	76	n/a	Fault-localized hydrothermal breccia	n/a	n/a
42	5730605.69	287858.69	356	82	n/a	Fault-localized hydrothermal breccia	n/a	n/a
43	5730605.65	287858.65	109	56	n/a	Fault-localized hydrothermal breccia	n/a	n/a
44	5730605.53	287858.53	330	77	n/a	Fault-localized hydrothermal breccia	n/a	n/a
45	5730605.45	287858.45	60	36	n/a	Fault-localized hydrothermal breccia	n/a	n/a
46	5730605.43	287858.43	328	82	n/a	Fault-localized hydrothermal breccia	n/a	n/a
47	5730605.12	287858.12	122	57	n/a	Fault-localized hydrothermal breccia	n/a	n/a
48	5730604.52	287857.52	120	76	n/a	Fault-localized hydrothermal breccia	n/a	n/a
49	5730604.38	287857.38	110	74	n/a	Fault-localized hydrothermal breccia	n/a	n/a

ID	Geographical coordinates [PSAD56-UTM]		Geometrical attitude [RHR]			Structural element	Kinematics	Kinematic indicator
	N	E	Strike	Dip	Rake			
50	5730604.13	287857.13	319	73	n/a	Fault-localized hydrothermal breccia	n/a	n/a
51	5730604.03	287857.03	150	72	n/a	Fault-localized hydrothermal breccia	n/a	n/a
52	5730606.47	287859.47	146	41	n/a	Fault-localized hydrothermal breccia	n/a	n/a
53	5730607.03	287860.03	122	66	n/a	Fault-localized hydrothermal breccia	n/a	n/a
54	5730603.00	287856.00	288	70	n/a	Fault-localized hydrothermal breccia	n/a	n/a
55	5730606.68	287859.68	148	89	12	Fault-vein	Sinistral	Quartz mineral fibers + steps
56	5730605.33	287858.33	148	46	n/a	Fault-localized hydrothermal breccia	n/a	n/a
57	5730610.07	287863.07	332	60	n/a	Fault-localized hydrothermal breccia	n/a	n/a
58	5730607.74	287860.74	118	50	n/a	Fault-localized hydrothermal breccia	n/a	n/a
59	5730606.11	287859.11	289	27	n/a	Fault-localized hydrothermal breccia	n/a	n/a

ID	Geographical coordinates [PSAD56-UTM]		Geometrical attitude [RHR]			Structural element	Kinematics	Kinematic indicator
	N	E	Strike	Dip	Rake			
60	5730605.97	287858.97	320	85	n/a	Fault-localized hydrothermal breccia	n/a	n/a
61	5730607.03	287860.03	132	28	unknown	Fault	Reverse	Cm-scale reverse separation
62	5730606.68	287859.68	138	26	unknown	Fault	Reverse	Cm-scale reverse separation

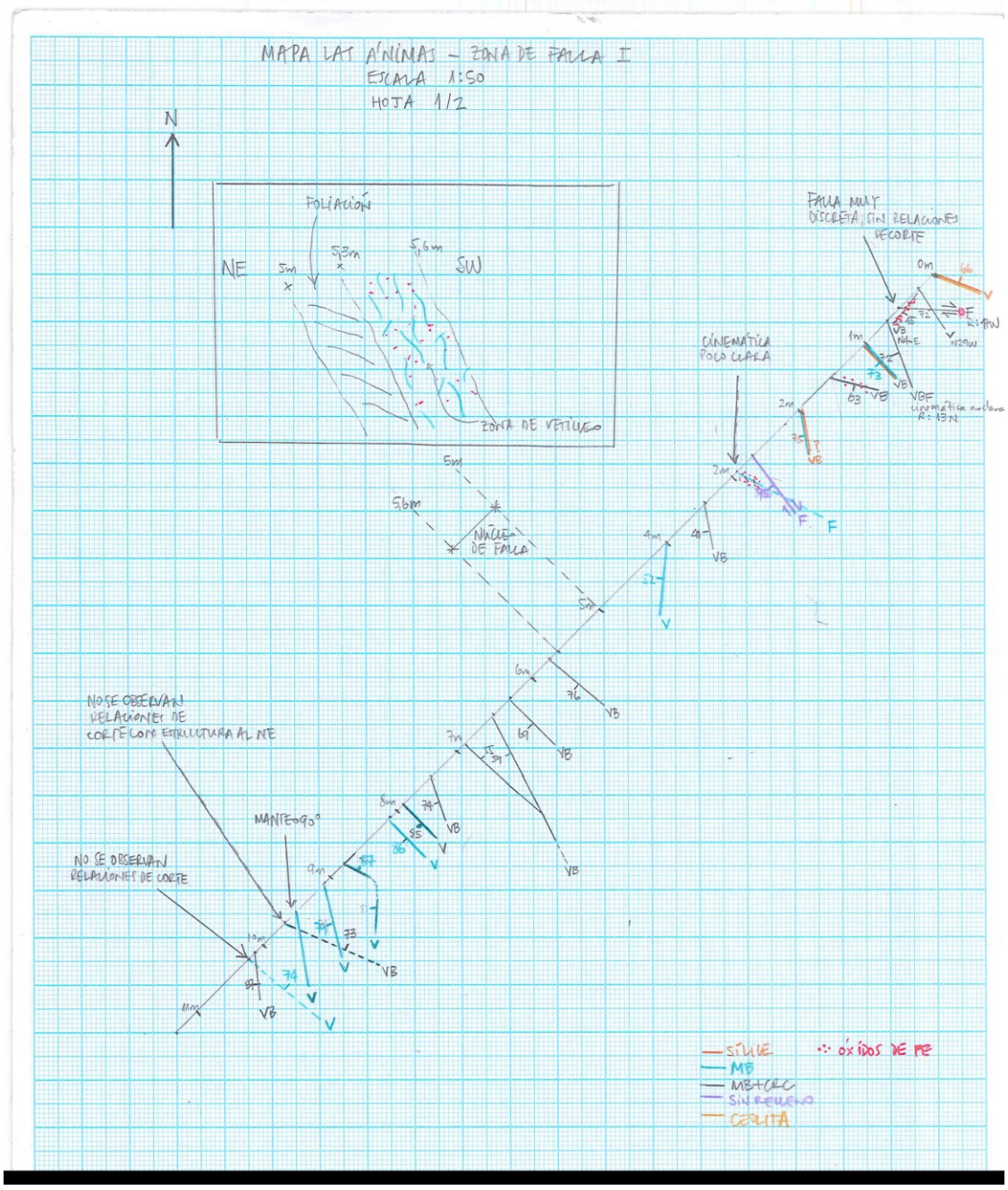

Figure F-1. LOFS splay fault map (1:50) with preliminary classification of structural elements (1/2).

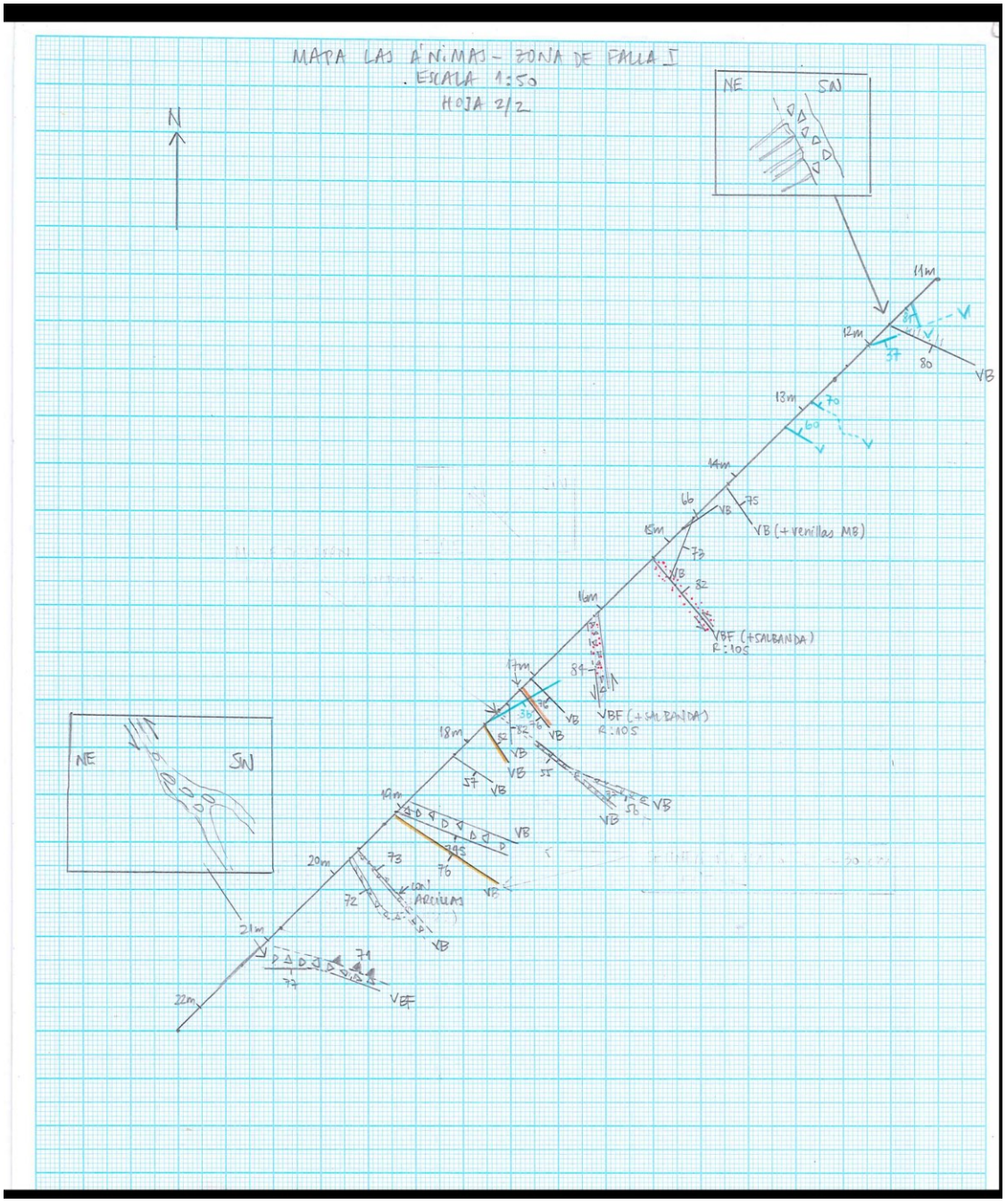

Figure F-2. LOFS splay fault map (1:50) with preliminary classification of structural elements (2/2).

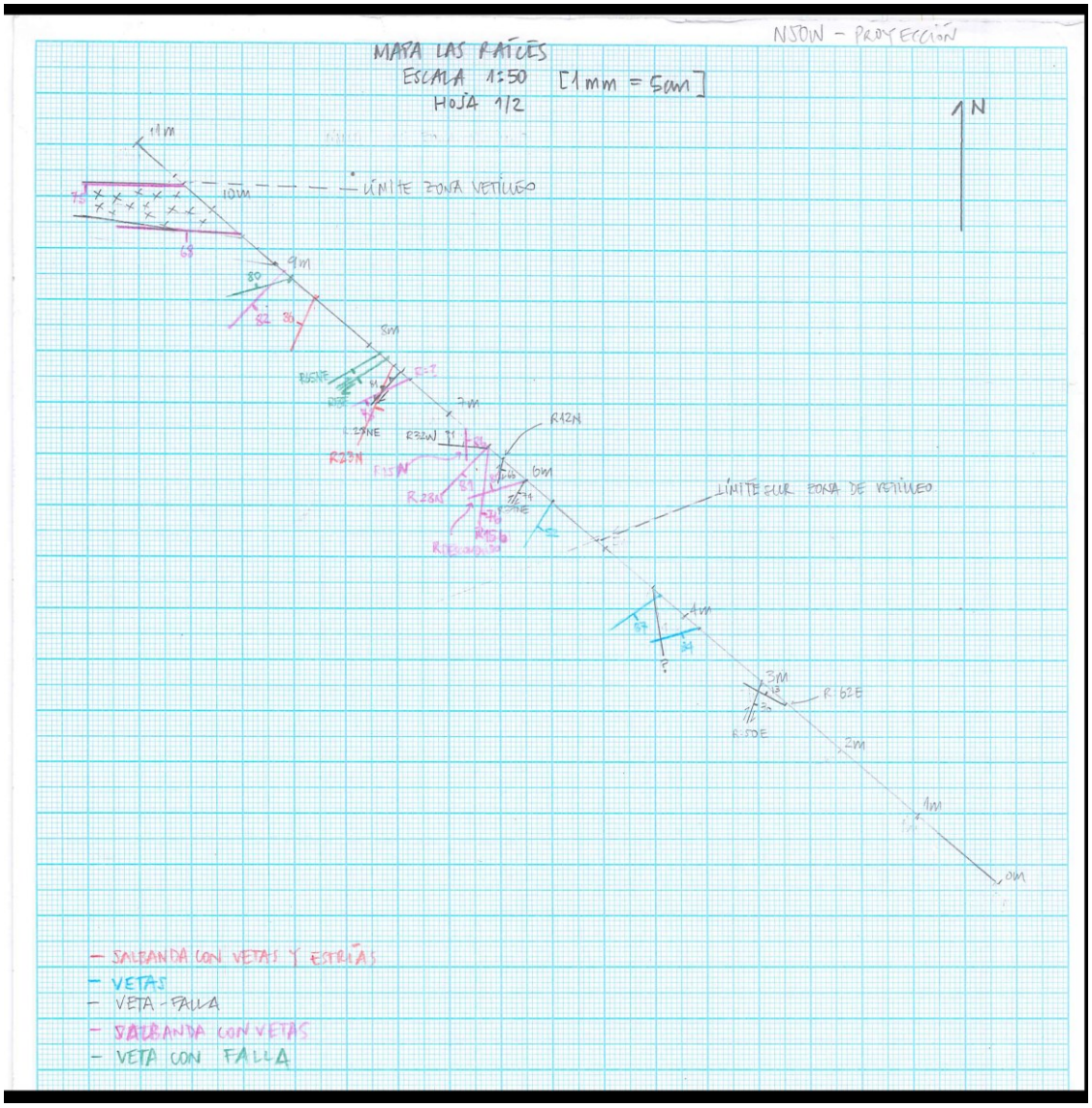

Figure F-3. ALFS segment map (1:50) with preliminary classification of structural elements (1/2).

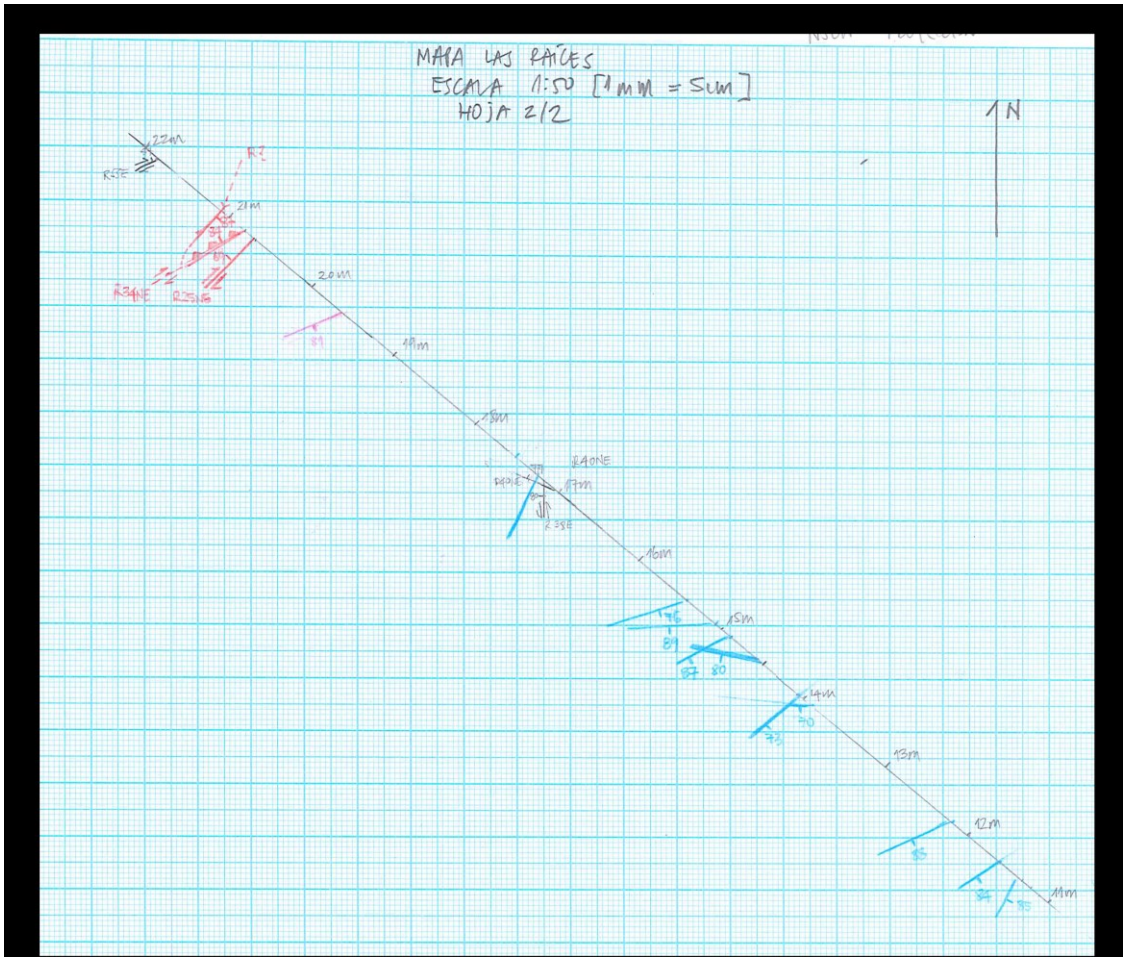

Figure F-4. ALFS segment map (1:50) with preliminary classification of structural elements (2/2).

APPENDIX G: ANALYZED DIFFRACTOGRAMS

A complete list of the analyzed diffractograms is provided in this appendix. Results from the LOFS exposure are summarized in Table G-1 and results from the ALFS exposure are summarized in Table G-2. A list of the interpreted diffractograms foe each outcrop follows the summary tables.

Table G-1. Summarized results of the interpreted diffractograms of the LOFS splay fault.

Sample	Geographical coordinates [PSAD56-UTM]		Mineralogy
	N	E	
LR3.8	5733801.147	280574.567	Laumontite; Quartz
LR4.19	5733801.446	280574.317	Laumontite; Stilbite; Quartz
LR4.33	5733801.553	280574.227	Quartz; Laumontite
LR5.1	5733802.143	280573.732	Laumontite; Montmorillonite
LR5.7	5733802.602	280573.346	Laumontite
LR6.8	5733803.445	280572.639	Stilbite; Laumontite
LR6.25	5733803.024	280572.993	Quartz; Laumontite
LR6.45	5733803.177	280572.864	Laumontite; Quartz
LR7.5	5733803.981	280572.189	Stilbite; Laumontite
LR7.6	5733804.058	280572.125	Laumontite; Hematite
LR7.62	5733804.073	280572.112	Stilbite; Laumontite; Chabacite
LR8.2	5733804.518	280571.739	Laumontite; Quartz
LR8.4	5733804.671	280571.611	Laumontite; Stilbite
LR8.6	5733804.824	280571.482	Quartz; Laumontite
LR8	5733804.364	280571.868	Quartz; Hematite
LR9.1	5733805.207	280571.161	Laumontite; Quartz
LR9.6	5733805.590	280570.839	Calcite; Laumontite
LR10.4	5733806.203	280570.325	Calcite; Stilbite
LR13.9	5733808.884	280568.075	Laumontite
LR14.5	5733809.344	280567.690	Laumontite
LR14.9	5733809.650	280567.432	Calcite; Stilbite
LR15.05	5733809.765	280567.336	Calcite; Quartz; Stilbite
LR19.6	5733813.250	280564.411	Calcite; Quartz
LR19.7	5733813.400	280564.500	Calcite; Stilbite

Sample	Geographical coordinates [PSAD56-UTM]		Mineralogy
	N	E	
LR20.8	5733814.170	280563.640	Calcite; Stilbite; Quartz

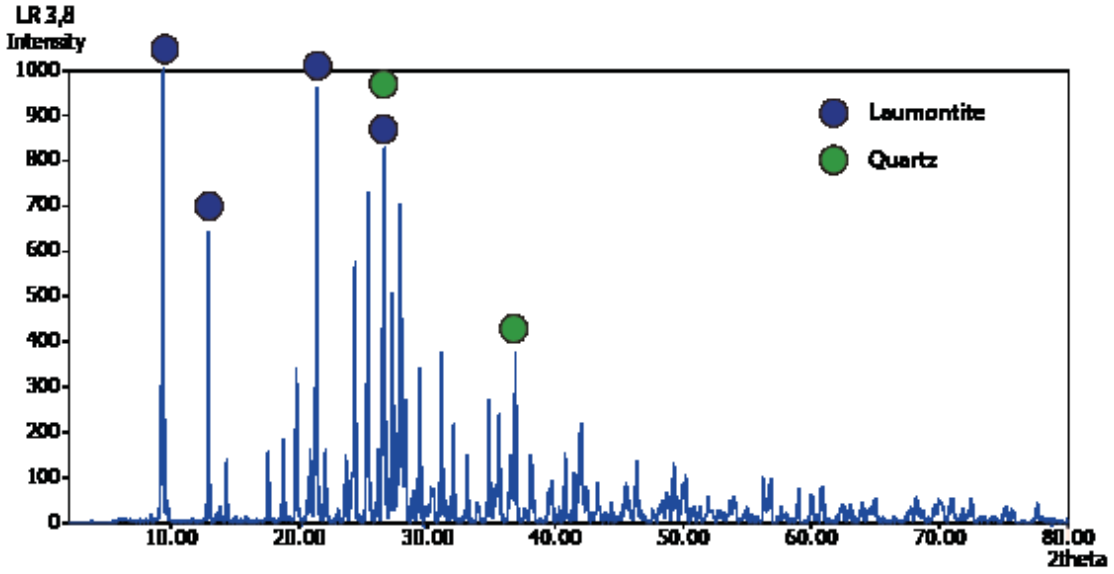

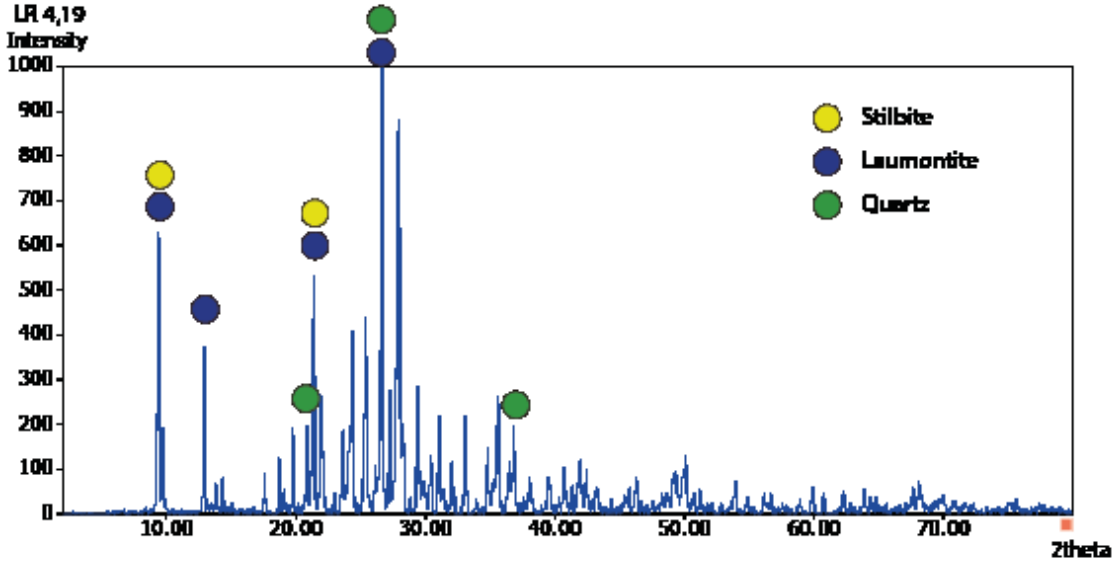

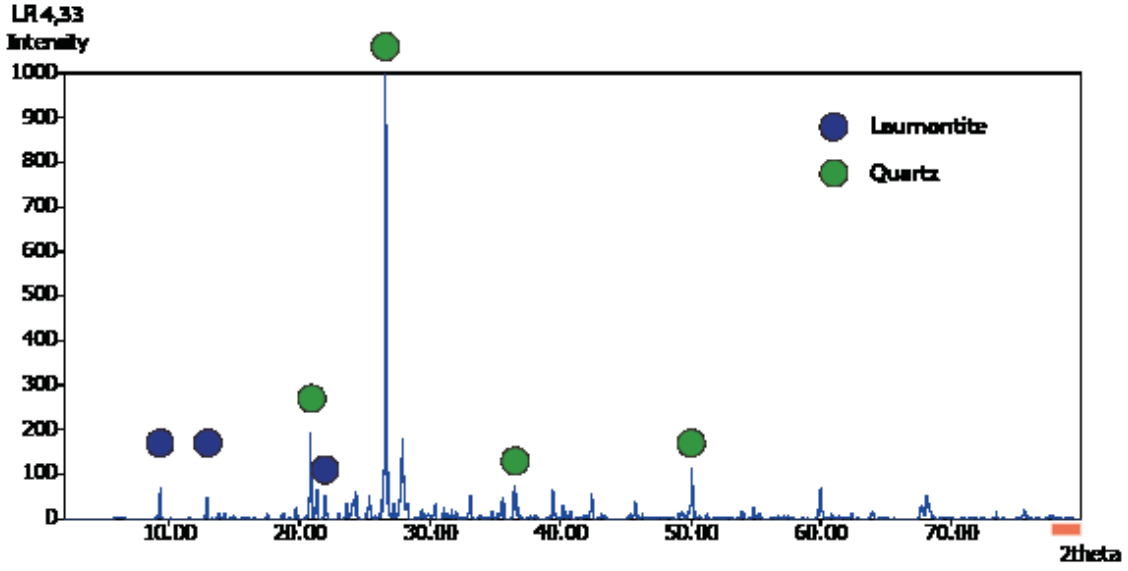
LR4,33
Intensity
1000
900
800
700
600
500
400
300
200
100
0
10.00
20.00
30.00
40.00
50.00
60.00
70.00
2theta
Laumontite
Quartz

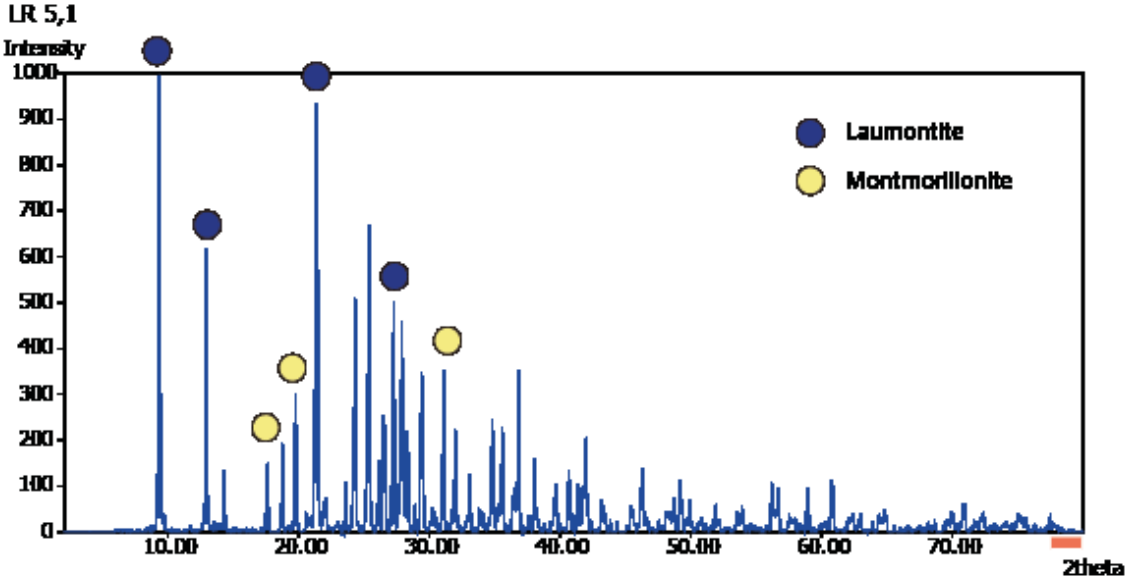
LR 5,1
Intensity
1000
900
800
700
600
500
400
300
200
100
0
10.00
20.00
30.00
40.00
50.00
60.00
70.00
2theta
Laumontite
Montmorillonite

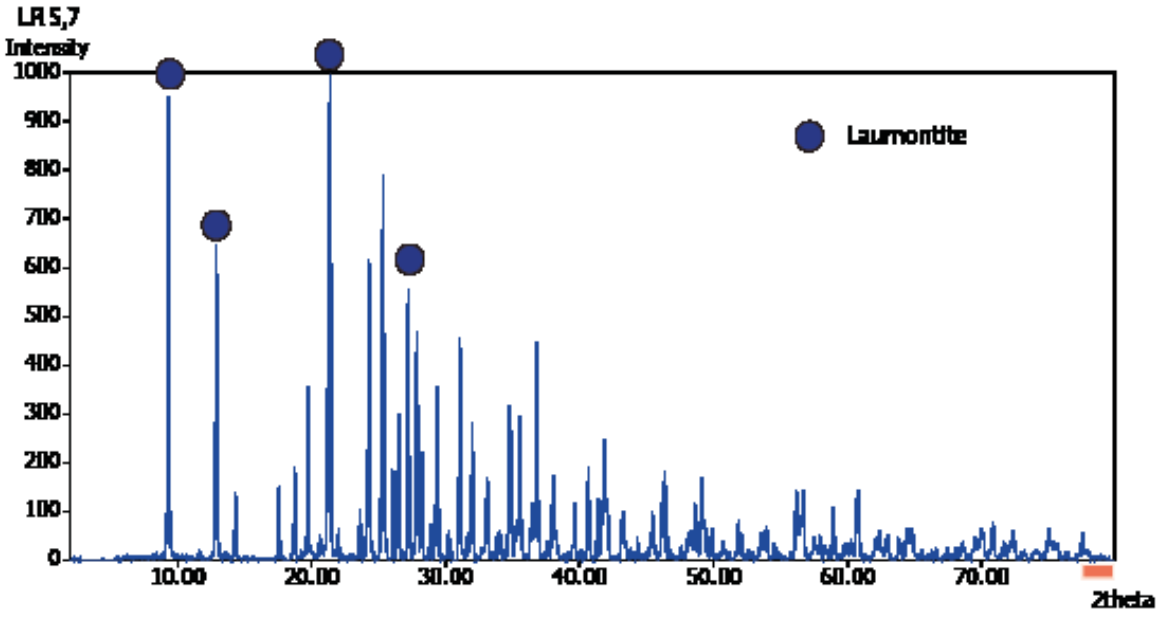
LR 5,7
Intensity
1000
900
800
700
600
500
400
300
200
100
0
10.00
20.00
30.00
40.00
50.00
60.00
70.00
2theta
Laumontite

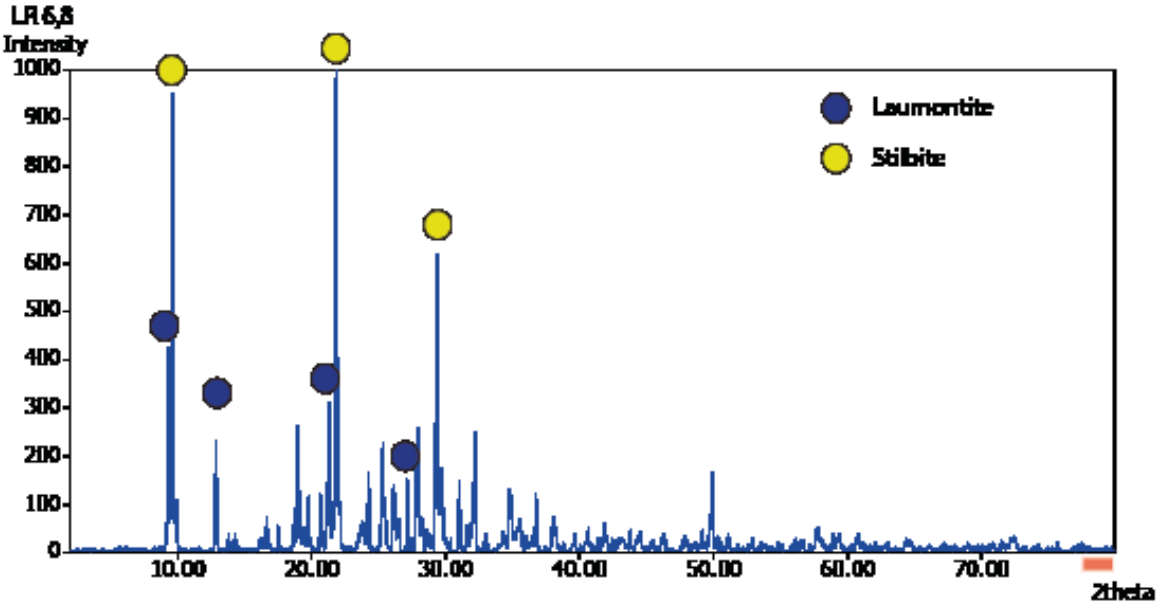
LR 6,8
Intensity
1000
900
800
700
600
500
400
300
200
100
0
10.00
20.00
30.00
40.00
50.00
60.00
70.00
2theta
Laumontite
Stilbite

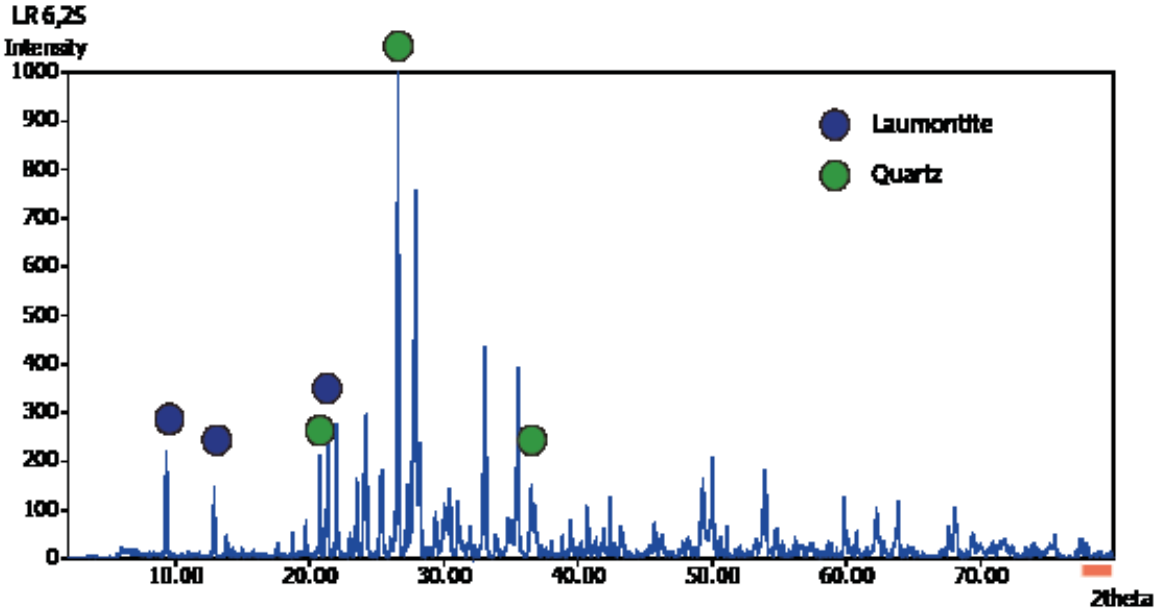
LR 6,25
Intensity
1000
900
800
700
600
500
400
300
200
100
0
10.00
20.00
30.00
40.00
50.00
60.00
70.00
2theta
Laumontite
Quartz

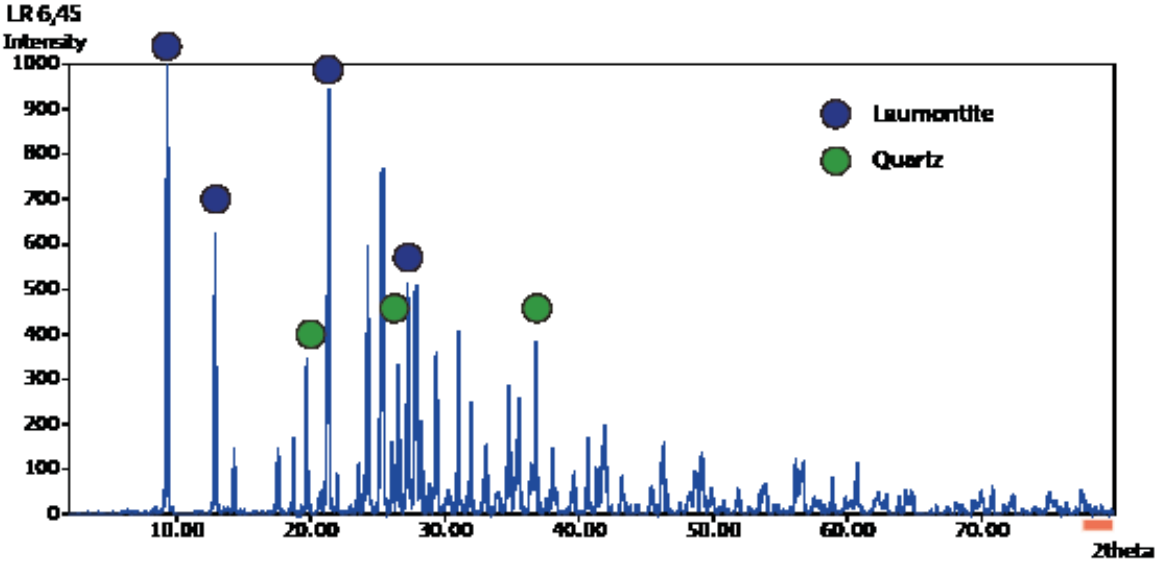
LR 6,45
Intensity
1000
900
800
700
600
500
400
300
200
100
0
10.00
20.00
30.00
40.00
50.00
60.00
70.00
2theta
Laumontite
Quartz

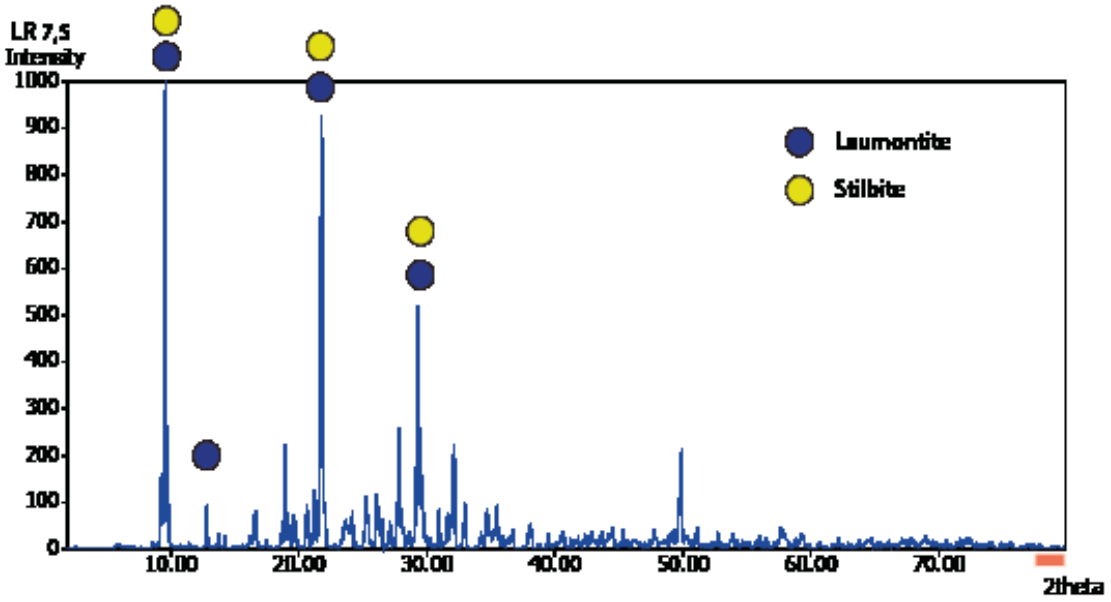
LR 7,5
Intensity
1000
900
800
700
600
500
400
300
200
100
0
10.00
20.00
30.00
40.00
50.00
60.00
70.00
2theta
Laumontite
Stilbite

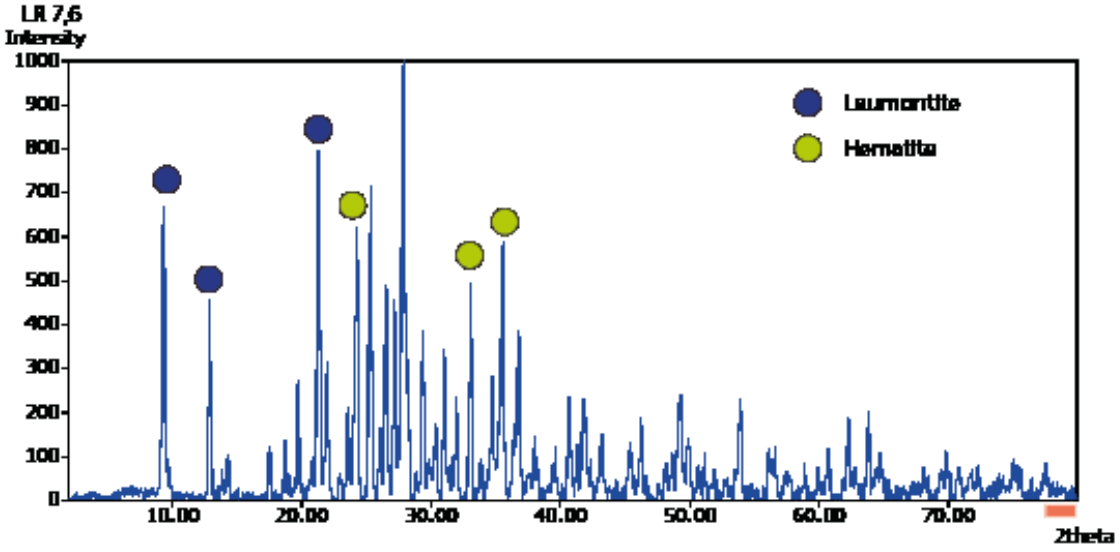
LR 7,6
Intensity
1000
900
800
700
600
500
400
300
200
100
0
10.00
20.00
30.00
40.00
50.00
60.00
70.00
2theta
Laumontite
Hematita

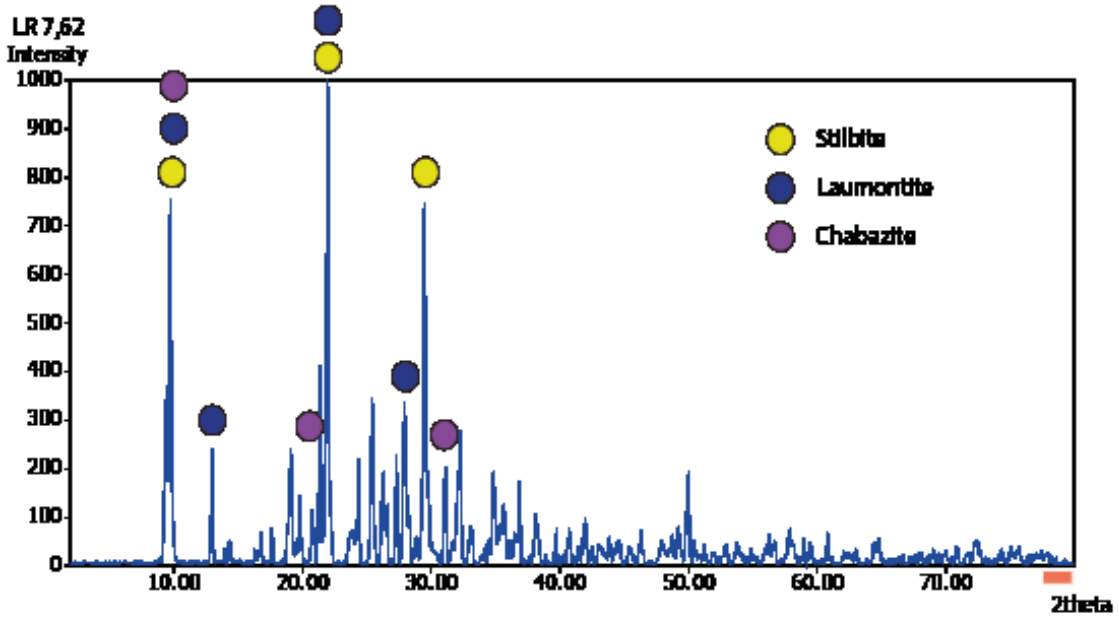
LR 7,62
Intensity
1000
900
800
700
600
500
400
300
200
100
0
10.00
20.00
30.00
40.00
50.00
60.00
70.00
2theta
Stilbite
Laumontite
Chabazite

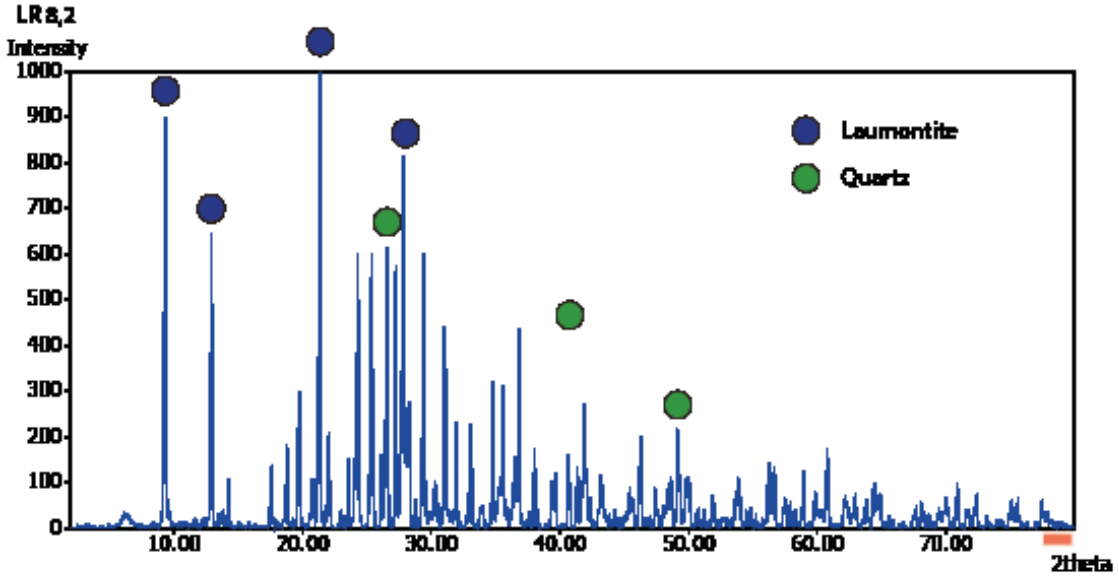
LR 8,2
Intensity
1000
900
800
700
600
500
400
300
200
100
0
10.00
20.00
30.00
40.00
50.00
60.00
70.00
2theta
Laumontite
Quartz

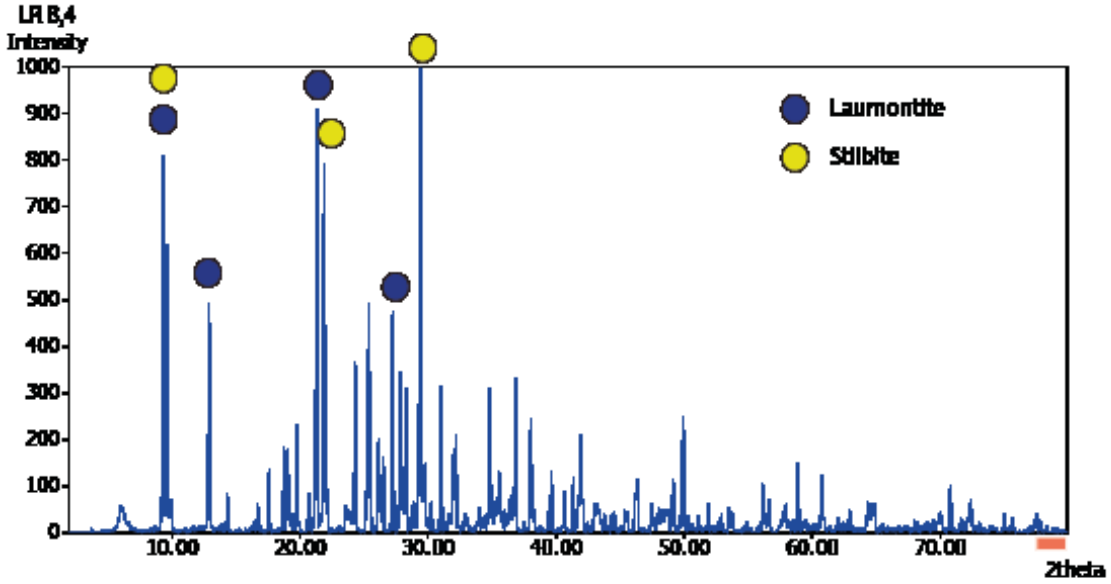
LR 8,4
Intensity
1000
900
800
700
600
500
400
300
200
100
0
10.00
20.00
30.00
40.00
50.00
60.00
70.00
2theta
Laumontite
Stilbite

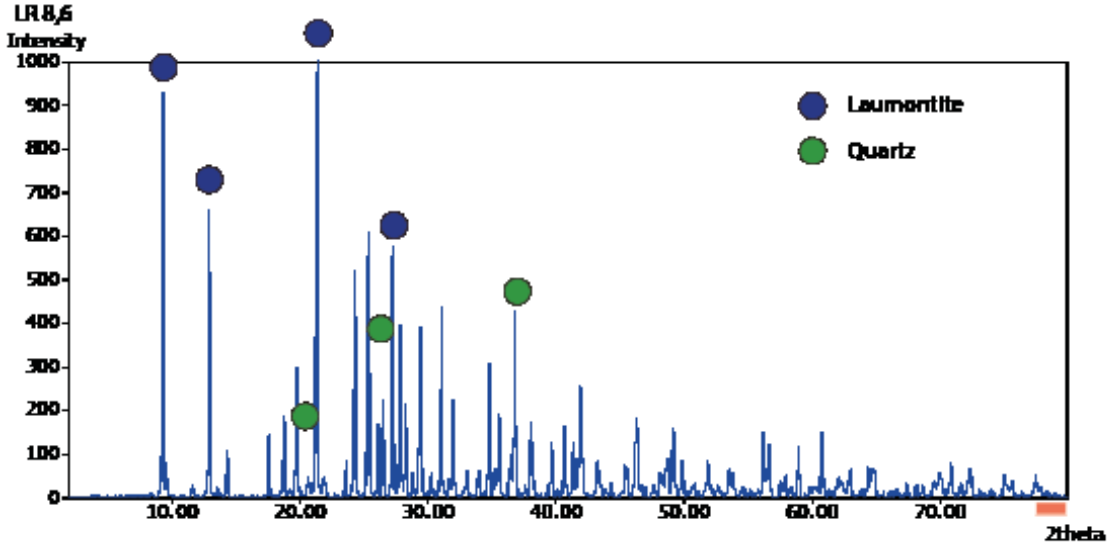
LR 8,6
Intensity
1000
900
800
700
600
500
400
300
200
100
0
10.00
20.00
30.00
40.00
50.00
60.00
70.00
2theta
Laumontite
Quartz

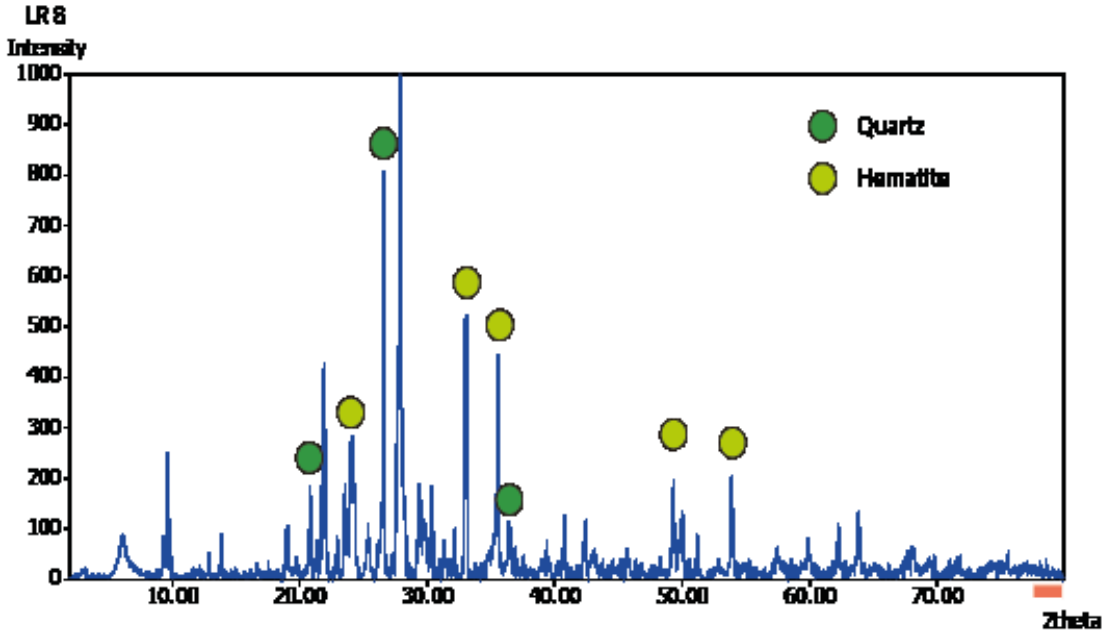
LR 8
Intensity
1000
900
800
700
600
500
400
300
200
100
0
10.00
20.00
30.00
40.00
50.00
60.00
70.00
2theta
Quartz
Hematite

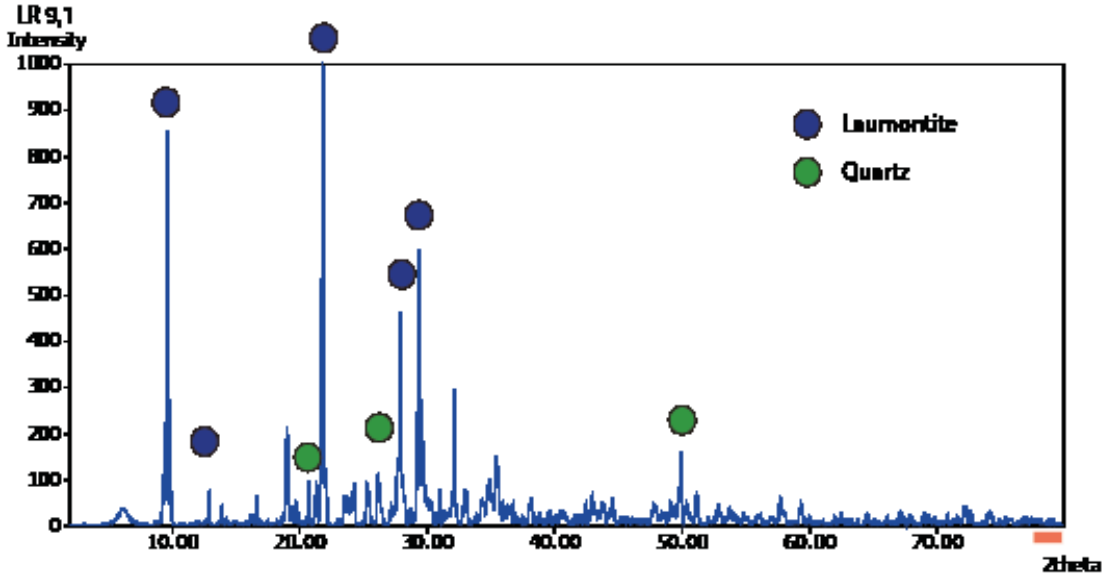
LR 9,1
Intensity
1000
900
800
700
600
500
400
300
200
100
0
10.00
20.00
30.00
40.00
50.00
60.00
70.00
2theta
Laumontite
Quartz

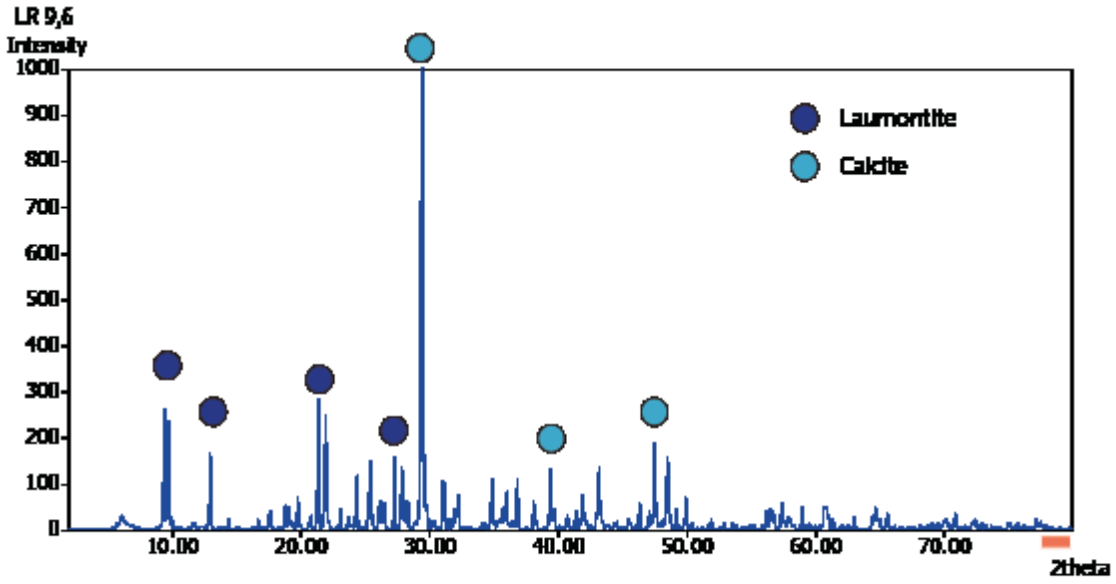
LR 9,6
Intensity
1000
900
800
700
600
500
400
300
200
100
0
10.00
20.00
30.00
40.00
50.00
60.00
70.00
2theta
Laumontite
Calcite

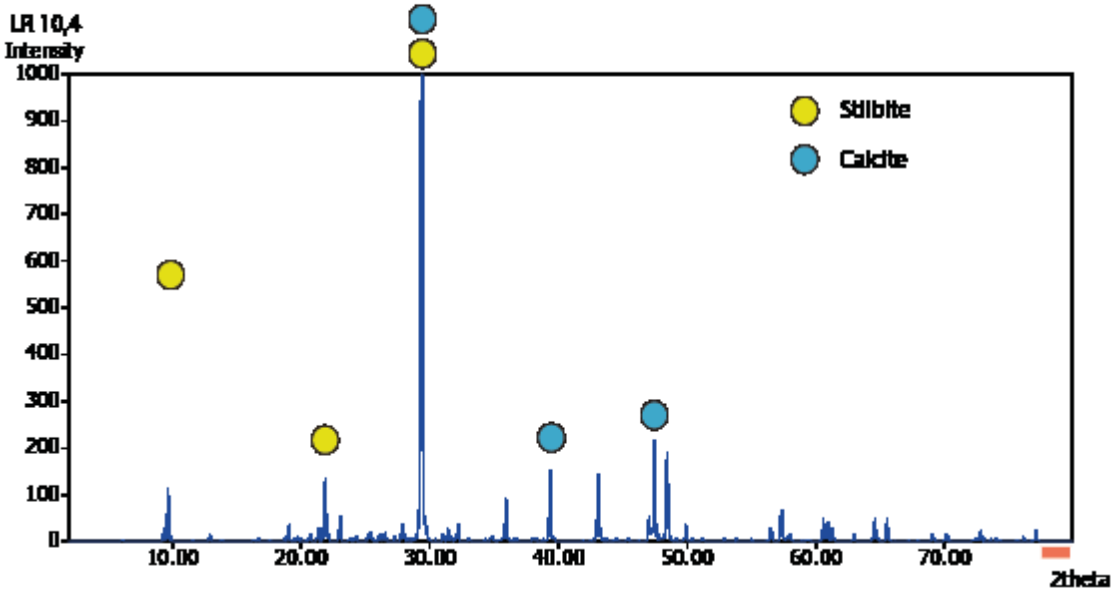
LR 10,4
Intensity
1000
900
800
700
600
500
400
300
200
100
0
10.00
20.00
30.00
40.00
50.00
60.00
70.00
2theta
Stilbite
Calcite

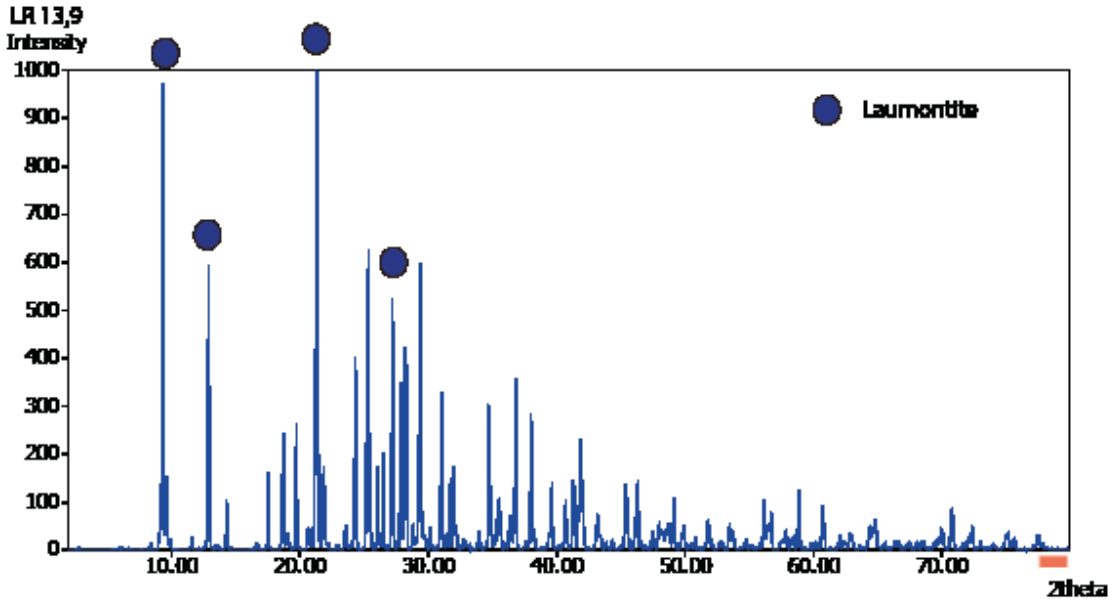
LR 13,9
Intensity
1000
900
800
700
600
500
400
300
200
100
0
Laumontite
10.00
20.00
30.00
40.00
50.00
60.00
70.00
2theta

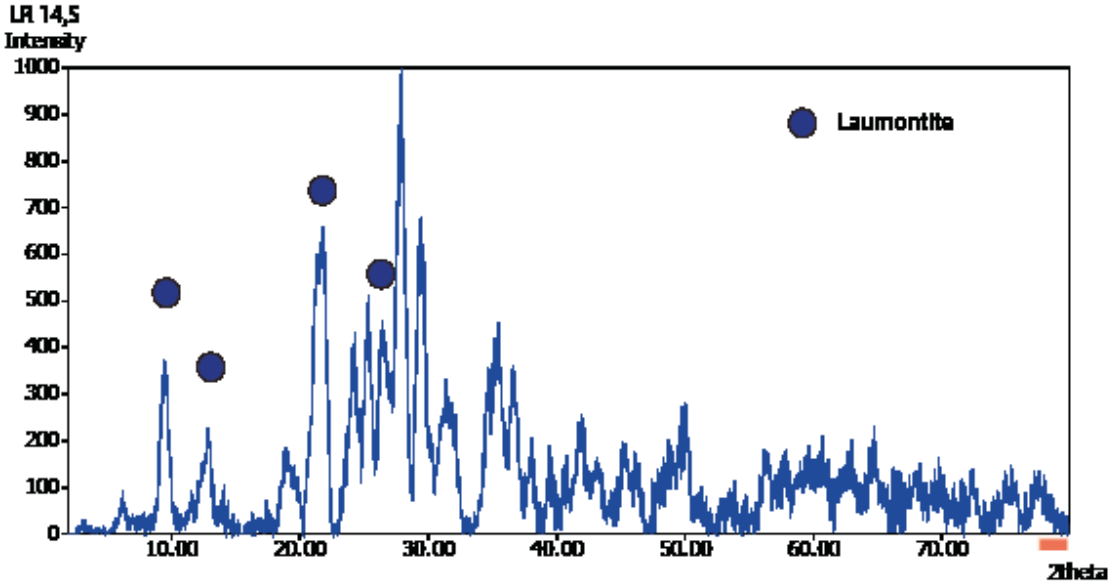
LR 14,5
Intensity
1000
900
800
700
600
500
400
300
200
100
0
Laumontite
10.00
20.00
30.00
40.00
50.00
60.00
70.00
2theta

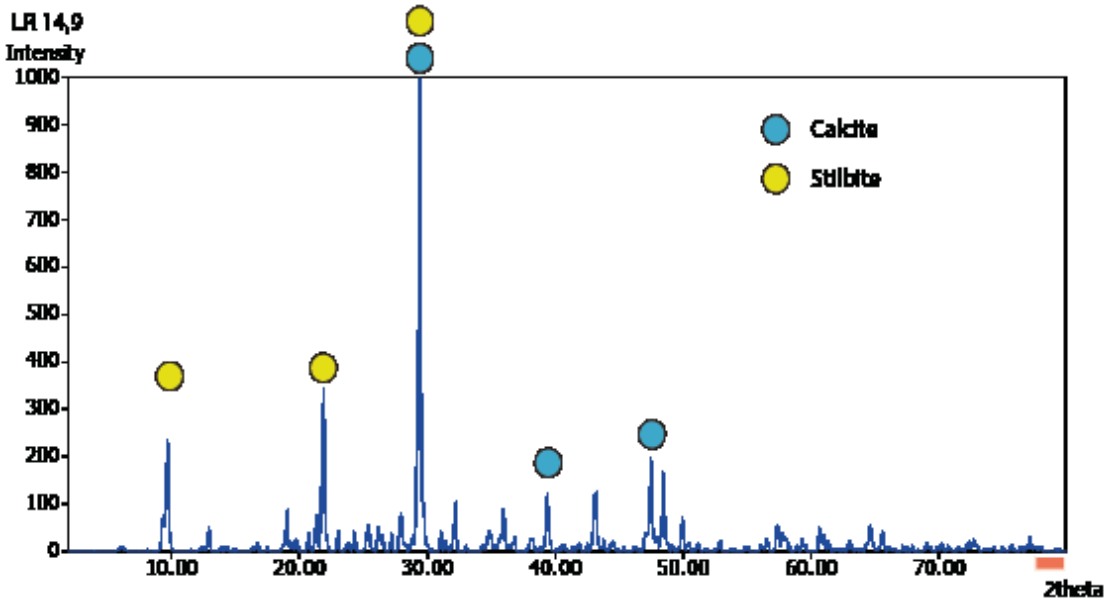
LR 14,9
Intensity
1000
900
800
700
600
500
400
300
200
100
0
10.00
20.00
30.00
40.00
50.00
60.00
70.00
2theta
Calcite
Stilbite

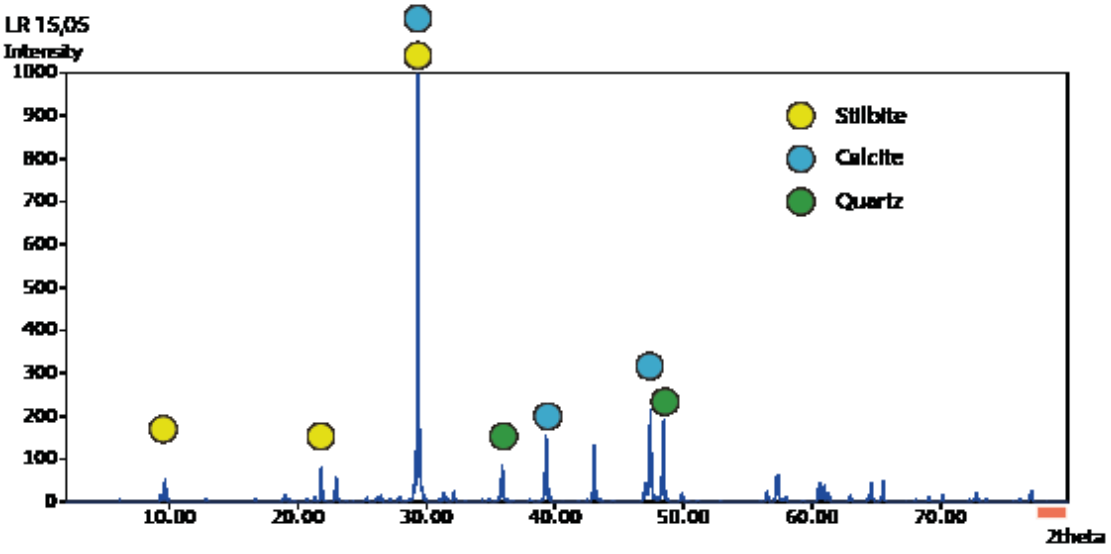
LR 15,05
Intensity
1000
900
800
700
600
500
400
300
200
100
0
10.00
20.00
30.00
40.00
50.00
60.00
70.00
2theta
Stilbite
Calcite
Quartz

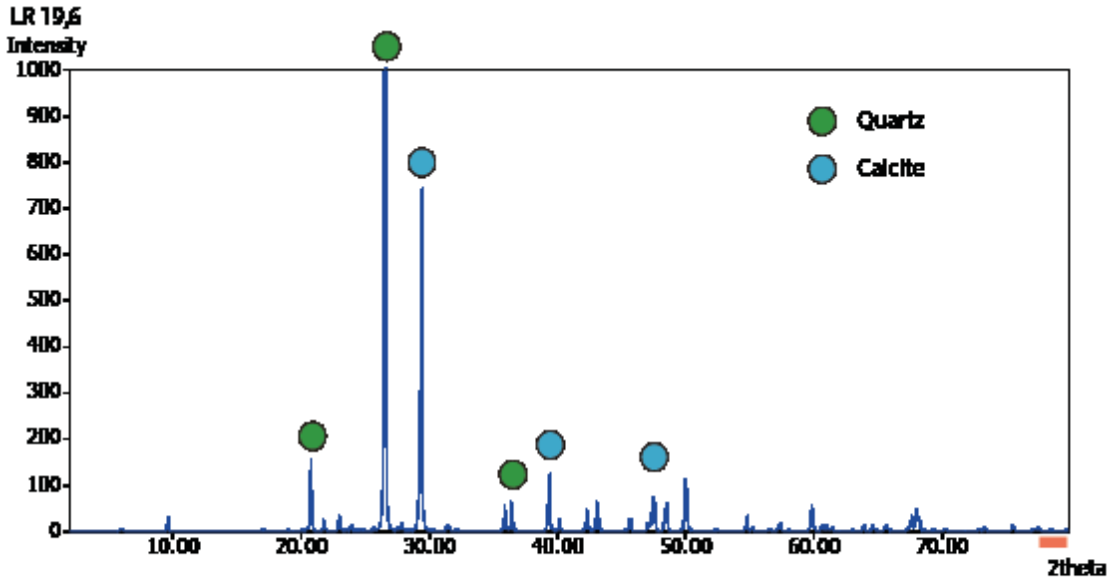
LR 19,6
Intensity
1000
900
800
700
600
500
400
300
200
100
0
10.00
20.00
30.00
40.00
50.00
60.00
70.00
2theta
Quartz
Calcite

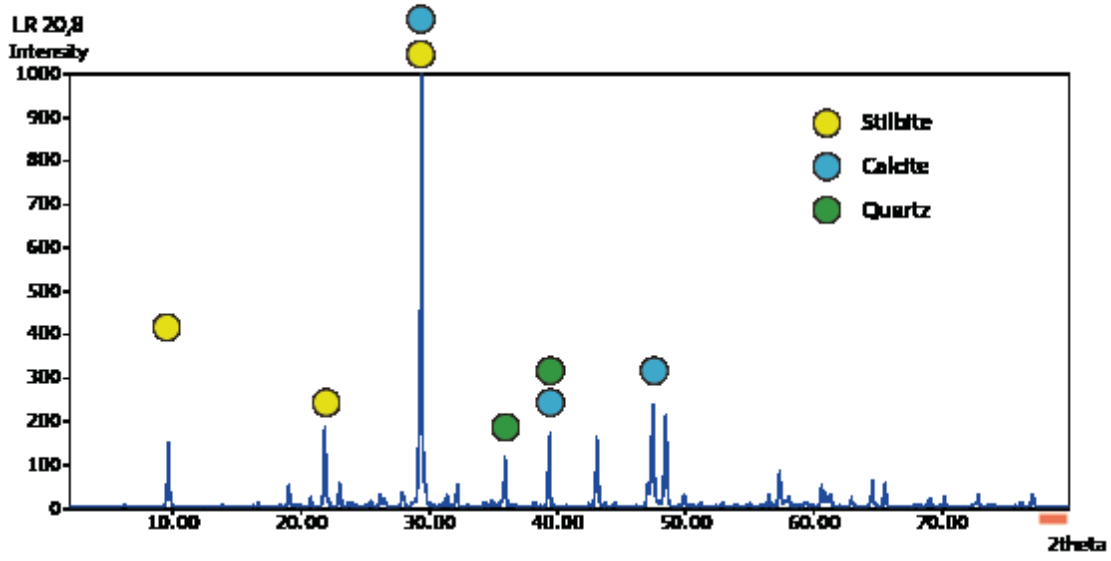
LR 20,8
Intensity
1000
900
800
700
600
500
400
300
200
100
0
10.00
20.00
30.00
40.00
50.00
60.00
70.00
2theta
Stilbite
Calcite
Quartz

Table G-2. Summarized results of the interpreted diffractograms of the ALFS exposure.

Sample	Geographical coordinates [PSAD56-UTM]		Mineralogy
	N	E	
LAZI1.5	5730616.94	287869.94	Natrolite; Yugawaralite
LAZI1	5730617.29	287870.29	Laumontite; Yugawaralite
LAZI2.2	5730616.44	287869.44	Natrolite; Quartz
LAZI3.4	5730615.60	287868.60	Laumontite; Quartz
LAZI4	5730615.17	287868.17	Laumontite; Scolecite
LAZI5.2	5730614.32	287867.32	Laumontite; Calcite
LAZI5.4	5730614.18	287867.18	Laumontite; Mordenite
LAZI5.6	5730614.04	287867.04	Laumontite; Quartz
LAZI5.75	5730613.93	287866.93	Laumontite
LAZI5	5730614.46	287867.46	Laumontite; Natrolite
LAZI6.56	5730613.36	287866.36	Stilbite; Natrolite
LAZI7.2	5730612.91	287865.91	Natrolite; Laumontite; Feldspar
LAZI7	5730612.98	287865.98	Laumontite; Feldspar; Scolecite
LAZI8.07	5730612.29	287865.29	Laumontite; Natrolite
LAZI8.8	5730611.78	287864.78	Laumontite; Quartz
LAZI9.1	5730611.57	287864.57	Laumontite; Quartz
LAZI9.7	5730611.14	287864.14	Stilbite; Scolecite; Natrolite; Feldspar
LAZI10.1	5730610.86	287863.86	Scolecite; Natrolite
LAZI10.24	5730610.76	287863.76	Natrolite; Micas; Feldspar
LAZI11.45	5730609.90	287862.90	Stilbite; Scolecite
LAZI11.71	5730609.72	287862.72	Laumontite
LAZI12.5	5730609.16	287862.16	Laumontite; Scolecite
LAZI12.38	5730609.27	287862.27	Laumontite; Chabacite
LAZI12.83	5730608.93	287861.93	Laumontite; Scolecite
LAZI14.74	5730607.58	287860.58	Yugawaralite
LAZI15.52	5730607.03	287860.03	Laumontite; Wairakite
LAZI17.2	5730605.84	287858.84	Stilbite; Heulandite; Feldspar
LAZI17.25	5730605.80	287858.80	Laumontite
LAZI17.46	5730605.53	287858.53	Laumontite
LAZI17.76	5730605.44	287858.44	Stilbite; Pyroxene
LAZI18.2	5730605.13	287858.13	Laumontite
LAZI19.05	5730604.53	287857.53	Laumontite; Chabacite
LAZI19.5	5730604.21	287857.21	Laumontite
LAZI19.6	5730604.14	287857.14	Laumontite

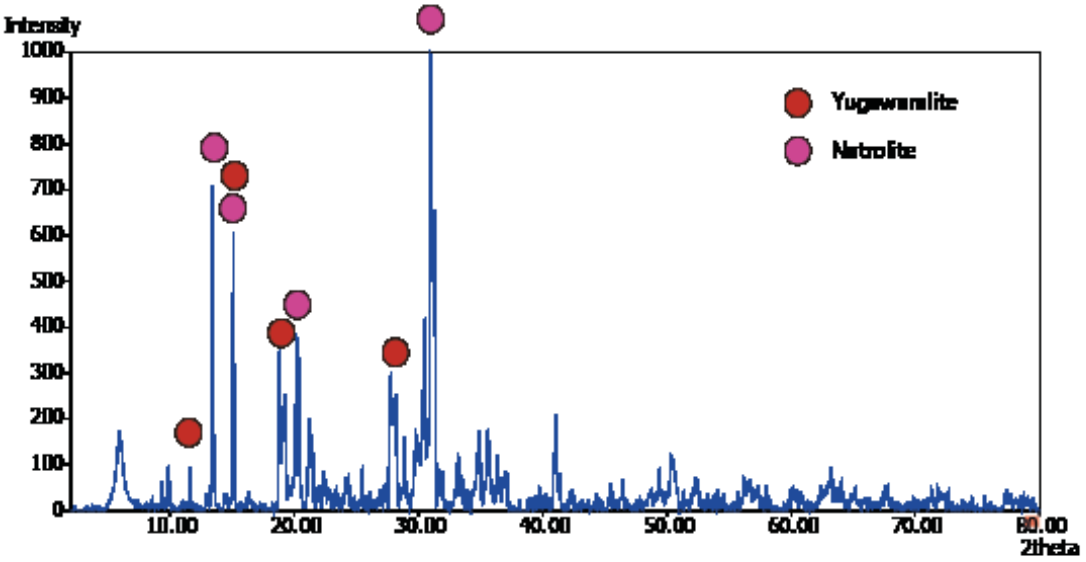
Intensity
1000
900
800
700
600
500
400
300
200
100
0
10.00
20.00
30.00
40.00
50.00
60.00
70.00
80.00
2theta
Yugawaralite
Natrolite

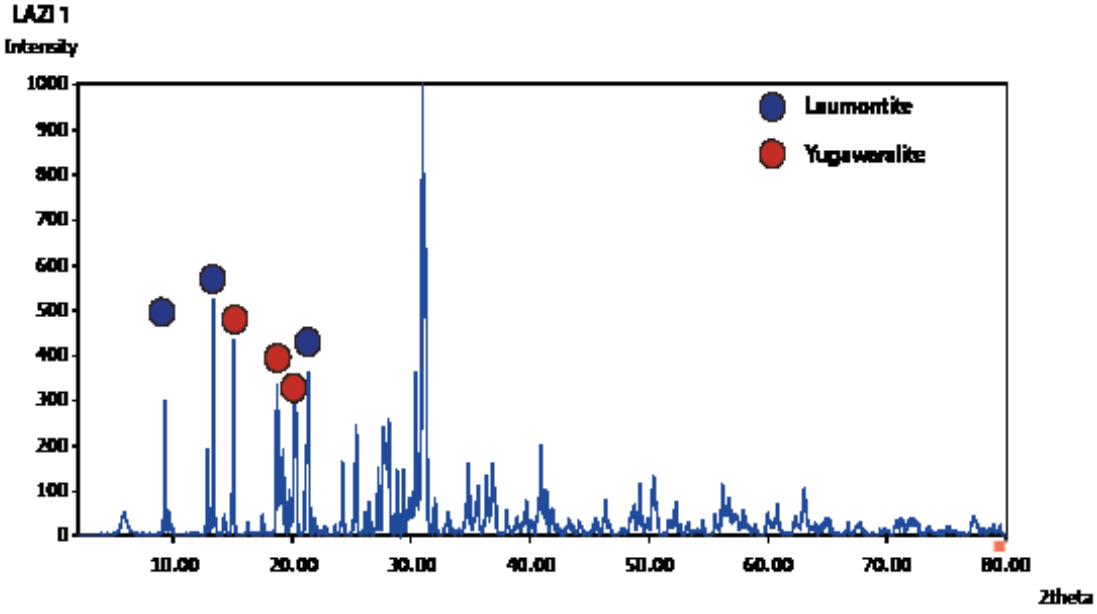
LAZI 1
Intensity
1000
900
800
700
600
500
400
300
200
100
0
10.00
20.00
30.00
40.00
50.00
60.00
70.00
80.00
2theta
Laumontite
Yugawaralite

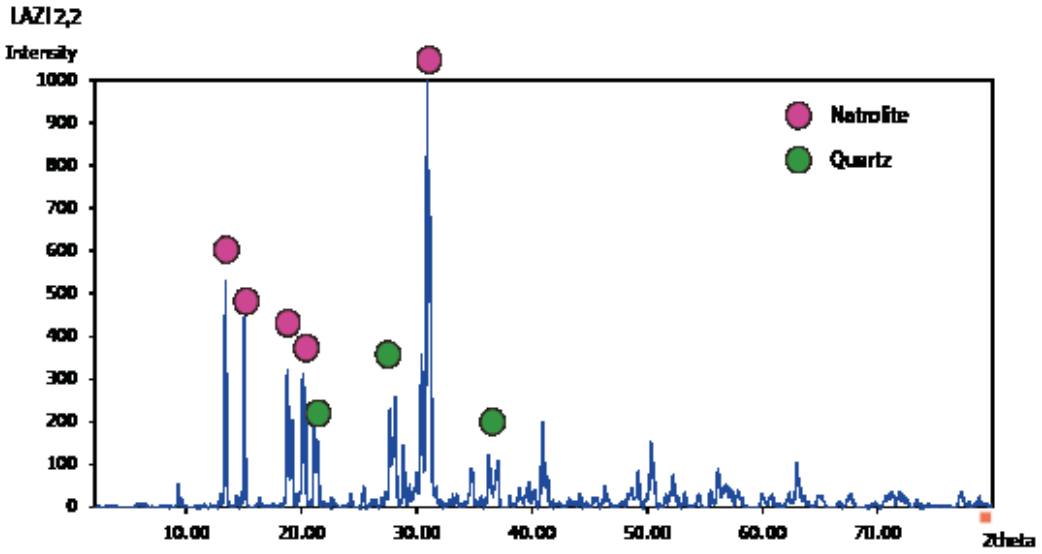
LAZI2,2
Intensity
1000
900
800
700
600
500
400
300
200
100
0
Natrolite
Quartz
10.00
20.00
30.00
40.00
50.00
60.00
70.00
2theta

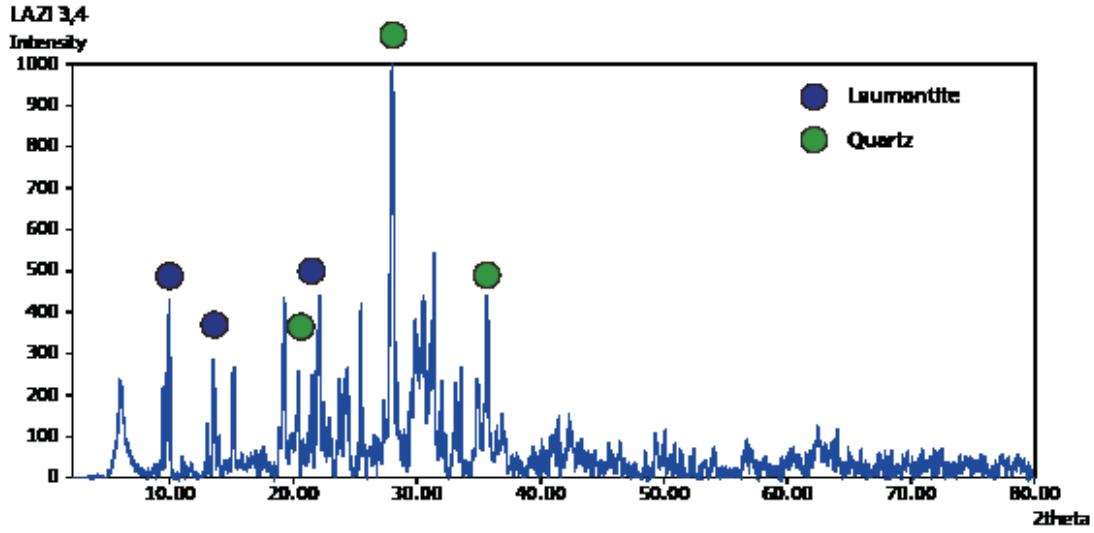
LAZI 3,4
Intensity
1000
900
800
700
600
500
400
300
200
100
0
Laumontite
Quartz
10.00
20.00
30.00
40.00
50.00
60.00
70.00
80.00
2theta

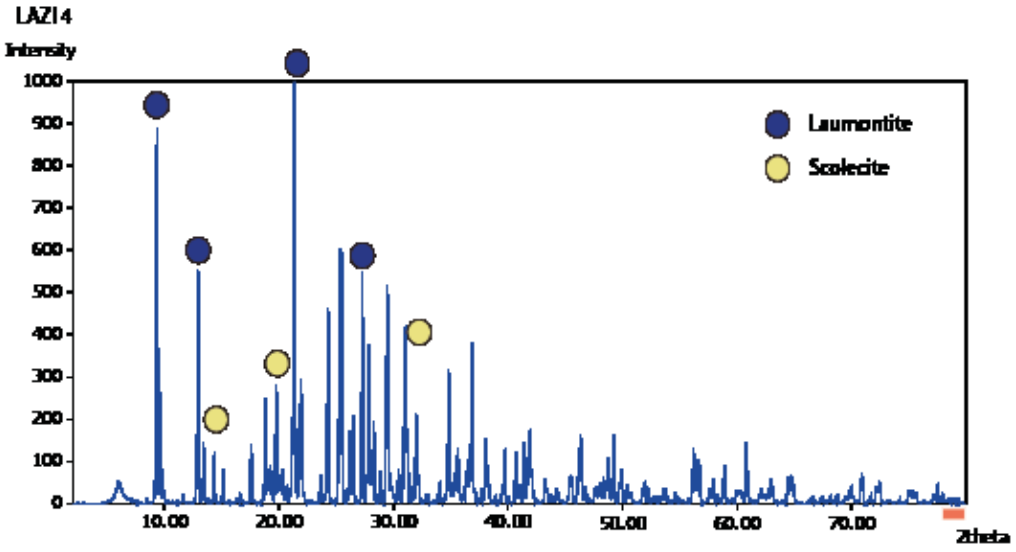
LAZI 4
Intensity
1000
900
800
700
600
500
400
300
200
100
0
10.00
20.00
30.00
40.00
50.00
60.00
70.00
2theta
Laumontite
Scolecite

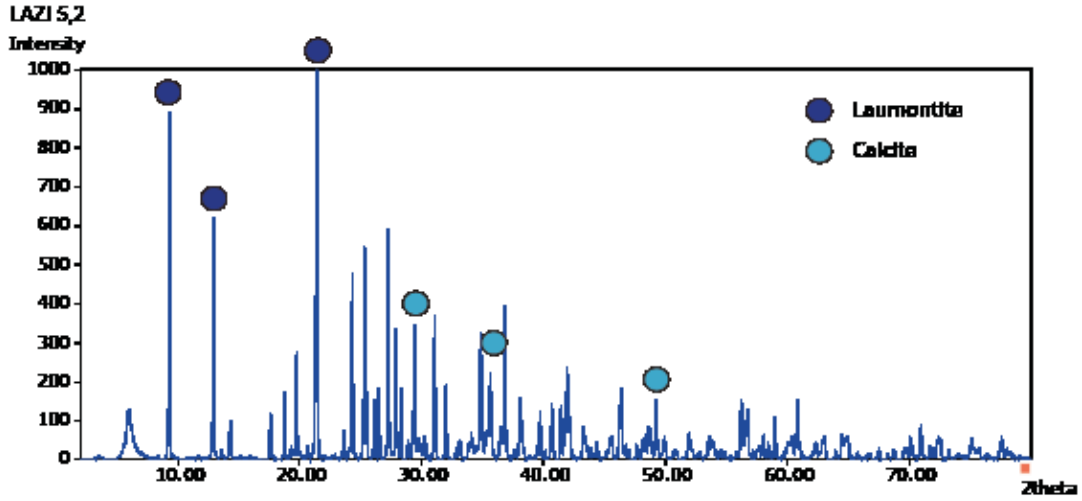
LAZI S,2
Intensity
1000
900
800
700
600
500
400
300
200
100
0
10.00
20.00
30.00
40.00
50.00
60.00
70.00
2theta
Laumontite
Calcite

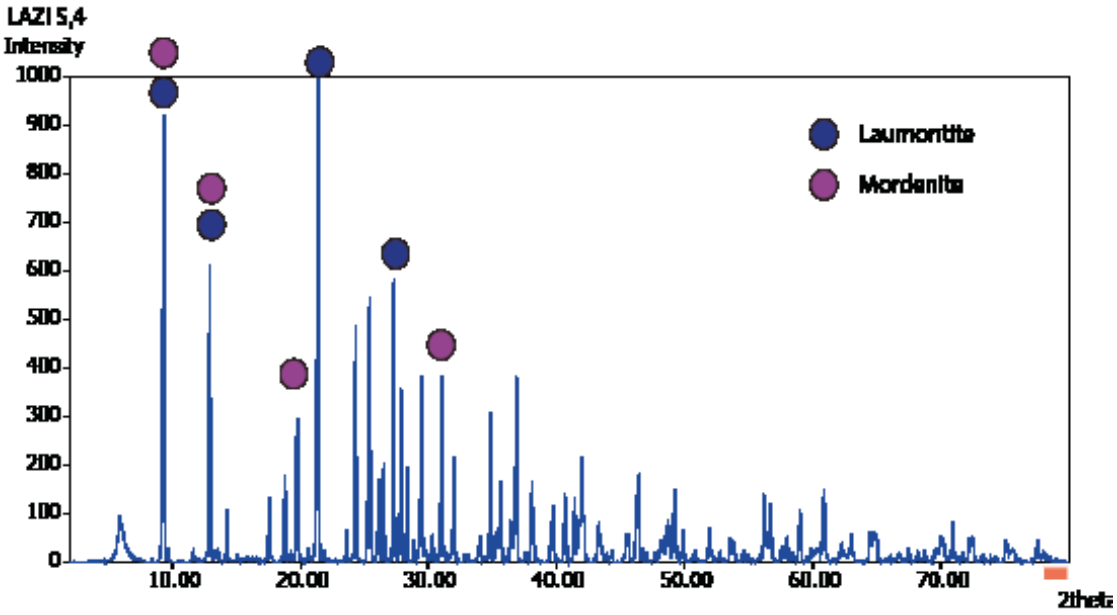
LAZI S,4
Intensity
1000
900
800
700
600
500
400
300
200
100
0
10.00
20.00
30.00
40.00
50.00
60.00
70.00
2theta
Laumontite
Mordenite

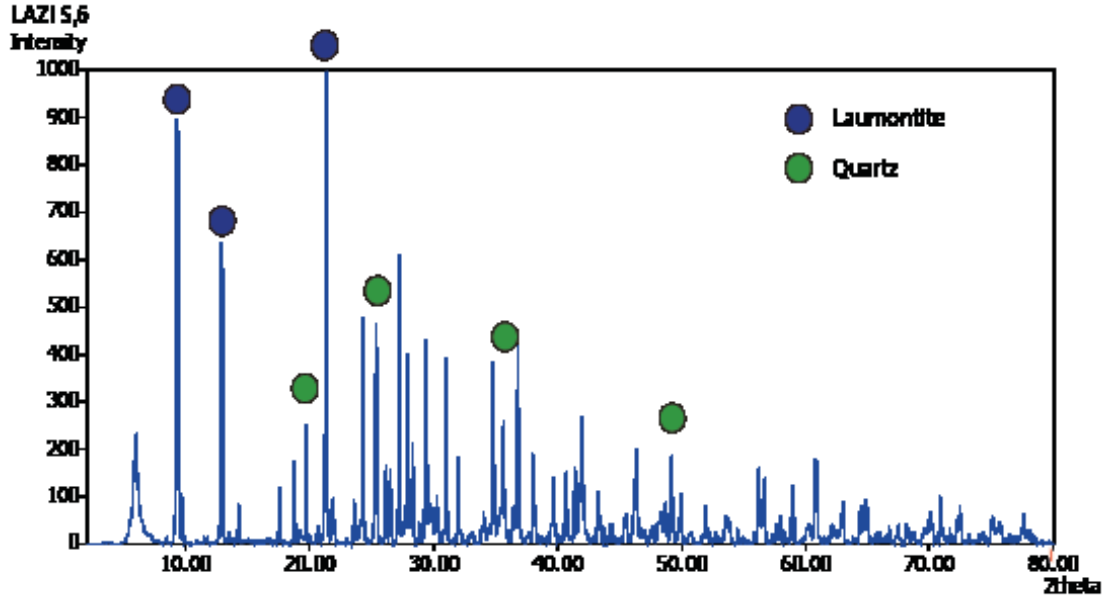
LAZI S,6
Intensity
1000
900
800
700
600
500
400
300
200
100
0
10.00
20.00
30.00
40.00
50.00
60.00
70.00
80.00
2theta
Laumontite
Quartz

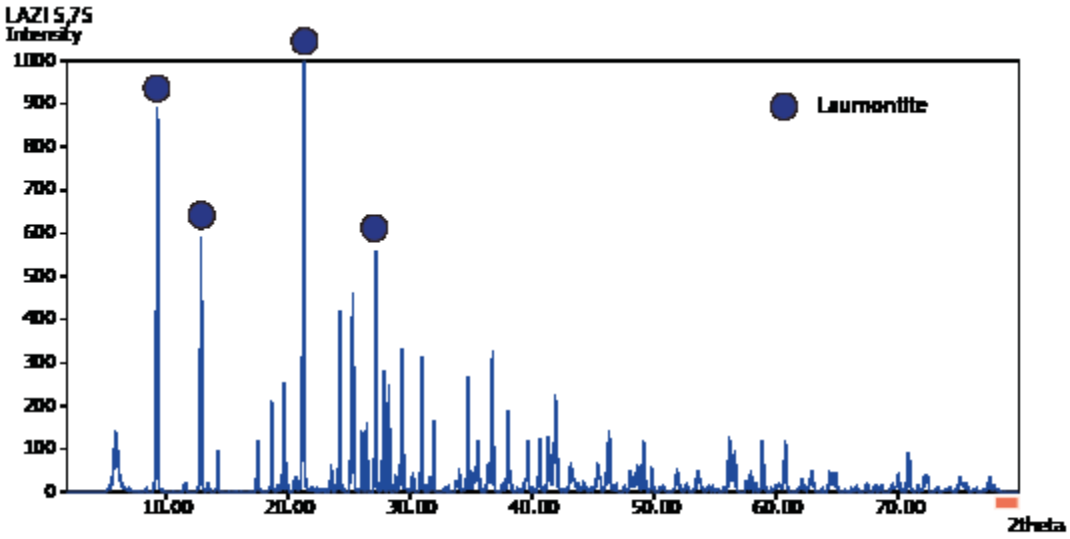
LAZI S.7S
Intensity
1000
900
800
700
600
500
400
300
200
100
0
10.00
20.00
30.00
40.00
50.00
60.00
70.00
2theta
Laumontite

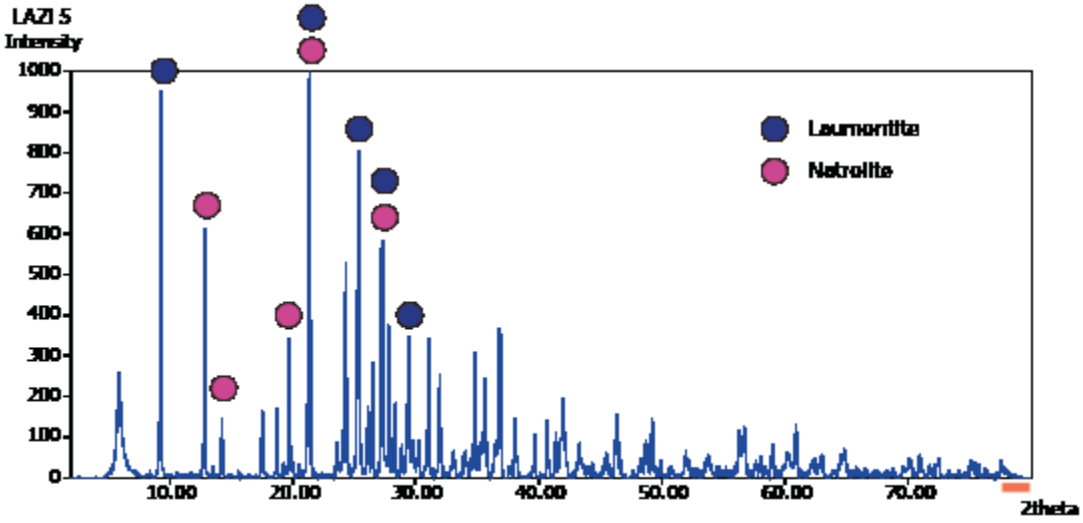
LAZI S
Intensity
1000
900
800
700
600
500
400
300
200
100
0
10.00
20.00
30.00
40.00
50.00
60.00
70.00
2theta
Laumontite
Natrolite

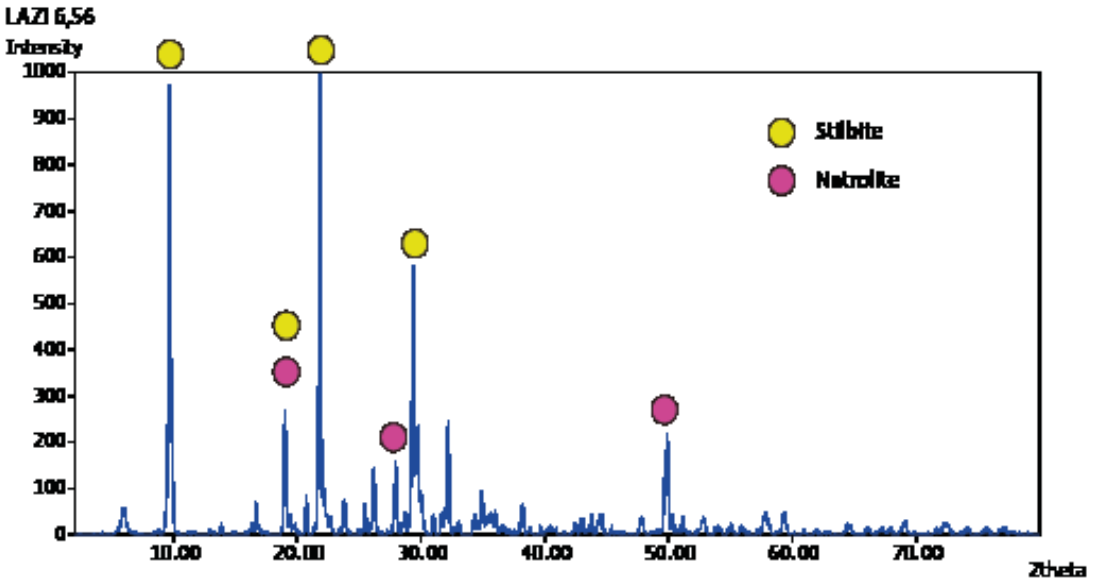
LAZI 6,56
Intensity
1000
900
800
700
600
500
400
300
200
100
0
10.00
20.00
30.00
40.00
50.00
60.00
70.00
2theta
Stilbite
Natrolite

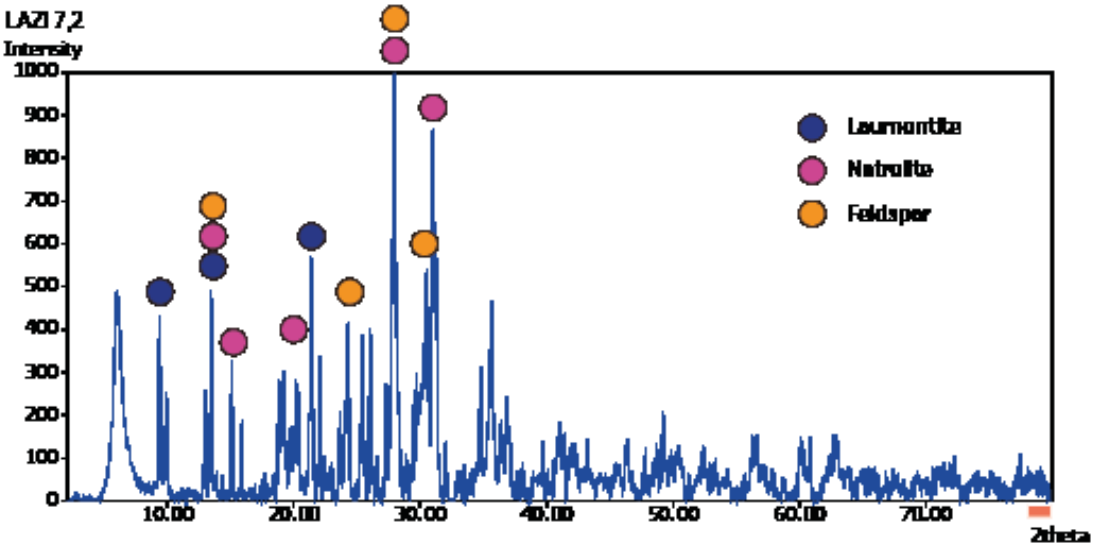
LAZI 7,2
Intensity
1000
900
800
700
600
500
400
300
200
100
0
10.00
20.00
30.00
40.00
50.00
60.00
70.00
2theta
Laumontite
Natrolite
Feldspar

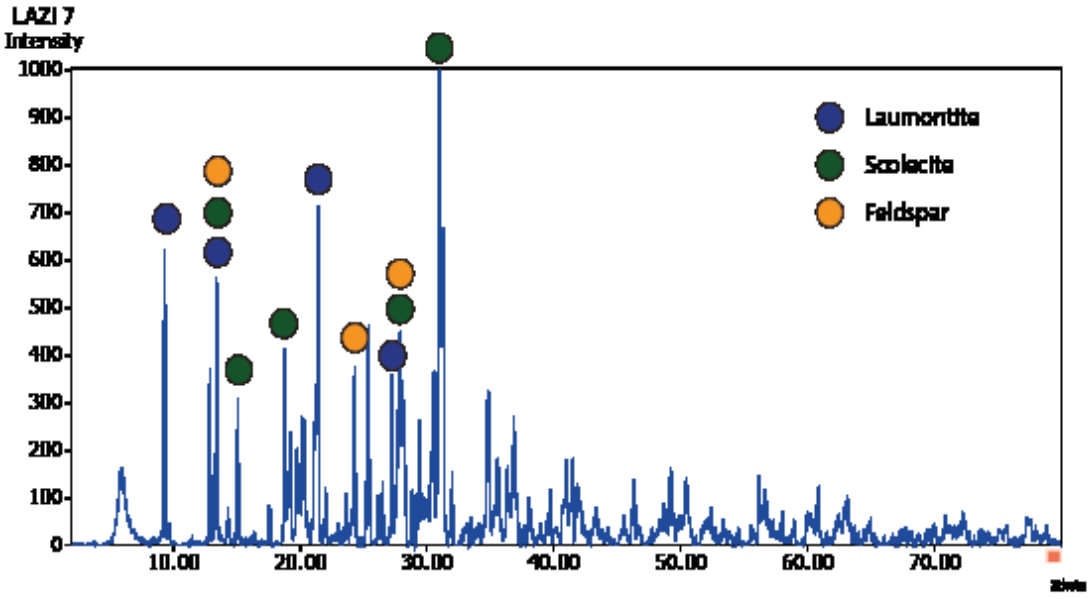
LAZI 7
Intensity
1000
900
800
700
600
500
400
300
200
100
0
10.00
20.00
30.00
40.00
50.00
60.00
70.00
Laumontite
Scolacite
Feldspar

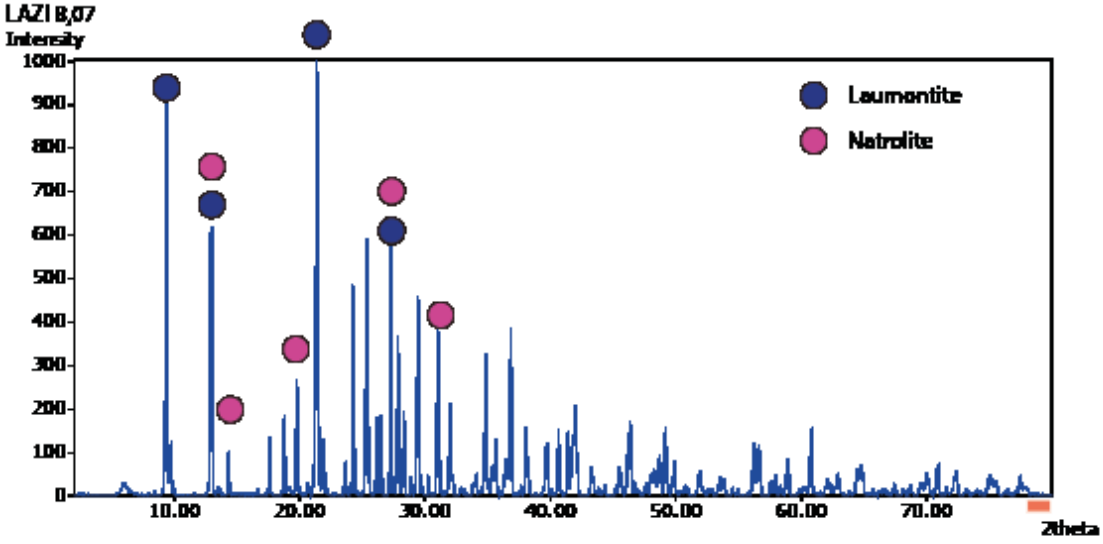
LAZI 8,07
Intensity
1000
900
800
700
600
500
400
300
200
100
0
10.00
20.00
30.00
40.00
50.00
60.00
70.00
Laumontite
Natrolite

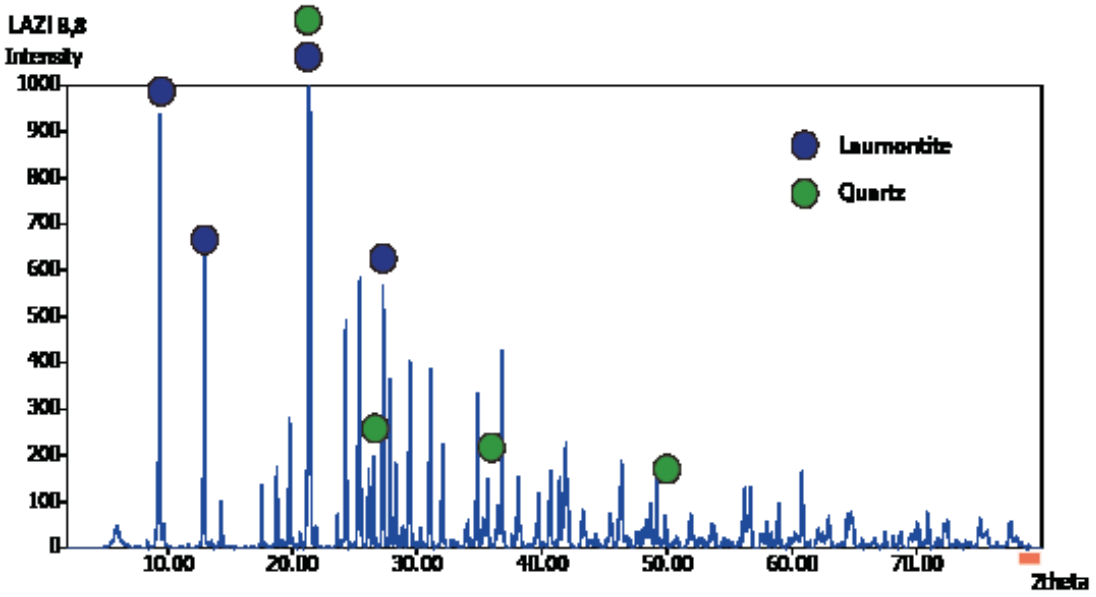
LAZI 8,8
Intensity
1000
900
800
700
600
500
400
300
200
100
0
10.00
20.00
30.00
40.00
50.00
60.00
70.00
2theta
Laumontite
Quartz

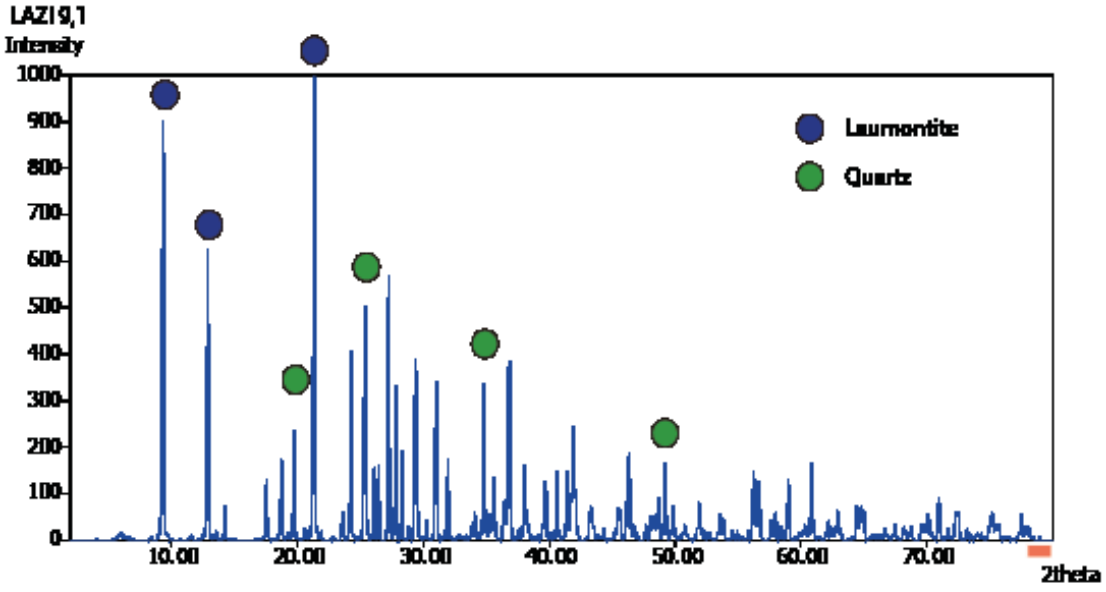
LAZI 9,1
Intensity
1000
900
800
700
600
500
400
300
200
100
0
10.00
20.00
30.00
40.00
50.00
60.00
70.00
2theta
Laumontite
Quartz

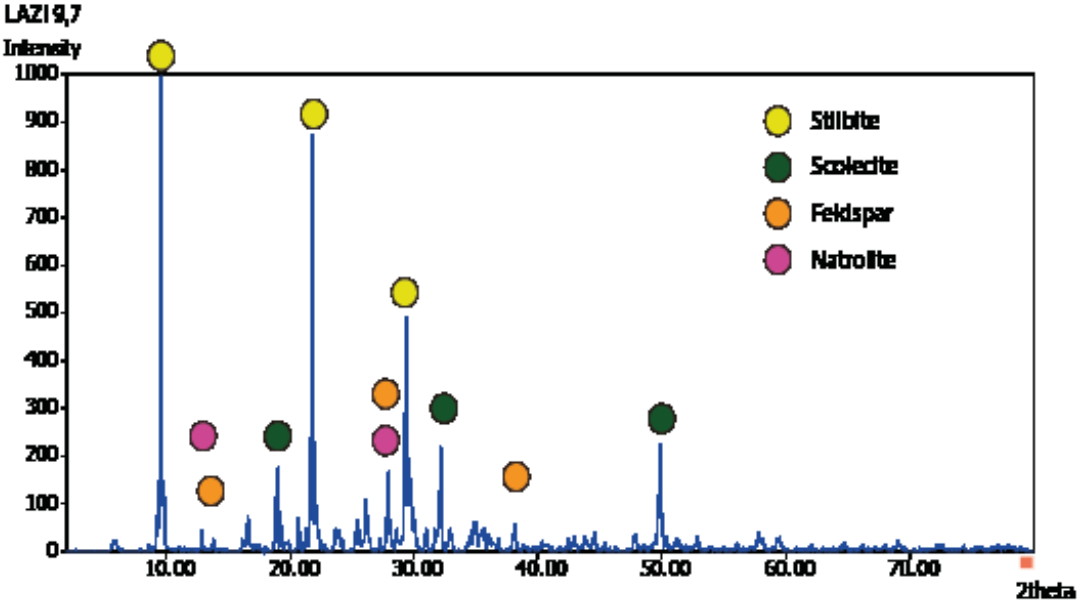
LAZ19,7
Intensity
1000
900
800
700
600
500
400
300
200
100
0
10.00
20.00
30.00
40.00
50.00
60.00
70.00
2theta
Stilbite
Scolecite
Feldspar
Natrolite

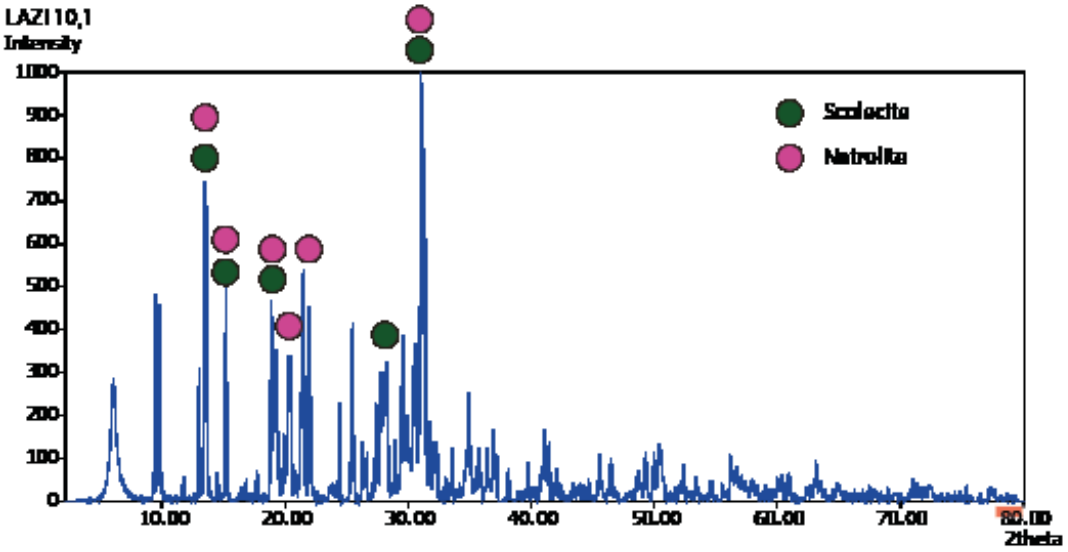
LAZ110,1
Intensity
1000
900
800
700
600
500
400
300
200
100
0
10.00
20.00
30.00
40.00
50.00
60.00
70.00
80.00
2theta
Scolecite
Natrolite

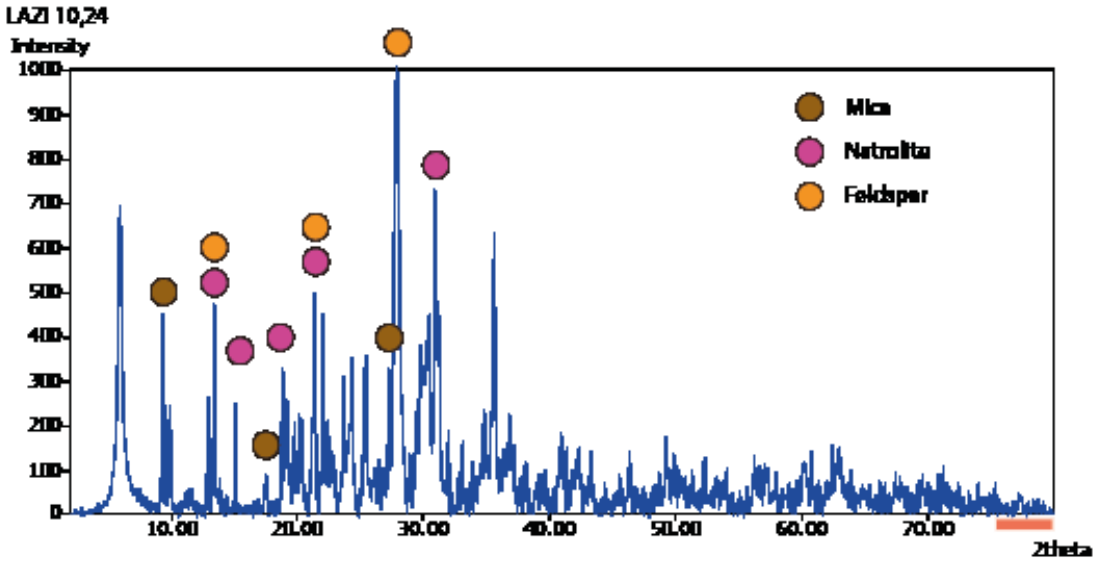
LAZI 10,24
Intensity
1000
900
800
700
600
500
400
300
200
100
0
10.00
20.00
30.00
40.00
50.00
60.00
70.00
2theta
Mica
Natrolite
Feldspar

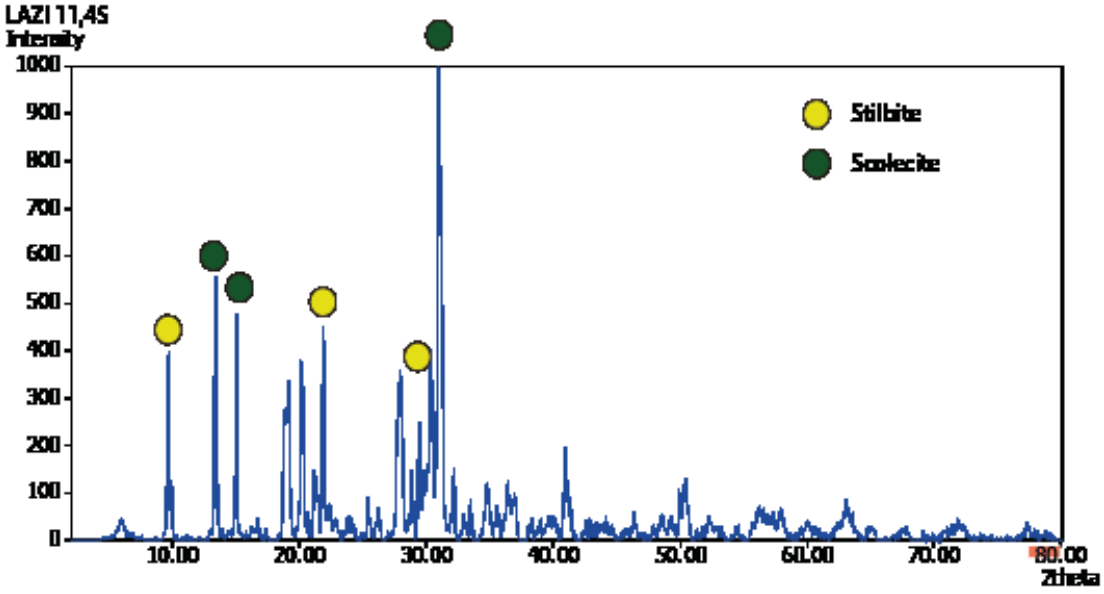
LAZI 11,45
Intensity
1000
900
800
700
600
500
400
300
200
100
0
10.00
20.00
30.00
40.00
50.00
60.00
70.00
80.00
2theta
Stilbite
Scolecite

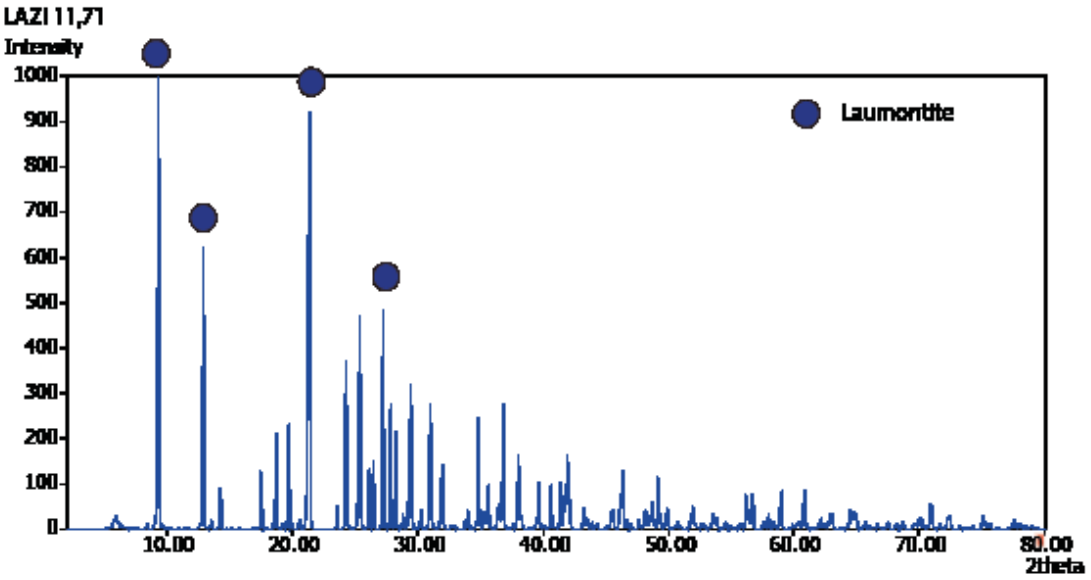
LAZI 11,71
Intensity
1000
900
800
700
600
500
400
300
200
100
0
10.00
20.00
30.00
40.00
50.00
60.00
70.00
80.00
2theta
Laumontite

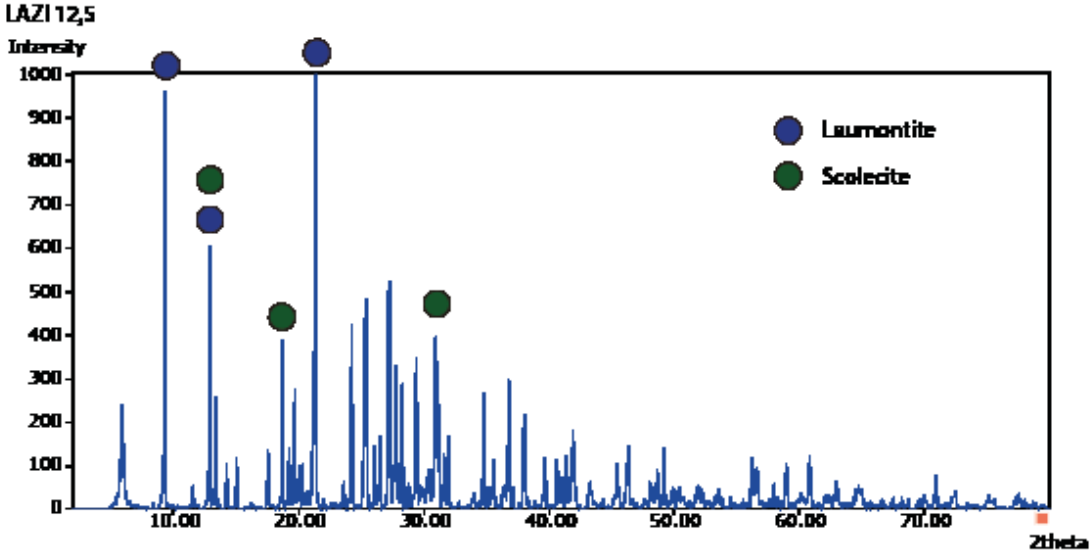
LAZI 12,5
Intensity
1000
900
800
700
600
500
400
300
200
100
0
10.00
20.00
30.00
40.00
50.00
60.00
70.00
2theta
Laumontite
Scolecite

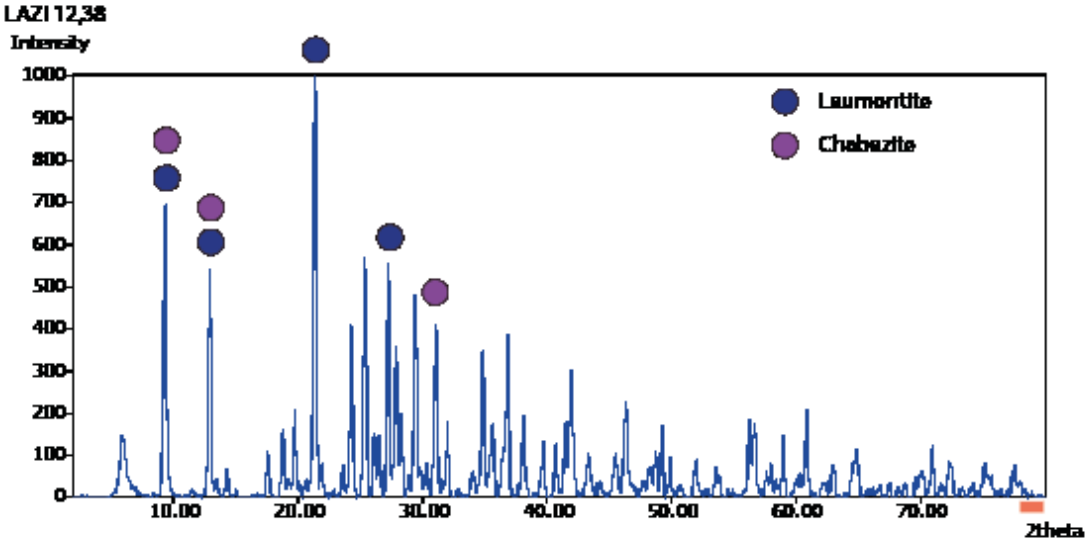
LAZI 12,38
Intensity
1000
900
800
700
600
500
400
300
200
100
0
10.00
20.00
30.00
40.00
50.00
60.00
70.00
2theta
Laumontite
Chabazite

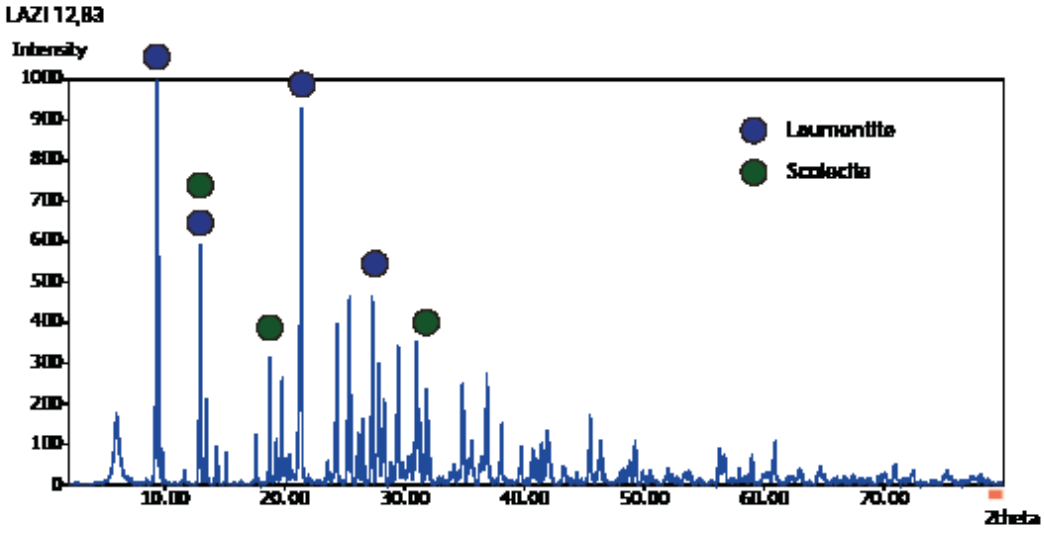
LAZI 12,83
Intensity
1000
900
800
700
600
500
400
300
200
100
0
10.00
20.00
30.00
40.00
50.00
60.00
70.00
2theta
Laumontite
Scolecite

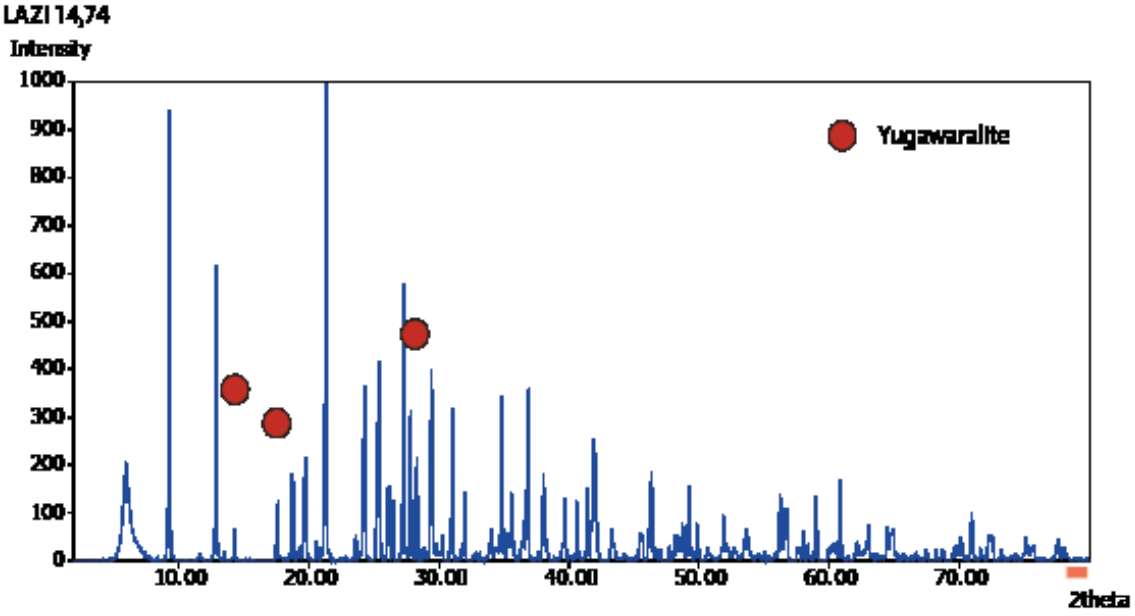
LAZI 14,74
Intensity
1000
900
800
700
600
500
400
300
200
100
0
10.00
20.00
30.00
40.00
50.00
60.00
70.00
2theta
Yugawaralite

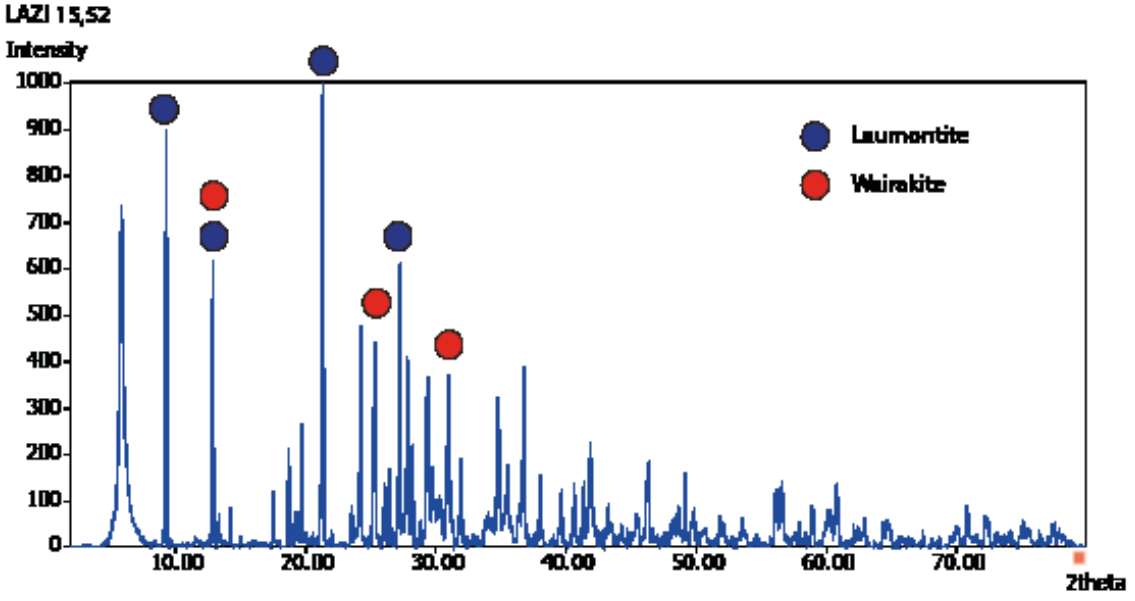
LAZI 15,52
Intensity
1000
900
800
700
600
500
400
300
200
100
0
10.00
20.00
30.00
40.00
50.00
60.00
70.00
2theta
Laumontite
Wairakite

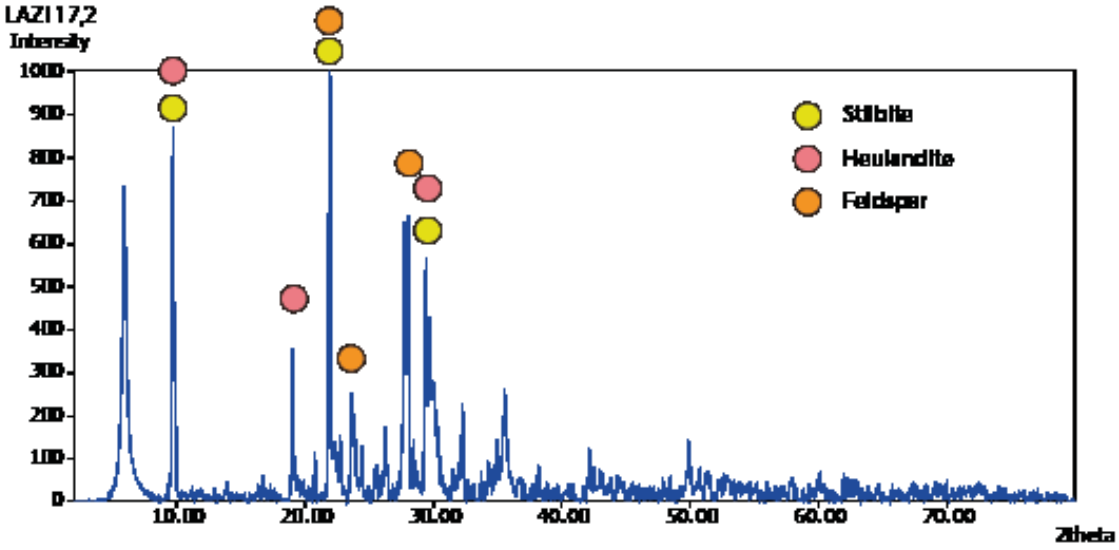
LAZI17,2
Intensity
1000
900
800
700
600
500
400
300
200
100
0
10.00
20.00
30.00
40.00
50.00
60.00
70.00
2theta
Stilbite
Heulandite
Feldspar

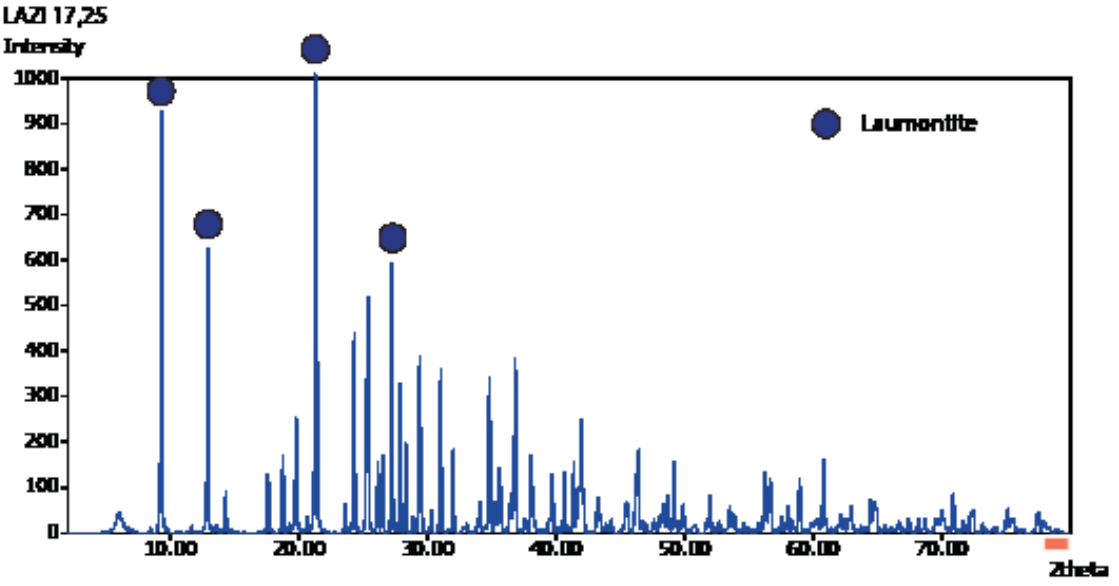
LAZI 17,25
Intensity
1000
900
800
700
600
500
400
300
200
100
0
10.00
20.00
30.00
40.00
50.00
60.00
70.00
2theta
Laumontite

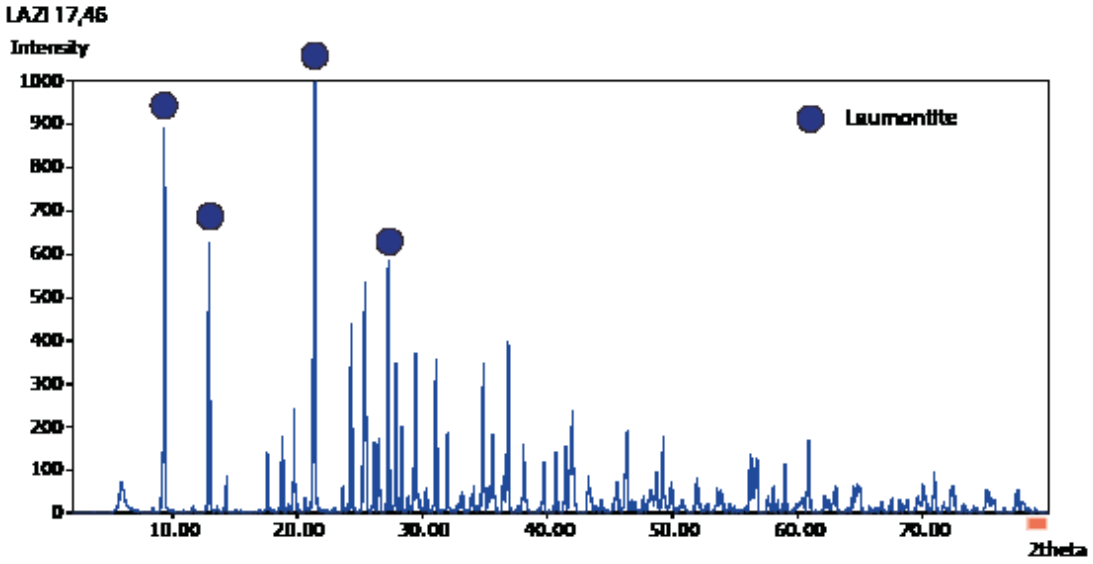
LAZI 17,46
Intensity
1000
900
800
700
600
500
400
300
200
100
0
10.00
20.00
30.00
40.00
50.00
60.00
70.00
2theta
Laumontite

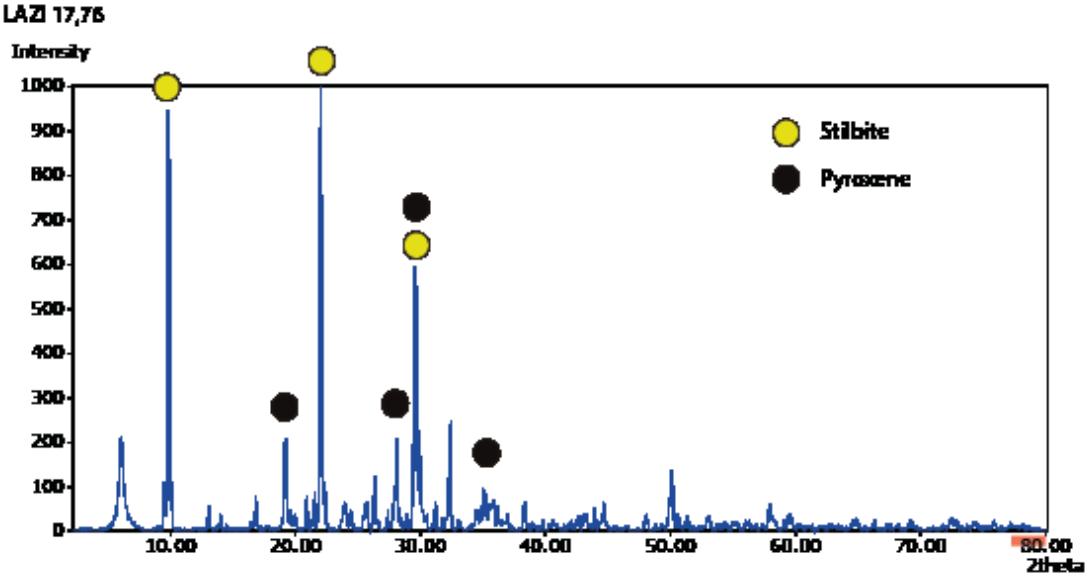
LAZI 17,76
Intensity
1000
900
800
700
600
500
400
300
200
100
0
10.00
20.00
30.00
40.00
50.00
60.00
70.00
80.00
2theta
Stilbite
Pyroxene

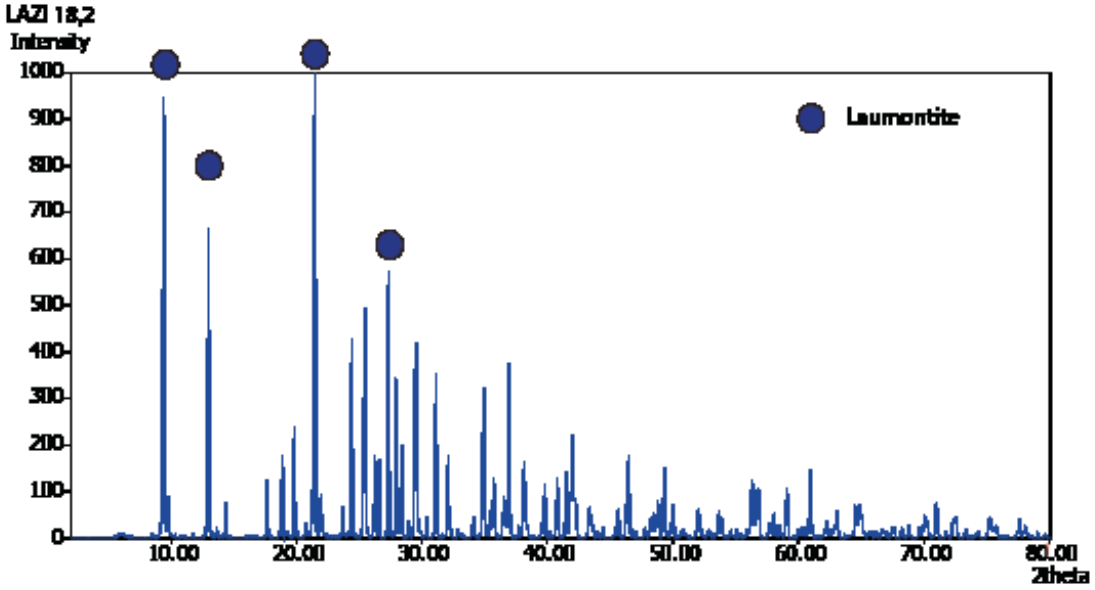
LAZI 18,2
Intensity
1000
900
800
700
600
500
400
300
200
100
0
10.00
20.00
30.00
40.00
50.00
60.00
70.00
80.00
2theta
Laumontite

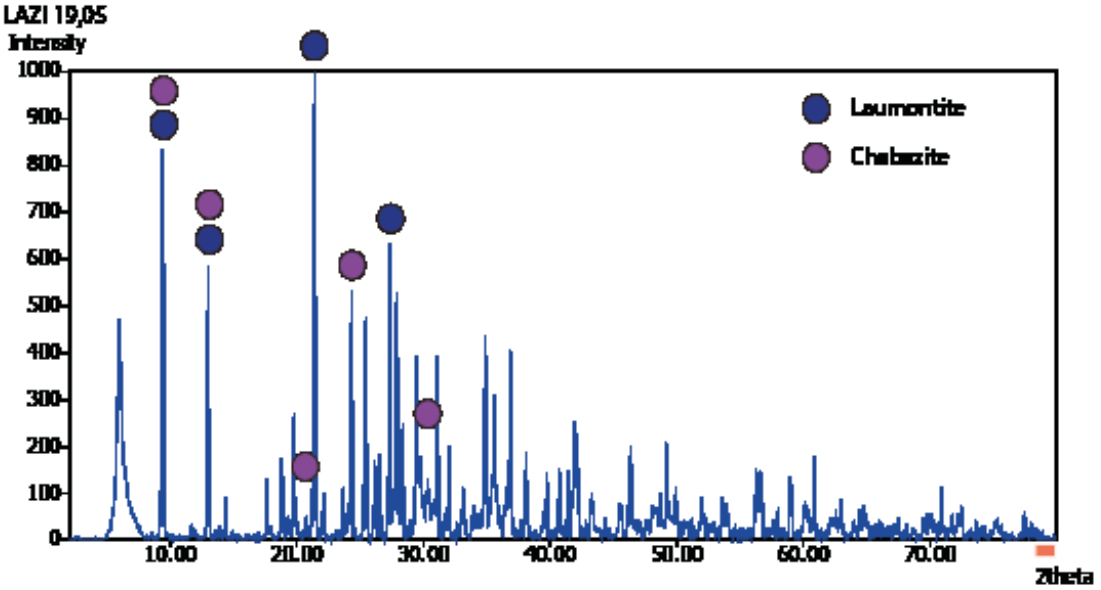
LAZI 19,05
Intensity
1000
900
800
700
600
500
400
300
200
100
0
10.00
20.00
30.00
40.00
50.00
60.00
70.00
2theta
Laumontite
Chabazite

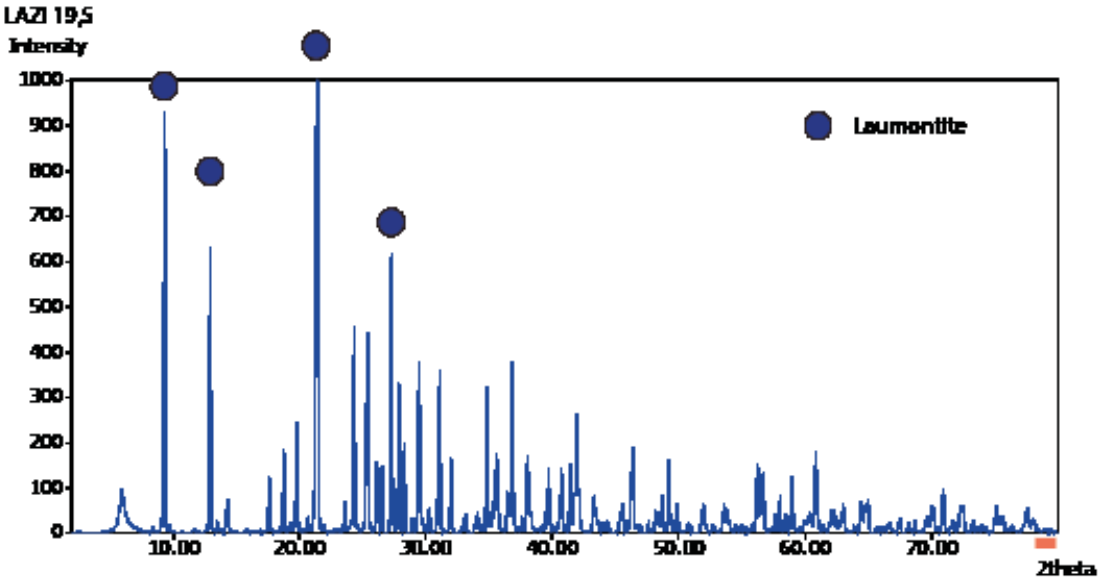
LAZI 19,5
Intensity
1000
900
800
700
600
500
400
300
200
100
0
10.00
20.00
30.00
40.00
50.00
60.00
70.00
2theta
Laumontite

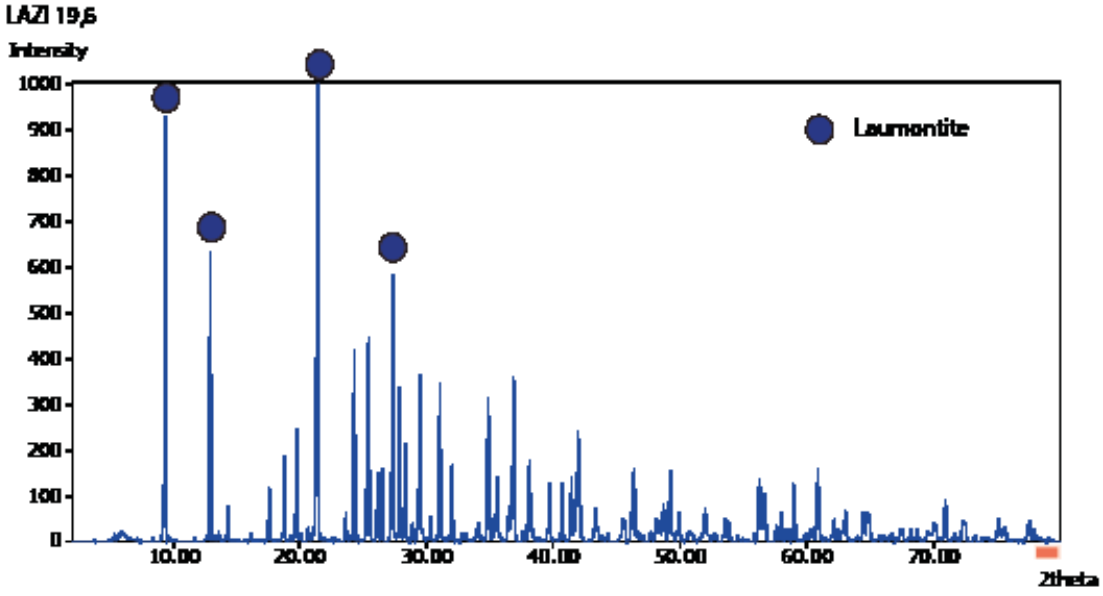
LAZI 19,6
Intensity
1000
900
800
700
600
500
400
300
200
100
0
10.00
20.00
30.00
40.00
50.00
60.00
70.00
2theta
Laumontite

APPENDIX H: FAILURE MODE DIAGRMAS IN THE PORE FLUID FACTOR-DIFFERENTIAL STRESS SPACE

In this work, failure criteria in pore fluid factor (λ)-differential stress (σ) space are built as indicated by Cox (2010), but expanding the analysis to the case where σ_2 does not lie in the fault plane, nor σ_v is approximated to any principal stress. This is the case of preexistent faults within a randomly oriented stress field.

H.1 Stress tensor algebra

The orientation of the stress tensor principal axes can be obtained from stress inversion methods, which are calculated from field observations from striations on fault surfaces (e.g. Yamaji, 2000). Then, the stress tensor is expressed in the vector basis built by the principal stress axes orientations (here after referred to as eigenvector basis):

$$\hat{\boldsymbol{\sigma}} = \begin{bmatrix} \sigma_1 & 0 & 0 \\ 0 & \sigma_2 & 0 \\ 0 & 0 & \sigma_3 \end{bmatrix}$$

Also, the stress inversion methods calculate the relative proportion between the magnitudes of principal stresses, value known as the stress tensor shape ratio:

$$\phi = \frac{\sigma_2 - \sigma_3}{\sigma_1 - \sigma_3} \tag{H.1}$$

However, the stress tensor should be expressed in convenient basis vectors, such as the basis built by NS-EW-vertical axes (here after referred to as geographic

basis). To transform the stress tensor from eigenvector basis to geographic basis, I use the tensorial transformation law:

$$\boldsymbol{\sigma} = \boldsymbol{R}\hat{\boldsymbol{\sigma}}\boldsymbol{R}^{\boldsymbol{T}}$$

where $\boldsymbol{\sigma}$ is the stress tensor expressed in the geographic basis, $\hat{\boldsymbol{\sigma}}$ is expressed in the eigenvector basis, and $\boldsymbol{R}$ is an orthonormal *rotation* matrix, whose columns represent the i-th eigenvector expressed in the geographic basis. Moreover, this rotation is defined by the direction cosines between both sets of basis vectors, which can be expressed in term of the azimuth (α) and plunge (β) of the stress principal axes:

$$\boldsymbol{R} = \begin{bmatrix} \sin(\alpha_1)\cos(\beta_1) & \sin(\alpha_2)\cos(\beta_2) & \sin(\alpha_3)\cos(\beta_3) \\ \cos(\alpha_1)\cos(\beta_1) & \cos(\alpha_2)\cos(\beta_2) & \cos(\alpha_3)\cos(\beta_3) \\ -\sin(\beta_1) & -\sin(\beta_2) & -\sin(\beta_3) \end{bmatrix}$$

In this way, for a given plane with normal vector $\boldsymbol{n}$ defined in the geographic basis, I now define stress components. First, the traction vector $\boldsymbol{t_n}$ is the projection of the stress tensor $\boldsymbol{\sigma}$ on the plane:

$$\boldsymbol{t_n} = \boldsymbol{\sigma n} \tag{H.2}$$

Following, the normal stress (σ_n) is the magnitude of the projection between $\boldsymbol{t_n}$ and the direction of interest ($\boldsymbol{n}$). Maximum shear stress (τ) in this plane is the magnitude of the difference between those vectors:

$$\sigma_n = \boldsymbol{n} \cdot \boldsymbol{t_n} = \boldsymbol{n} \cdot \boldsymbol{\sigma n} \tag{H.3}$$

$$\tau = |\boldsymbol{t_n} - \sigma_n \boldsymbol{n}| = \sqrt{|\boldsymbol{\sigma n}|^2 - {\sigma_n}^2} \tag{H.4}$$

We note that σ_n and τ are defined in terms of $\boldsymbol{n}$ and $\sigma_i, \alpha_i, \beta_i$ for $i = 1,2,3$. However, I recall that α_i, β_i and $\boldsymbol{n}$ are known from the structural data. Moreover, σ_2 can be removed of equations H.3 and H.4, by using equation H.1:

$$\sigma_2 = \phi(\sigma_1 - \sigma_3) + \sigma_3$$

Hence, $\boldsymbol{\sigma}$ components are functions that uses only σ_1 and σ_3 as arguments. Given that the stress tensor is expressed in the geographic basis, σ_v is the (3, 3) component of $\boldsymbol{\sigma}$, and equals:

$$\sigma_v(\sigma_1, \sigma_3) = \rho g z \tag{H.5}$$

where ρ is the rock density, g the gravity constant and z the depth of analysis.

We recall that the differential stress σ' is given by the equation:

$$\sigma' = \sigma_1 - \sigma_3 \tag{H.6}$$

Therefore, for a given σ' I calculate its corresponding σ_1 and σ_3 by combining equations H.5 and H.6. Finally, the values of σ_n and τ are calculated by replacing the values of σ_1 and σ_3 in equations H.2 and H.4.

H.2 Failure criteria in the $\boldsymbol{\lambda - \sigma}$ space

Three failure criteria are commonly used in rock mechanics for brittle failure, which depends on the mode of fracture. The first is extensional, which implies σ_n is lower than $-T$, the tensile strength of the rock. Moreover, for fracture development, the plane orientation is orthogonal to σ_3, thus $\sigma_n = \sigma_3 < -T$. The following two criteria are extension-shear and pure shear, which are well

constrained by the Griffith and the Mohr-Coulomb failure envelopes, respectively.

However, when σ_1 and σ_2 does not lie in the fault plane (or generally when less than any two principal stress directions), **shear stress will always be present**. This can be illustrated by the 3D Mohr's circle (Figure G-1).

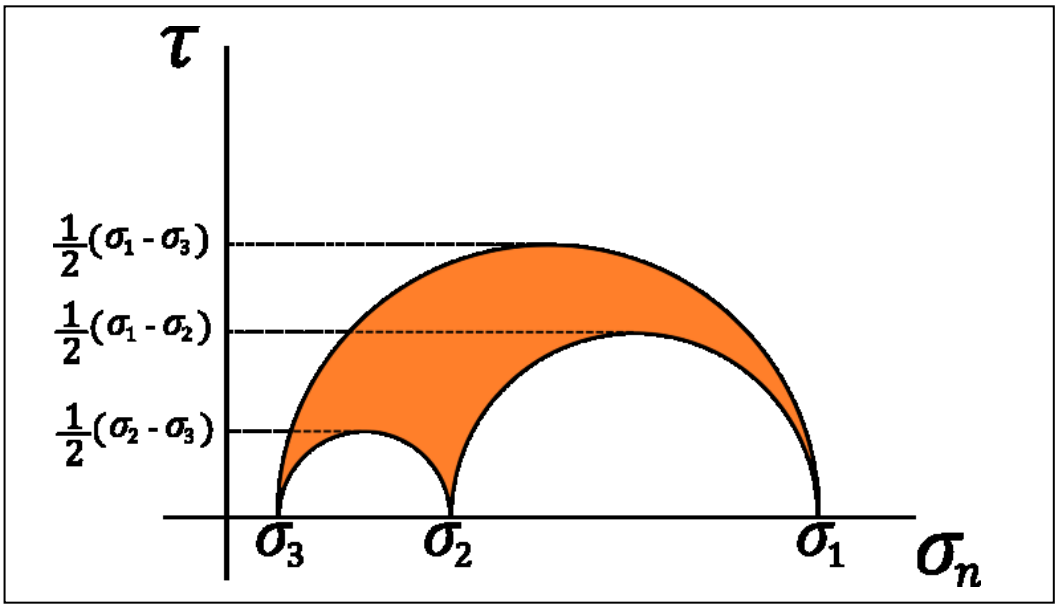

Figure G-1. 3D Mohr's circle, representing a random tri-axial state of stress. Each circle represents the state of stress within planes containing two principal stresses. The radiuses of the circles represent the maximum shear stress within such plane. However, the stress state of a plane oblique to all three principal stresses is located within the shaded area. Graphically, the only possibility to have zero shear stress is to be located within a plane, whose normal is parallel to any principal direction.

Therefore, extension criteria can be only applicable to the cases when the rock is subjected to an isotropic tensile state of stress, to fracture development and to faults in optimal orientation (parallel to both σ_1 and σ_2). For this reason, I use the Murrel's extension of Griffith criterion (generalized Griffith criterion) (Griffith,

1928; Murrell, 1963), a parabolic envelope which constrains the two cases of extension and extension-shear:

$$\tau^2 = 4T\sigma_n^{eff} + 4T^2 \tag{H.7}$$

Finally, shear faulting is described by the Mohr-Coulomb criterion:

$$\tau = \phi\sigma_n^{eff} + c \tag{H.8}$$

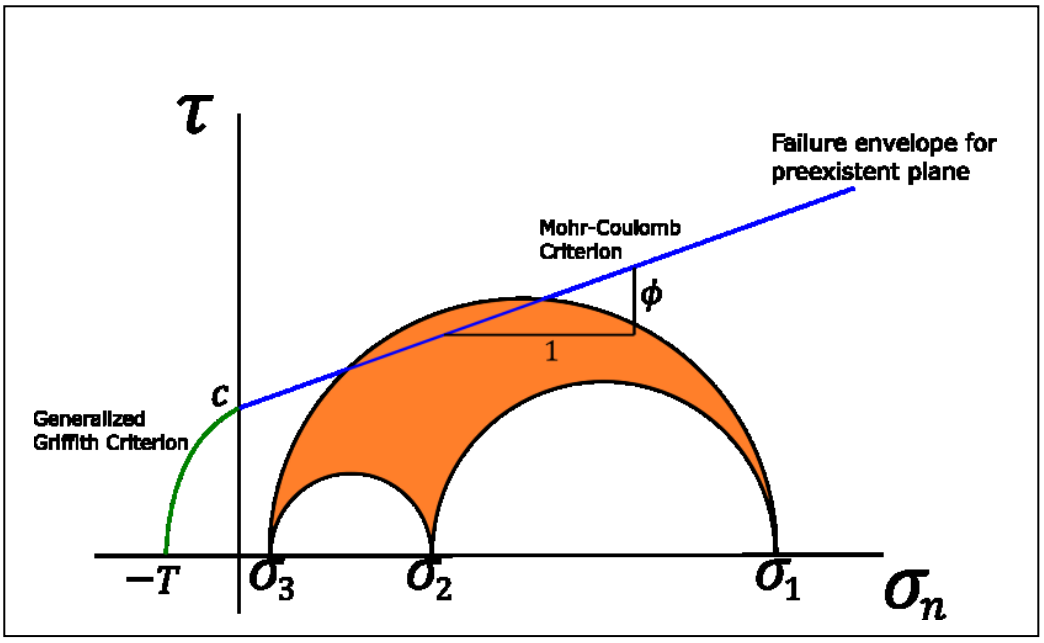

Figure G-2. Failure envelope for a preexistent plane within a random tri-axial state of stress. Extension-shear is described by the Generalized Griffith criterion (green), whereas pure shear by the Mohr-Coulomb criterion (blue). The greater circle does not necessarily contain the failure plane, but rather a preexistent plane in the shaded area if intersected by the failure envelope

To construct failure criterion in $\lambda - \sigma$ space, I substitute normal effective stress in terms of total stress and pore fluid pressure:

$$\sigma_n^{eff} = \sigma_n - P_f \tag{H.9}$$

Then, replacing equation H.9 into equations H.7 and H.8, and dividing by σ_v, I obtain:

$$\lambda = \frac{P_f}{\sigma_v} = \frac{\sigma_n + T}{\sigma_v} + \frac{\tau^2}{4T\sigma_v} \tag{H.10}$$

$$\lambda = \frac{P_f}{\sigma_v} = \frac{\sigma_n}{\sigma_v} + \frac{c - \tau}{\phi\sigma_v} \tag{H.11}$$

Given that $\sigma_n, \sigma_v, \sigma'$ and τ are defined in terms of σ_1 and σ_3, the differential stress could become an implicit argument of the Griffith criterion (Equation H.10) and Mohr-Coulomb (Equation H.11) in the $\lambda - \sigma$ space. These failure criteria are delimited when σ_n is positive (Mohr-Coloumb) or negative (Griffith criterion).